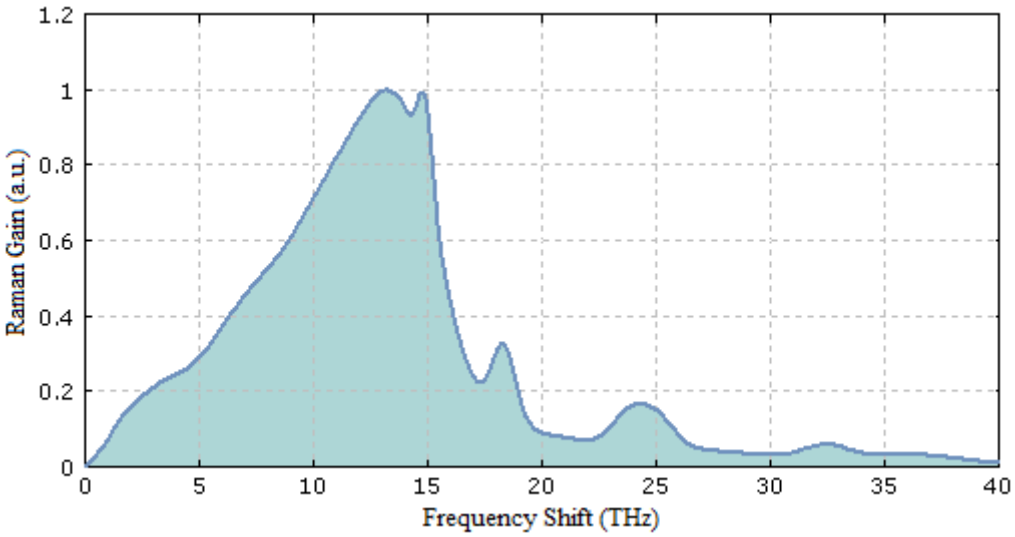

Distributed and Remote Fiber Sensing Assisted by Raman Effect

Hugo Fidalgo Martins
Física
Departamento de Física e Astronomia
2014

Supervisor
Orlando José dos Reis Frazão, Invited Assistant Professor of Departamento de Física e Astronomia da Faculdade de Ciências da Universidade do Porto and Senior Researcher at INESC Porto

Supervisor
Miguel González-Herráez, Associate Professor, Departamento de Electrónica de la Universidad de Alcalá

DEPARTAMENTO DE FÍSICA E ASTRONOMIA DA FACULDADE DE CIÊNCIAS DA UNIVERSIDADE DO PORTO

DEPARTAMENTO DE ELECTRÓNICA DE LA UNIVERSIDAD DE ALCALÁ

DOCTORAL THESIS

DISTRIBUTED AND REMOTE FIBER SENSING ASSISTED BY RAMAN EFFECT

This thesis was conducted under the supervision of

Prof. Dr. Orlando José dos Reis Frazão

Invited Assistant Professor of Departamento de Física e Astronomia da Faculdade de Ciências da Universidade do Porto and Senior Researcher at INESC TEC

and

Prof. Dr. Miguel González-Herráez

Associate Professor of Departamento de Electrónica de la Universidad de Alcalá

Hugo Fidalgo Martins

2014

Bolsa de investigação da Fundação para a Ciência e a Tecnologia com a referência SFRH/BD/76991/2011, financiada pelo POPH – QREN – Tipologia 4.1 – Formação Avançada, comparticipada pelo Fundo Social Europeu e por fundos nacionais do MCTES.

Acknowledgements

I would like to thank to everyone who contributed with work, time and patience to the realization of this thesis.

Firstly to my Portuguese supervisors Dr. Orlando Frazão and Professor Manuel Joaquim Marques, for accepting my PhD application and continuing to unconditionally support my work, after having already supervised my Master thesis. To Dr. Orlando Frazão, for his support and the help provided in all the stages of the experimental work developed in Portugal, from the numerous ideas to the scientific discussions, without forgetting his constant presence around the laboratory. Also for facilitating an initial contact with Professor Miguel González-Herráez, essential to arrange my research activity at the University of Alcalá. Special thanks to Professor Manuel Joaquim Marques, not only for the scientific discussions that were helpful to clarify the theoretical concepts necessary for a better understanding of optics in fibres and the help in writing the thesis, but also for assisting me with the process for the agreement of the jointly awarded PhD between the University of Porto and University of Alcalá and other bureaucratic procedures, which sometimes proved to be far more time and patience consuming than anticipated.

To my Spanish supervisor Professor Miguel González-Herráez for receiving me and providing the necessary arrangements for a most successful stay in the University of Alcalá. His expertise in distributed sensing provided an insightful understanding of numerous concepts and valuable help in the work developed in this area.

Especial thanks to Sonia Martin-Lopéz for introducing me to the laboratories and assisting me in the experimental work, especially at the beginning of my stay in Alcalá.

To Pedro Corredera and Juan Diego for their good mood and the material borrowed from the "*Consejo Superior de Investigaciones Cientificas*" (CSIC).

To Professor Luc Thévenaz for receiving me in École Polytechnique Fédérale de Lausanne (EPFL) to test the possibility to perform distributed birefringence measurements using ϕOTDR and to Dr. Marcelo Soto and Xin Lu for working with me

during my stay in EPFL. This collaboration was also possible due to the support provided by COST Action TD1001 (OFSeSa).

To Dr. Cristiano Cordeiro from Instituto de Física Gleb Wataghin, UNICAMP, for providing a three core PCF which was used as an intensity curvature sensor.

To Dr. Kay Schuster and Dr. Jens Kobelke from IPHT Jena for providing a double-core fibre which was used as an in-line MZ interferometer.

To my co-workers and friends from INESC TEC and Alcalá, for their companionship and good mood necessary to create a positive work environment.

To INESC TEC, the Physics and Astronomy Department of *Faculdade de Ciências da Universidade do Porto* and the *Universidad of Alcalá* for the opportunity and logistical support which allowed the realization of my PhD degree.

I also would like to acknowledge the PhD scholarship from FCT Fundação para a Ciência e a Tecnologia (Portuguese Foundation for Science and Technology), SFRH / BD / 76991 / 2011.

To my family, for their care, trust and comprehension through the years.

And last but not least, to my dearest wife Inês, for her patience and care, and for her help in the editing corrections of several publications, including this very thesis.

Abstract

In this thesis, the work developed in the Physics PhD Degree project is presented. The work was focused on distributed and remote optical fibre sensing assisted by Raman effect.

Throughout the thesis, an effort has been made to present solid but also academic analysis of the proposed configurations, which often included both experimental and theoretical results as well as qualitative and quantitative explanations of the physical principles of the measurement techniques.

A special emphasis has been given to the use of phase-sensitive optical time domain reflectometry (ϕOTDR) for distributed vibration sensing, which was extensively described both experimentally and theoretically using different configurations, including the use of first and second-order Raman amplification to extend the sensing range.

The use of ϕOTDR for static measurements was also studied: a technique based on the correlation of ϕOTDR measurements at two orthogonal states of polarization was proposed to measure local variations of the phase birefringence along any kind of optical fibre.

A new configuration for an intensity vibration sensor based on a Raman fibre laser is proposed for remote point sensing. In this case, the linear cavity of the Raman fibre laser relied on the combination of a distributed Rayleigh mirror and FBGs (Fibre Bragg Gratings), which were used as the sensing element and intensity filter.

As a result of parallel projects which were not directly connected to the main theme of the thesis, it was possible to test microstructured fibres for different applications. An intensity curvature sensor based on a three core Photonic Crystal fibre and a high-sensitivity strain and temperature sensor based on a dissimilar-doping dual-core fibre were proposed.

Resumo

Nesta tese, é apresentado o trabalho desenvolvido durante o projeto de Doutoramento em Física. O trabalho focou-se em sensores em fibra ótica distribuídos e remotos assistidos pelo efeito Raman.

Ao longo da tese, foi feito um esforço para apresentar uma análise robusta, mas também académica, das configurações propostas, que, muitas vezes, incluiu resultados experimentais e teóricos, bem como explicações qualitativas e quantitativas dos princípios físicos das técnicas de medição.

Foi dada especial importância ao uso de reflectometria ótica no domínio do tempo sensível à fase (ϕOTDR) para medição distribuída de vibrações, que foi extensivamente descrito a nível experimental e teórico, usando diferentes configurações, incluindo o uso de amplificação de Raman de primeira e segunda ordens para aumentar o alcance de deteção.

O uso de ϕOTDR para medições estáticas foi também estudado: uma técnica baseada na correlação de medições de ϕOTDR em dois estados de polarização ortogonais foi proposta para medir variações locais da birrefringência de fase ao longo de qualquer tipo de fibras óticas.

Uma nova configuração para um sensor de vibrações interrogado em intensidade baseada num laser de Raman em fibra foi proposta para um sensor pontual remoto. Neste caso, a cavidade linear do laser Raman em fibra baseava-se na combinação de um espelho Rayleigh distribuído e redes de Bragg em fibra, que foram usadas como elemento sensor e filtro de intensidade.

Como resultado de projetos paralelos, não diretamente relacionados com o tema principal desta tese, foi possível testar fibras microestruturadas para diferentes aplicações. Um sensor de curvatura interrogado em intensidade baseado numa fibra de cristal fotónico com três núcleos e um sensor de elevada sensibilidade de deformação e temperatura, baseado numa fibra com dois núcleos de dopagem distinta foram propostos.

Resumen

En esta memoria se presenta el trabajo realizado en el proyecto de doctorado en física. El trabajo se centra en el estudio de sensores de fibra óptica distribuidos y remotos asistidos por efecto Raman.

A lo largo de la tesis se hizo un esfuerzo para presentar, no solo un análisis sólido, sino también riguroso, de las configuraciones propuestas, que incluyen con frecuencia resultados experimentales y teóricos, así como explicaciones cualitativas y cuantitativas de los principios físicos de las técnicas de medición.

Se prestó especial atención a la utilización de la reflectometría óptica en el dominio del tiempo sensible a la fase (ϕOTDR) para medición distribuida de vibraciones, que se describe ampliamente desde la punto de vista tanto experimental como teórico, usando diferentes configuraciones e incluyendo el uso de la amplificación de Raman de primer y segundo orden para extender el rango de detección.

Se ha estudiado también el uso de ϕOTDR para mediciones estáticas: se propuso una técnica basada en las medidas de correlación ϕOTDR en dos estados ortogonales de polarización con el objeto de medir las variaciones locales de la birrefringencia de fase a lo largo de cualquier tipo de fibra óptica.

Se propuso una nueva configuración de sensor de vibración interrogado en intensidad basado en un láser Raman en fibra para un sensor puntual remoto. En este caso, la cavidad lineal del láser Raman en fibra se basa en una combinación de un espejo Rayleigh distribuido y redes de Bragg en fibra, que se utilizaron como elemento sensor y filtro de intensidad.

Como resultado de proyectos paralelos, que no están directamente relacionados con el tema principal de esta tesis, fue posible probar fibras microestruturadas para diferentes aplicaciones. Se han propuesto un sensor de curvatura interrogado en intensidad basado en una fibra de cristal fotónico con tres núcleos y un sensor de elevada sensibilidad a la deformación y la temperatura, basado en una fibra con dos núcleos con dopaje distinto.

Contents

List of Figures

List of Acronyms

ϕOTDR – Phase-sensitive optical time domain reflectometry

ASE – Amplified Spontaneous Emission

BOTDA – Brillouin Optical Time Domain Analysis

BOTDR – Brillouin optical time domain reflectometry

COTDR – Coherent OTDR

CW – Continuous wave

DBG – Dynamic Brillouin gratings

DC – Direct current

DCF – Dispersion Compensating fibre

DFB – Distributed-Feedback

DFOS – Distributed fibre optic sensors

DFWM – Degenerate Four-wave mixing

DPP – Differential Pulse-Width pair

DTS – Distributed temperature sensing

EDFA – Erbium-Doped fibre Amplifier

EOM – Electro-Optic Modulator

ER – Extinction Ratio

ESA – Electrical Spectrum Analyzer

FBG – fibre Bragg grating

FFT – Fast Fourier Transform

FPU – Fermi-Pasta-Ulam

FUT – fibre Under Test

FWHM – Full-Width at Half-Maximum

FWM – Four-wave Mixing

GDD – Group delay dispersion

GVD – Group Velocity Dispersion

IR – Infrared

IYL – International Year of Light

LD – Laser Diode

LO - Local oscillator

MI – Modulation Instability

MMF – Multimode fibres

MZ – Mach-Zehnder

MZI – Mach-Zehnder interferometer

NLSE – Nonlinear Schrödinger Equation

OFDR – Optical Frequency Domain Reflectometry

OSA – Optical Spectrum Analyzer

OTDR – Optical time domain reflectometry

PC – Polarization Controller

PCF – Photonic Crystal fibre

PDL – Polarization dependent loss

PMD – Polarization-mode dispersion

PMF – Polarization-maintaining fibre

POTDR – Polarization OTDR

PSw – Polarization Switch

PZT – Piezoelectric element

RFL – Raman fibre Laser

RIN – Relative Intensity Noise

RMS – Root mean square

SBS – Stimulated Brillouin scattering

SFG – Sum-Frequency Generation

SG – Signal Generator

SHG – Second-Harmonic Generation

SMF – Single-mode fibres

SMS – Single-Mode-Multimode-single-mode

SNR – Signal-to-noise ratio

SRS – Stimulated Raman scattering

SOA – Semiconductor Optical Amplifier

SOP – State of polarization

SPM – Self-phase Modulation

TOD – Third-order dispersion

TOF – Tuneable Optical Filter

URFL – Ultralong Raman fibre laser

UV – Ultraviolet

WDMs – Wavelength division multiplexers

XPM – Cross-phase modulation

1 Introduction

1.1 Contextualization of the work

In the 21st century, light based technology plays a vital role in our daily lives, having revolutionized areas as important as medicine, internet communications, among several others. The importance of such systems is well established and recognized by prestigious international entities: in 2009 Charles Kao won the Nobel Prize in Physics for "*groundbreaking achievements concerning the transmission of light in fibres for optical communication*"; in the end of 2013, the United Nations (UN) proclaimed 2015 as the International Year of Light and Light-based Technologies (IYL 2015).

In the context of optical fibres, a number of linear and nonlinear effects can be generated which can set limitations or be used in an advantageous manner, depending on the specific situation. Rayleigh scattering is the main effect responsible for fibre losses in the 1.55 μm region. Brillouin scattering can limit the transmitted power, especially with narrowband optical signals. Modulation instability (MI) and Raman scattering can generate and amplify noise at frequencies near that of the main signal. However, using the same effects, Rayleigh backscatter, Brillouin and Raman effects can also be used for distributed sensing and MI has been used to generate stable ultra-short pulses. Raman amplification has also been widely studied and reported in the scientific literature as a way to increase the sensing range and signal-to-noise ratio (SNR) of optical communications and sensing systems. Understanding these optical effects is therefore of fundamental importance, whether to limit their impact on existing optical systems or to develop new ones.

Among light based systems, the specific interest in fibre optic sensors has increased significantly over the last decade due to their intrinsic properties, such as immunity to electromagnetic noise, small size, geometric versatility, lightweight, relatively low cost, possibility of remote operation and multiplexing capability. In most systems, the fibre can be used as both the sensing element and the communication channel, which allows numerous convenient solutions using this type of technology. When the number of points to be monitored is very large, distributed sensors present clear advantages over conventional point sensors, due to their low cost per monitored point, and should therefore be preferred for monitoring large important infrastructures such as bridges, dams, railways, pipelines for gas and oil transport, high power electrical lines or national borders.

Several types of distributed fibre optic sensors have been demonstrated for monitoring different parameters at any point along a fibre. Optical time domain reflectometry (OTDR) is a Rayleigh backscatter based technique commonly used for distributed measurement of losses along the fibre (including the measurement of fibre attenuation, the location of broken points and optical connectors, discontinuities and others). Brillouin based sensing is traditionally used in strain and temperature sensing. The use of phase-sensitive OTDR (ϕOTDR) has been demonstrated for the distributed measurement of vibrations which can be used to monitor intrusions and, more recently, for highly sensitive distributed temperature measurements. Depending on the required spatial resolution, the distributed optical fibre sensors mentioned can typically present measuring ranges of up to a few tens of kilometers which, depending on the application, may not be enough.

In this context, the aim of this PhD program is to study the possibility of using the Raman effect to improve the performance, mainly the sensing range and SNR, of distributed and remote optical fibre sensors. Special care is taken with the detrimental phenomena associated with the technique, mainly the amplified spontaneous emission (ASE) noise introduced and the Relative Intensity Noise (RIN) transfer which can severely degrade the system performance.

1.2 Motivation and Objectives

The main motivations for the work reported in this PhD thesis were the study of the possibility of using the Raman effect to improve the performance of distributed and remote optical fibre sensors, mainly focused on vibration sensing.

Acquisition of further knowledge and better understanding of the different effects which occur in optical fibres, and of the fundamental physical mechanisms which lead to them, were also an ever present motivation for the work developed in this thesis.

The following objectives have been addressed in this PhD programme:

- Perform a detailed study of ϕOTDR operation when used for distributed vibration sensing, including proper identification of the main linear and nonlinear effects which limit its performance, in order to avoid/minimize them in future systems.
- Document the use of first- and second-order Raman amplification schemes to increase the performance of ϕOTDR distributed vibration sensing using the best configurations identified in the previous point. Characterize its performance as well as the limiting effects of the system, with especial attention to the RIN transfer and ASE noise introduced by the Raman pumps.
- Investigate the possibility of using a Raman fibre laser (RFL) combined with fibre Bragg gratings (FBGs) for remote point sensing of vibrations with high SNR and optical intensity variation interrogation.
- Work with microstructured fibres, evaluating the possibility to use them for optical sensing.

1.3 Organization of the Dissertation

This thesis is divided into seven chapters in which several concepts related to the work developed are described.

In chapter 1, besides the contextualization of the work and the description of motivation and objectives, a list of the main contributions and publications is presented.

In chapter 2, the physical explanation of the optical properties of the fibres used in this thesis is presented. Losses, dispersion and birefringence are discussed as linear effects. As for the nonlinear effects, parametric nonlinearities and nonlinear refractive index, which lead to the occurrence of MI in fibres, are discussed. Lastly, an overview of Rayleigh and Raman scattering processes is presented.

In chapter 3, an extensive investigation on the use of ϕOTDR for distributed vibration sensing, which includes experimental and theoretical descriptions using different configurations, is presented. The limitations due to MI are discussed and the performance of the different configurations, including the use of first and second-order Raman amplification, is analyzed.

In chapter 4, a method to measure local variations of the phase birefringence along any kind of optical fibre is proposed. The technique is based on the correlation of ϕOTDR measurements of two orthogonal states of polarization.

In chapter 5, a new configuration for a remote intensity vibration sensor based on a Raman fibre laser is proposed. The linear cavity of the Raman fibre laser relies on the combination of a distributed Rayleigh mirror and FBGs, which are used as the sensing element and intensity filter.

In chapter 6, two additional works, which resulted from parallel projects which were not directly connected to the main theme of the thesis, are presented. Firstly, a curvature sensor which uses a simple interrogation technique based on optical power variation using a Photonic Crystal fibre (PCF) is proposed. Then, a dual-core fibre, in which one of the cores is doped with Germanium and the other with Phosphorus, is used as an in-line Mach-Zehnder (MZ) dispersive interferometer, is characterized for strain and temperature measurement.

In chapter 7, the final conclusions of the thesis and some suggestions for future work are presented.

1.4 Main Contributions

The most important contributions which resulted from the work developed during this PhD programme are listed below:

- Theoretical and experimental in-depth descriptions of the impact of MI in the performance of a ϕOTDR are presented, to the best of our knowledge, for the first time. It has been demonstrated that MI generally leads to localized fading of the interference recorded in the trace and therefore to loss of sensitivity in these positions. This work can be useful for understanding the limitations imposed by MI in ϕOTDR operation in both dynamic and static measurements.
- An experimental and theoretical description of the use of first and second-order Raman amplification to improve the performance of ϕOTDR is presented. The detection of vibrations of up to 250 Hz and 380 Hz, respectively, over 125 km with a resolution of 10 m and no post-processing was achieved.
- A technique that uses the cross-correlation between ϕOTDR measurements of orthogonal states of polarization has been proposed and experimentally validated for distributed birefringence measurement. The method offers the possibility to discriminate local birefringence variations along many tens of km of optical fibres with metric spatial resolution. The high birefringence accuracy demonstrated ($\sim 10^{-7}$) enables proper distributed characterization of low birefringence single-mode fibres.
- A new device concept for a highly sensitive MZ interferometer, based on a dual-core fibre with dissimilar-doping, has been described theoretically and experimentally. Opposite sensitivities for wavelength peaks above and below the central wavelength of the interferometer were demonstrated when strain and temperature were applied. To our knowledge this is the first time that such behaviour was demonstrated using this type of in-line interferometer based on a dual-core fibre. A sensitivity of (0.102±0.002) nm/$\mu\varepsilon$, between 0-800 $\mu\varepsilon$, and (-4.0±0.2) nm/ºC between 47-62ºC, was demonstrated.

1.5 List of Publications

During the PhD thesis project the author published six papers in international scientific journals, all as first author.

The results obtained during the PhD thesis were also presented at seven international conferences and two national conferences. The references of the published articles and conference proceedings are listed below.

1.5.1 Articles published in International Scientific Journals (6)

[1] Martins, H.F., et al., *Intensity Curvature Sensor based on Photonic Crystal fibre with Three Coupled Cores*, Optics Communications, 2012 **285**(24): pp.5128-5131.

[2] Martins, H.F., et al., *Modulation instability-induced fading in phase-sensitive optical time-domain reflectometry.* Optics Letters, 2013. **38**(6): p. 872-874.

[3] Martins, H.F., et al., *Coherent Noise Reduction in High Visibility Phase-Sensitive Optical Time Domain Reflectometer for Distributed Sensing of Ultrasonic Waves.* Journal of Lightwave Technology, 2013. **31**(23): p. 3631-3637.

[4] Martins, H.F., M.B. Marques, and O. Frazão, *Intensity vibration sensor based on Raman fibre laser using a distributed mirror combined with Bragg grating structures.* Applied Physics B, 2014. **114**(4): p. 455-459.

[5] Martins, H.F., et al., *Phase-sensitive optical time domain reflectometer assisted by first-order Raman amplification for distributed vibration sensing over >100km.* Journal of Lightwave Technology, 2014. **32**(8): p. 1510-1518.

[6] Martins, H.F., et al, *High-sensitivity dispersive Mach-Zehnder interferometer based on a dissimilar-doping dual-core fibre for sensing applications,* Optics Letters, 2014 **39**(9): pp.2763-2766.

1.5.2 Conference Proceedings (11)

1. -H. F. Martins, M. J. Marques, P. Jorge, C. M. B. Cordeiro, O. Frazão, "Intensity Curvature Sensor based on Photonic Crystal fibre with Three Coupled" Cores, SPIE Photonics Europe 201 - SPIE Photonics Europe 2012 | Photonics, Optics, Lasers, Micro- Nanotechnologies Research, vol.8026, Brussels, Belgium, 2012.

2. -H. Martins, M. B. Marques and O. Frazão, "100 km-Ultralong Raman fibre Laser using a Distributed Rayleigh Mirror for Sensing Applications" SEON 2012 - X Symposium on Enabling Optical Networks and Sensors, Porto, Portugal, 2012.
3. -H. F. Martins, M. J. Marques, O. Frazão, "Sensor de vibração usando laser de Raman com espalhamento de Rayleigh cooperativo," Física 2012 - Física 2012, Aveiro, Portugal, 2012.
4. -H. F. Martins, S. M. Lopez, P. Corredera, M. L. Filograno, O. Frazão and M. G. Herráez, "Modulation instability-induced visibility fading in phase-sensitive OTDR," EWOFS 2013 - 5th European Workshop on Optical fibre Sensors, Kraków, Poland, May, 2013.
5. -H. F. Martins, S. M. Lopez, P. Corredera, M. L. Filograno, O. Frazão and M. G. Herráez, "High visibility phase-sensitive optical time domain reflectometer for distributed sensing of ultrasonic waves," EWOFS 2013 - 5th European Workshop on Optical fibre Sensors, Kraków, Poland, May, 2013.
6. -H. F. Martins, S. M. Lopez, P. Corredera, M. L. Filograno, O. Frazão and M. G. Herráez, "Characterization of a phase-sensitive optical time domain reflectometer used for distributed sensing of vibrations and its performance limits due to modulation instability," OPTOEL 2013, Alcalá de Henares, Spain, 2013
7. -H. F. Martins, M. J. Marques, O. Frazão, "Raman fibre laser using a distributed mirror combined with Bragg grating structures for intensity vibration sensing," RIAO/OPTILAS 2013 - VIII Iberoamerican Conference on Optics and XI Latinamerican meeting on Optics Lasers and Applications, Oporto, Portugal, July, 2013.
8. -H. F. Martins, J. Bierlich, K.Wondraczek, S. Unger, J. Kobelke, K. Schuster, M. B. Marquesa, M. Gonzalez-Herraez, O. Frazão, “Dual core fibre interferometer as in-line Mach-Zenhder interferometer sensor”, AOP14 Second International Conference on Applications of Optics and Photonics, Aveiro, Portugal, 2014
9. -H. F. Martins, J. Bierlich, K.Wondraczek, S. Unger, J. Kobelke, K. Schuster, M. B. Marquesa, M. Gonzalez-Herraez, O. Frazão, “In-line Mach-Zehnder interferometer based on a dissimilar-doping dual-core fibre for high sensitivity strain and temperature sensing”, OFS-23 2014, Santander, Spain, 2014
10. -H. F. Martins, S. Martin-Lopez, M. L. Filograno, P. Corredera, O. Frazão, and M. Gonzalez-Herraez, “Comparison of the use of first and second-order Raman

amplification to assist a phase-sensitive optical time domain reflectometer in distributed vibration sensing over 125 km", OFS-23 2014, Santander, Spain, 2014

11. -H. F. Martins, X. Lu, M. A. Soto, M. Gonzalez-Herraez, L. Thévenaz. "Distributed Birefringence Measurements Using Polarisation Correlation in Phase-Sensitive OTDR", ECOC 2014, Cannes, France, 2014 (paper accepted).

2 Optical effects in fibres

2.1 Introduction

A number of processes can affect the characteristics of any optical wave travelling in a medium, and optical fibres are no different. Since it is important for the reader to be aware of this situation, a thorough theoretical description of the most relevant effects which occur in optical fibres, within the context of the work reported in this dissertation, will be presented in this chapter.

Firstly, the propagation of light in the linear regime will be described, presenting an overview of the losses (with special emphasis on Rayleigh scattering), chromatic dispersion and polarization-mode dispersion (PMD). Then, the nonlinear effects are discussed: it is explained how parametric processes (mainly self-phase and cross-phase modulation (XPM)) lead to a nonlinear dependence of the refractive index on the optical power, which in turn leads to modulation instability (MI). An explanation of the physical principles behind Rayleigh and Raman scattering is also presented.

2.2 Linear effects

When an electromagnetic wave with electric field $E(\omega)$ of angular frequency ω propagates in a dielectric medium, it induces a linear polarization $\boldsymbol{P_L}(\omega)$ (assuming a linear response of the medium) which is usually frequency dependent. This polarization depends on how the bound electrons of the medium respond to the applied $E(\omega)$ and is therefore strongly dependent on the resonance frequencies of the medium. From these two quantities, the linear optical susceptibility $\chi^{(1)}(\omega)$ can be defined as

$$\chi^{(1)}(\omega) = \frac{P_L(\omega)}{\varepsilon_0 E(\omega)}, \tag{2.1}$$

where ε_0 is the electric permittivity of free space. $\chi^{(1)}(\omega)$ is a very important parameter from which several important properties of the fibre can be derived. The complex refractive index $n_c(\omega)$ is derived from $\chi^{(1)}(\omega)$:

$$n_c(\omega) = \sqrt{1+\chi^{(1)}(\omega)}\,. \tag{2.2}$$

From the complex refractive index $n_c(\omega)$, the real refractive index $n(\omega)$ and attenuation constant $\alpha(\omega)$ can be defined as [7]

$$n(\omega) = \mathrm{Re}(n_c(\omega)) \tag{2.3}$$

$$\alpha(\omega) = \frac{2\omega}{c}\mathrm{Im}(n_c(\omega)), \tag{2.4}$$

where c is the light velocity in the vacuum. Polarization-mode dispersion (PMD) and polarization dependent loss (PDL) can also be described as a dependency of $n_c(\omega)$ on the polarization axis of the propagating wave.

2.2.1 Optical Losses: absorption and scattering

The electric field for a plane wave propagating along the z axis in a material, $E(z,t)$, is given by

$$E(z,t) = E_0 e^{i\omega(\frac{n_c(\omega)}{c}z - t)} + E_0 e^{-i\omega(\frac{n_c(\omega)}{c}z - t)}. \tag{2.5}$$

Due to the imaginary part of $n_c(\omega)$ (see eq. 2.4), an optical signal propagating in a fibre will experience losses proportional to the propagating power. Therefore, the optical power $P(L)$ of the signal after a distance of propagation L in the fibre will be given by

$$P(L) = P_i e^{(-\alpha L)}, \tag{2.6}$$

where P_i is the input power and α (usually given in km^{-1}) is the attenuation constant which accounts for all losses in the medium. Usually the attenuation constant is given in dB/km (α_{dB}):

$$\alpha_{dB} = -\frac{10}{L}\log_{10}(\frac{P(L)}{P_i}) = 10\alpha\log_{10}(e) = 4.343\alpha. \tag{2.7}$$

In an optical fibre, optical absorption and optical scattering are the main causes of losses. The losses can be divided into intrinsic losses of the material (optical absorption peaks which occur at the resonance frequencies of the material and optical scattering) and extrinsic losses (optical absorption peaks caused by impurities and mechanical stress or curvatures applied to the fibre that induce local losses).

Regarding optical absorption losses, in the case of silica fibres, absorption peaks occur in the ultraviolet (UV) (<200 nm) and infrared (IR) (~7000 nm), due to the resonances of *Si-O* and electrons in atoms - intrinsic losses. These absorption peaks have tails that extend into the visible and near IR wavelengths.

Additional resonance peaks, and therefore additional absorption peaks will be added in the presence of impurities - extrinsic losses. In the case of silica fibres, the presence of OH^- ions will cause absorption at the OH^- fundamental vibrational absorption peak at 2.73 μm, and its overtones near 1.37 μm, 1.23 μm and 0.95 μm [8].

Another type of optical absorption losses occurs due to atomic irregularities (color centres). These are mostly negligible due to the optimized modern fibre fabrication processes. However, when high intensities are employed, absorption in these irregularities can lead to local changes of the structure of the fibre, which in turn will lead to higher absorption. This exponential process can lead to the destruction of the fibre.

In the case of the losses in fibres due to optical scattering (intrinsic losses), these can be caused by Rayleigh scattering (scattering by inhomogeneities much smaller than the wavelength), Mie scattering (scattering by inhomogeneities with size above the light wavelength) and scattering generated by imperfections in the core-cladding interface (waveguide scattering). However, due to the quality of the modern fabrication processes of optical fibres, in which the typical size of density fluctuations are much smaller (<10 %) than the propagating wavelengths, losses due to optical scattering in fibres are mainly caused by Rayleigh scattering (described in further detail in section 2.4.1) The Rayleigh scattering induced loss coefficient (α_R) can be expressed as:

$$\alpha_R = \frac{C_R}{\lambda^4}. \tag{2.8}$$

Usually α_R is given in dB/km. The constant C_R is dependent on the components and fabrication method of the fibre, but is typically within the range 0.7-0.9 dB km^{-1} μm^4 [9]. Since the Rayleigh scattering induced losses vary with λ^{-4}, they are dominant for short wavelengths.

In Fig. 2.1, the typical loss spectrum (represented by the attenuation constant α_{dB}) of an optical silica fibre is presented. The Rayleigh scattering losses decrease as the wavelength increases and a local minimum loss of ≈0.2 dB/km is observed at around 1550 nm, between the peak losses induced by the OH^- ions and the IR absorption. This minimum corresponds to the third transmission window and will be used in this

dissertation. Two other local minima are located at 800 nm and 1310 nm, and correspond to the first and second communication windows.

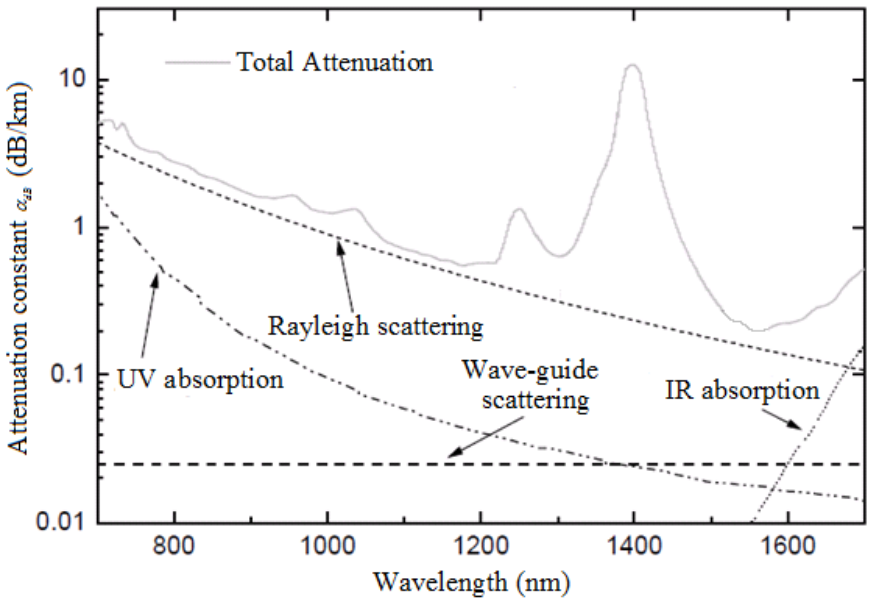

Fig. 2.1 Typical loss spectrum for a silica fibre (Adapted from ref. [10]).

2.2.2 Chromatic Dispersion

The linear optical refractive index $n(\omega)$ defines the phase velocities $\boldsymbol{v_p}(\omega)$ at which different frequencies ω will travel in the fibre:

$$\boldsymbol{v}_p(\omega) = \frac{c}{n(\omega)}. \tag{2.9}$$

Eq. 2.9 therefore defines the chromatic dispersion of the fibre, which is the dependency of $\boldsymbol{v_p}(\omega)$ (and hence $n(\omega)$) on the frequency of the propagating wave, ω.

When working with optical pulses, it is useful to define the dispersion as a Taylor expansion of the mode-propagation constant $\beta(\omega)$ around the central angular frequency of the pulse, ω_0:

$$\beta(\omega) = n(\omega)\frac{\omega}{c} = \beta_0 + \beta_1(\omega-\omega_0) + \frac{1}{2}\beta_2(\omega-\omega_0)^2 + \frac{1}{6}\beta_3(\omega-\omega_0)^3 + \ldots . \tag{2.10}$$

Here β_0 is the mode-propagation constant at ω_0, and β_i is the i^{th}-order dispersion coefficient, given by:

$$\beta_i = \left(\frac{\partial^i \beta(\omega)}{\partial \omega^i} \right)_{\omega=\omega_0} \qquad (i = 0,1,2,3...)\,. \tag{2.11}$$

The first-order dispersion coefficient β_1 is the inverse of the group velocity $\boldsymbol{v_g}$,

$$\beta_1 = \frac{1}{\mathrm{v}_g(\omega)} = \frac{n_g(\omega)}{c} = \frac{1}{c}\left(n(\omega) + \omega \frac{n(\omega)}{\partial \omega} \right), \tag{2.12}$$

where $n_g(\omega)$ is the group refractive index. The second-order dispersion coefficient β_2 is also referred as group velocity dispersion (GVD), and β_3 is the third-order dispersion (TOD) coefficient. Physically, the group velocity is the velocity at which the envelope of an optical pulse moves and the GVD describes the dispersion (i.e., dependency on ω) of the group velocity. GVD is responsible for the broadening of optical pulses, since different frequencies will travel at different velocities, and is therefore an undesired effect in optical communication. When the GVD>0 (<0), the dispersion is said to be normal (anomalous). In silica fibres, the GVD increases with the wavelength, crossing the zero at ~1.3 μm, although dispersion-shifted fibres, where the zero has been shifted to ~1.5 μm, have been developed a long time ago [11].

When working with optical fibres, the chromatic dispersion parameter D is commonly used instead of GVD, being defined as

$$D = \frac{\partial \beta_1}{\partial \lambda} = -\frac{2\pi c}{\lambda^2} \beta_2\,, \tag{2.13}$$

where λ is the wavelength corresponding to the mode of frequency ω. D is usually given in ps km^{-1} nm^{-1}, and can be understood as the time delay (ps) between two waves of wavelengths separated by 1 nm after travelling 1 km of fibre.

In optical fibres, chromatic dispersion can generally result from a dependency of n in ω associated with the resonances of the material (material dispersion) but also from geometrical effects (waveguide dispersion). Waveguide dispersion is associated with the change of the modal radius with frequency. Since there is a difference between the $n(\omega)$ of the core and cladding, this leads to an effective $n(\omega)$ variation with frequency.

Different modes of propagation also experience different value of $n(\omega)$, but in SMFs, since there is only one mode of propagation, intermodal dispersion does not occur. Another kind of dispersion is PMD, which is discussed in the next section.

2.2.3 Polarization-mode dispersion

The linear polarization $\boldsymbol{P_L(\omega)}$ induced in a dielectric medium by an applied electric field $E(\omega)$ is owed to a rearrangement of the charges in the medium. Therefore $\boldsymbol{P_L(\omega)}$ is strongly dependent on the molecular structure of the medium and can depend on the direction of the applied $E(\omega)$ in an anisotropic material. In this case, $\chi^{(1)}(\omega)$ and $n(\omega)$ depend on the state of polarization (SOP) of $E(\omega)$ and the medium is said to be birefringent. In a birefringent medium, two modes with the same frequency and different polarizations have different β – modal birefringence. The optical absorption function can also be dependent on the polarization – PDL. Although this effect is less important in fibre optics, it can be relevant for optical components. The strength of modal birefringence β_m is defined as [12]:

$$\beta_m = \frac{\lambda}{2\pi} |\beta_x - \beta_y| = |n_x - n_y| \tag{2.14}$$

where n_x, n_y are the refractive indices for the two orthogonally polarized states. From β_m, the beat length L_B, defined as the period over which the two modes exchange their powers when propagating along the fibre, can be derived:

$$L_B = \frac{2\pi}{|\beta_x - \beta_y|} = \frac{\lambda}{\beta_m} \tag{2.15}$$

Since different polarizations experience different refractive indices, these will travel at different velocities, which will cause a broadening of a pulse propagating in the fibre if both polarization components are excited – PMD.

In an amorphous system with geometrical symmetry such as a single-mode fibre (SMF), birefringence should not occur since it requires a break of symmetry. However, due to random fluctuations of $n(\omega)$ or mechanical stresses, optical fibres always present some birefringence. Although this does not considerably affect the value of $n(\omega)$ and can therefore be neglected for most purposes when using unpolarized light, these small fluctuations cause the SOP of propagating waves to change randomly, thus causing instability in the output of the state of polarization.

In order to solve this problem, polarization-maintaining fibres (PMFs) have been developed. These present a high built-in birefringence which prevents the coupling of light from one polarization mode to the other. In this case, if the polarization of the light

coupled is aligned with one of the polarization axis, the SOP will be preserved even if the fibre is bent or small fluctuations in $n(\omega)$ occur. However, if both polarization axis are excited, the SOP will change continuously, repeating itself after a period of L_B.

PMFs are built by introducing asymmetries in the fabrication process. These asymmetries can be geometrical (such as a non-circular core or asymmetric microstructured fibre), due to a built-in mechanical stress (as in Panda or Bow-tie fibres) or an asymmetric refractive index profile. Fig. 2.2 shows some of the most common types of PMFs.

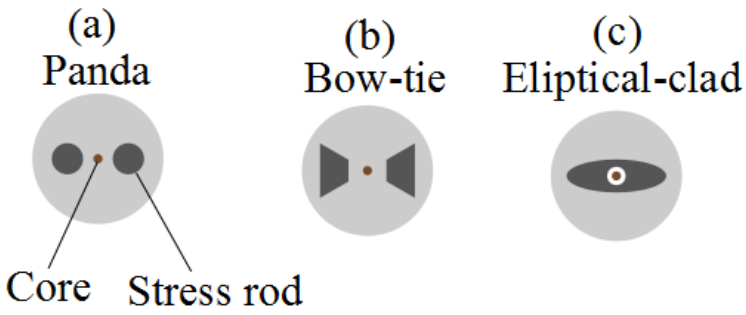

Fig. 2.2 Different types of PMF: a) Panda, b) Bow-tie, c) Elliptical-clad (Adapted from ref. [13]).

PMFs can also be used for sensing applications. The birefringence in a PMF can be dependent on the applied pressure, thus making these fibres suitable for the measurements of pressure [14]. In this dissertation, distributed measurement of birefringence is achieved along PMF and SMF using phase-sensitive OTDR (ϕOTDR) (chapter 4).

2.3 Nonlinear Propagation

A number of nonlinear processes become relevant when the interaction length, or the optical intensity, is high. Depending on the working conditions, some processes can be neglected or are simply forbidden, while others take special relevance. In this section, the most important parametric nonlinearities for the work developed in this thesis are described. A process is called parametric if the initial and final states of the atoms in the medium where the electromagnetic waves interact are the same. Therefore, the energy and momentum of the interacting waves must be conserved and the medium plays a passive role. In this category are included Self-Phase Modulation (SPM) and Cross-Phase Modulation (XPM), which are a consequence of the Kerr effect (nonlinear dependence of the refractive index on the optical power) and without which MI would not occur.

2.3.1 Parametric nonlinearities

The polarization induced by the electromagnetic radiation in a dielectric medium becomes nonlinear for high intensities. This response is generated by the anharmonic oscillation of the bound electrons of the medium to the applied field. In this case, the polarization response $\vec{P}(\omega)$ is given by a power series in the electric field $\vec{E}(\omega)$ strength and eq. 2.1 can be modified to

$$\begin{aligned}\vec{P}(\omega) &= \varepsilon_0[\chi^{(1)}(\omega)\cdot\vec{E}(\omega)+\chi^{(2)}(\omega):\vec{E}(\omega)\vec{E}(\omega)+\chi^{(3)}(\omega)\vdots\vec{E}(\omega)\vec{E}(\omega)\vec{E}(\omega)+...] \\ &= \vec{P}_L(\omega)+\vec{P}_{2NL}(\omega)+\vec{P}_{3NL}(\omega)+... ,\end{aligned} \tag{2.16}$$

where $\vec{P}_L(\omega)$ is the linear polarization, $\chi^{(i)}$(i=2,3...) is the i^{th} order nonlinear optical susceptibility and $\vec{P}_{iNL}(\omega)$ is the i^{th} order nonlinear polarization. Typically, for condensed matter, $\chi^{(1)}$ is of the order of the unit, $\chi^{(2)}\approx10^{-12}$ m/V and $\chi^{(3)}\approx10^{-24}$ m^2/V^2 [7].

The quantity $\chi^{(2)}$ is responsible for Second-Harmonic Generation (SHG), Sum-Frequency Generation (SFG) and Three-Wave Mixing. However, the existence of a $\chi^{(n)}$ with an even order *n* implies that the medium does not have inversion symmetry. Therefore, for amorphous media (such as amorphous silica), these terms are only non-null at the interfaces and hence negligible for most purposes.

The quantity $\chi^{(3)}$ is responsible for the third order nonlinear polarization $\vec{P}_{3NL}(\omega)$. The molecular contributions to $\chi^{(3)}$ (Raman effect) can be neglected assuming instantaneous response. Considering a monochromatic wave $\vec{E}(\omega)$, then $\vec{P}_{3NL}(\omega)$ will have a term oscillating at frequency ω and another at 3ω (Third-Harmonic Generation - THG). However, the THG term requires phase-matching and is usually negligible in optical fibres. In this case $\vec{P}_{3NL}(\omega)$ will be given by:

$$\vec{P}_{3NL}(\omega) \approx \frac{\varepsilon_0 \chi_{xxxx}^{(3)} 3 |E(\omega)|^2}{4} E(\omega). \tag{2.17}$$

$\vec{P}_{3NL}(\omega)$ is responsible for the Kerr effect, as seen in the next section.

2.3.2 Nonlinear refractive index

The refractive index *n* can be calculated from the total polarization (P_L+P_{3NL}, defined in eq. 2.17), similarly to eq. 2.2. In this case, it is shown that *n* becomes dependent in the optical intensity travelling in the medium (Kerr effect):

$$n = \sqrt{1 + \frac{P_L(\omega) + P_{3NL}(\omega)}{\varepsilon_0 E(\omega)}} = \sqrt{1 + \chi^{(1)} + \frac{\chi_{xxxx}^{(3)} 3 |E(\omega)|^2}{4}} \simeq n_0 + n_2 |E|^2 \tag{2.18}$$

where $n_0 = \mathrm{Re}(\sqrt{1+\chi^{(1)}})$ and $n_2 = 3\,\mathrm{Re}(\chi_{xxxx}^{(3)})/8n_0$ are the linear and nonlinear refractive indices, respectively. In this case, the dispersion will also become nonlinear. The last equality of eq. 2.18 is valid assuming that the nonlinearity is small (and hence the Taylor series expansion can be truncated in the first term). The Kerr effect is responsible for a number of nonlinear effects, such as SPM (modulation of the phase of the own optical field with the applied intensity), XPM (modulation of the phase of another field), MI (pulse breakup in a train of soliton under the combined effect of SPM and anomalous dispersion) or self-focusing (Kerr lens). All these effects can be used for supercontinuum generation (generation of a wide spectrum of wavelengths from a coherent input beam). When working with optical fibres, the nonlinear phases introduced by SPM and XPM are usually expressed as a function of the nonlinear coefficient of the fibre γ, defined as

$$\gamma = \frac{\omega_n n_2}{c A_{eff}}, \tag{2.19}$$

where A_{eff} is the effective area of the guided mode of frequency ω_n.

Another important third-order nonlinear parametric process is Four-Wave Mixing (FWM) in which two or more electromagnetic waves exchange energy and generate new frequency components at frequencies that are natural combinations of the frequencies of the input beams. Since FWM is a coherent process, its efficiency is strongly dependent on the relative phases and polarizations of the interacting waves. The process is therefore sensitive to the dispersion of the medium and the phases added by SPM and XPM effects. Owing to its nature, the effects of FWM gain relevance in multichannel communication systems. The crosstalk (exchange of energy between channels) and generation of new frequency channels caused by FWM is usually an undesired effect that can degrade the signal in this type of systems. In single channel systems, however, the occurrence of spontaneous degenerate FWM (FWM process where two of the initial waves have the same frequency) is possible between a strong pump wave and the optical noise in a spectral region close to it. In fact, the appearance of two gain sidebands symmetrically placed around the central wavelength caused by MI in single channel systems is a process which resembles a Degenerate FWM (DFWM) process phase-matched by the nonlinear phase introduced by SPM.

2.3.2.1 Modulation Instability (MI)

MI results from the interplay of Kerr effect and anomalous GVD, and, in the time domain, results in the breakup of a continuous wave (CW) beam into a train of ultra-short pulses. In the spectral domain, MI results in the appearance of two gain sidebands on each side of the central wavelength. In fibres, MI has been demonstrated a long time ago [15] and can present a serious limitation in distributed sensing due to the large spans of fibre usually involved. MI has been shown to limit the performance of distributed fibre sensors based on stimulated Brillouin scattering (SBS) [16] and ϕOTDR [2].

In order to explain the origin of MI, we start by describing the propagation of a quasi-monochromatic ($\Delta\omega/\omega_0 << 1$) optical pulse with a central angular frequency ω_0 and width $\Delta\omega$ in nonlinear dispersive fibres. This can be described by solving the Nonlinear Schrödinger equation (NLSE):

$$\frac{\partial A(z,T)}{\partial z} + \frac{i\beta_2}{2}\frac{\partial^2 A(z,T)}{\partial T^2} - \frac{\beta_3}{6}\frac{\partial^3 A(z,T)}{\partial T^3} + \frac{\alpha}{2}A(z,T) = i\gamma \mid A(z,T)\mid^2 A(z,T), \qquad (2.20)$$

where $T = t - z/v_g \equiv t - \beta_1 z$, where t is time and z the fibre position, i.e., a frame of reference moving with the pulse at the group velocity v_g is used. A(z,t) is the scalar envelope of the electric field, assumed to be a slowly varying function of z and normalized such that $|A|^2$ = optical power of the pulse (P_0). Assuming that the carrier wavelength is not too close to the zero-dispersion wavelength and a pulse temporal width >5 ps, the contribution of β_3 can be neglected. If the fibre losses are neglected (α=0), a simplified version of eq. 2.20 can be derived [17]:

$$\frac{\partial A(z,T)}{\partial z} + \frac{i\beta_2}{2}\frac{\partial^2 A(z,T)}{\partial T^2} = i\gamma\,|A(z,T)|^2\,A(z,T)\,. \tag{2.21}$$

If A(z,T) remains constant over time during its propagation along the fibre, then a steady-state solution can be easily derived:

$$A(z,T) = \sqrt{P_0}\,e^{iP_0\gamma z}\,. \tag{2.22}$$

This solution, however, is not stable against perturbations. It can be demonstrated that small perturbations *a(z,T)* in *A* will evolve as

$$a(z,T) = a_1 \exp[i(Kz - \Omega T)] + a_2 \exp[-i(Kz - \Omega T)] \tag{2.23}$$

where K and Ω are, respectively, the wave number and the angular frequency of the perturbation a(z,T) which satisfy the dispersion relation [17]

$$K = \pm\frac{1}{2}\,|\beta_2\Omega|\sqrt{\Omega^2 + \frac{4\gamma P_0}{\beta_2}}\,. \tag{2.24}$$

The mathematical demonstration of this result is not trivial and is beyond the purpose of this theoretical introduction, but a more extensive explanation can be found in ref. [17]. The physical meaning, however, can be easily understood when considering the factor $e^{i(\beta_0 z - \omega_0 t)}$, which was factored out in this presentation. In this case, the real wave numbers and angular frequencies of the perturbation a(z,T) are, respectively, $\beta_0 \pm K$ and $\omega_0 \pm \Omega$. So a perturbation a results in the appearance of new spectral components in the optical pulse spectrum, symmetrically placed around the pulse central angular frequency ω_0. The amplitude of these new spectral components is stable if K has a real value (i.e., if $\Omega^2 > -\frac{4\gamma P_0}{\beta_2}$). However, for negative values of β_2 (anomalous GVD), K becomes

imaginary for frequencies below a critical angular frequency $\Omega_c = \left|\sqrt{\frac{4\gamma P_0}{\beta_2}}\right|$, and the amplitude of these perturbation frequencies grows exponentially with z. In this case, the appearance of spectral sidebands symmetrically placed around ω_0 is bound to occur for any initial P_0 for a sufficiently large z. The gain spectrum g(Ω) due to MI is then given by

$$g(\Omega) = |\beta_2 \Omega| \sqrt{\left|\frac{4\gamma P_0}{\beta_2}\right| - \Omega^2}\,, \tag{2.25}$$

The spectrum of $g(\Omega)$ is shown in Fig. 2.3 using typical parameters of a standard SMF: β_2=-22.8 ps^2km^{-1}, γ=1.3 $W^{-1}km^{-1}$ and P_0=1.25 W (same parameters which were used in section 3.4 to simulate the propagation of a pulse along the fibre).

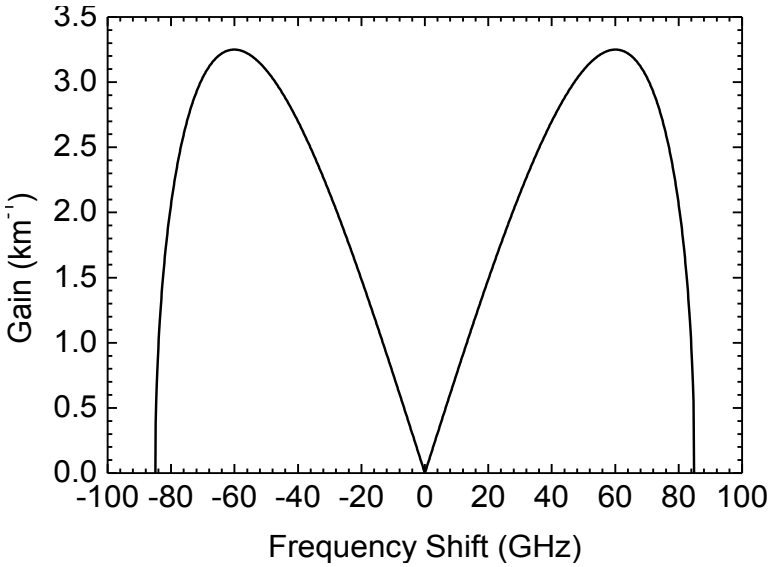

Fig. 2.3 Gain spectrum induced by MI using the parameters of a typical SMF.

This process can be thought off as a degenerate FWM process, where two photons from the central angular frequency ω_0 are destroyed to create two photons of angular frequency ω_0-Ω and ω_0+Ω. In this case, the process is phase-matched by the nonlinear phase ($P_0.\gamma z$) which is introduced by SPM.

In the time domain, as a result of MI, a CW will be converted into a periodic pulse train with a period [9]: $T = 2\pi\sqrt{2}/\Omega_c = 2\pi\left|\sqrt{\beta_2/(2\gamma P_0)}\right|$. This can be used to generate stable ultra-short pulses with a periodicity that can be tuned by the CW power (P_0).

2.4 Scattering

When travelling in a medium, light can be deflected from its straight trajectory due to the interaction with the atoms and molecules that constitute it. This phenomenon is known as scattering. At a quantum-mechanical level, scattering can be explained as the absorption of an incident photon by an atom/molecule which then emits another photon that can have a different direction/frequency/phase from that of the incident photon.

In optical fibres, different types of scattering can occur, which can be classified according to the nature of the interaction. Depending on whether energy is exchanged between the medium and the incident photons, the scattering can be elastic or inelastic:

- Elastic scattering: The incident and scattered photons have the same energy (and therefore the same frequency) and there is no exchange of energy with the medium. However, since the scattered photon can have a different direction of propagation from that of the incident photon, the medium can absorb momentum.
    - Rayleigh scattering: Scattering from non-propagating density fluctuations. In optical fibres Rayleigh scattering is one of the main mechanisms leading to losses, as discussed in section 2.2.1.
- Inelastic scattering: The incident and scattered photons have different energies (and therefore different frequencies). Since the overall energy of the process must be conserved, only differences of energy between the incident and scattered photons which can be absorbed/released by the medium are allowed. If the energy of the incident photon is higher than the energy of the scattered photon (i.e. the medium absorbs energy), the process is called Stokes scattering, and if it is lower (i.e. the medium releases energy), the process is called Anti-Stokes scattering.
    - Raman scattering: A molecule of the medium scatters a photon with different frequency of the incident photon. The energy difference is absorbed/released by the molecule which transits to a higher/lower energy vibration state.
    - Brillouin scattering: An electromagnetic wave is reflected by an acoustic wave propagating in the medium and its frequency is shifted due to the Doppler effect. The energy difference is compensated by the

creation/destruction of an acoustic phonon, thus increasing/decreasing the amplitude of the acoustic wave.

A schematic representation of energy variations for elastic and inelastic (Stokes and Anti-Stokes) photon scatterings by the medium of propagation is presented in Fig. 2.4.

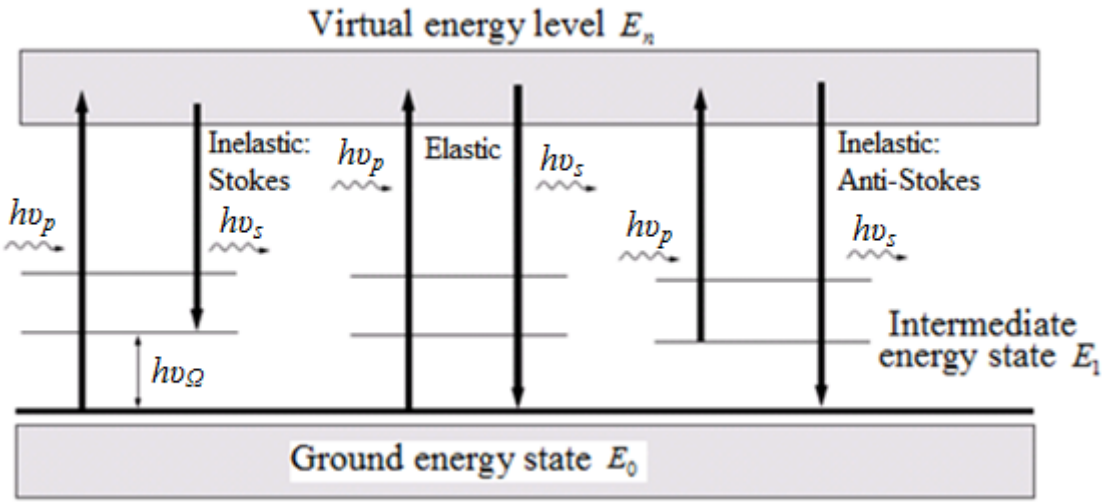

Fig. 2.4 Energy variations for different types of scattering (Adapted from ref. [18]).

In fibre optics, Rayleigh, Brillouin and Raman scattering can set limitations or be used in an advantageous manner, depending on the specific context. Rayleigh and Raman scattering are extensively used in the work developed in this thesis, and are therefore thoroughly described in the subsections below.

2.4.1 Elastic scattering: Rayleigh scattering

Rayleigh scattering is the elastic scattering of light by density fluctuations with a size much smaller than its wavelength (typically <10 %). For individual molecules and unpolarized incident light, the intensity of the scattered light (I_s), as a function of the angle between the incident and scattered light (θ), can be derived to be [9]:

$$I_s(\theta) \propto 1+\cos^2(\theta). \tag{2.26}$$

I_s will be maximum for θ=0 (forward scattering) and θ=π (backward scattering) and will decrease continuously as θ approaches the minima of the lateral scattering at θ= ±π/2. Such description can be used for the scattering of light in a low density medium (such as a dilute gas). In a dense medium, however, the interference of light coming from different scattering centres will play an important role, and eq. 2.26 may not be valid. In fact, in a dense and perfectly homogeneous medium, destructive interference will occur

for light scattered in all directions except for forward scattering [7], which is the basis of the origin of the refractive index.

However, if the medium is not perfectly homogeneous, perfectly destructive interference will no longer occur due to the presence of inhomogeneities and scattering can occur in all directions (Fig. 2.5). This will be the case of optical fibres, where the presence of inhomogeneities resulting from the fabrication process (fluctuations in the material density or dopant concentrations, impurities, etc) will result in losses due to laterally Rayleigh scattered light. These losses are dominant at short wavelengths since the intensity of the Rayleigh scattered light is proportional to $1/\lambda^4$.

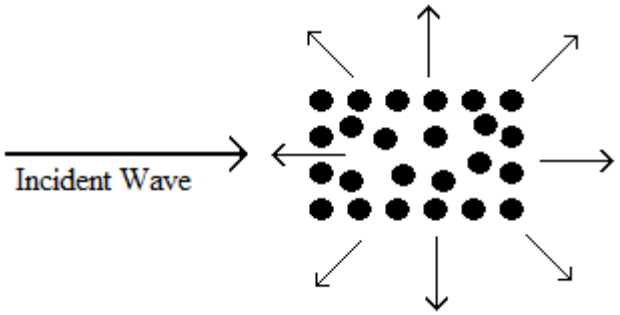

Fig. 2.5 Rayleigh scattering of light propagating in a dense inhomogeneous medium.

2.4.1.1 Rayleigh Backscattering

When an optical wave propagates in a fibre, a small fraction of the Rayleigh scattered light is coupled back into the fibre in the opposite direction ($\theta=\pi$) of the initial wave. This phenomenon is called Rayleigh backscattering and will create a counter-propagating wave with the same frequency of the initial wave (Fig. 2.6). The typical Rayleigh backscatter coefficient ($\alpha_{\text{Rayleigh Backscatter}}$) in SMF is ≈-72 dB/m. While this effect can be detrimental, introducing noise in optical communications or causing instability in high coherence lasers, it can also be used advantageously: it is the basis of OTDR (which can be used for distributed sensing of different parameters, as discussed in section 3.2.2) and it can also be used as a distributed mirror to assist Raman fibre lasers (RFLs) (as discussed in chapter 5).

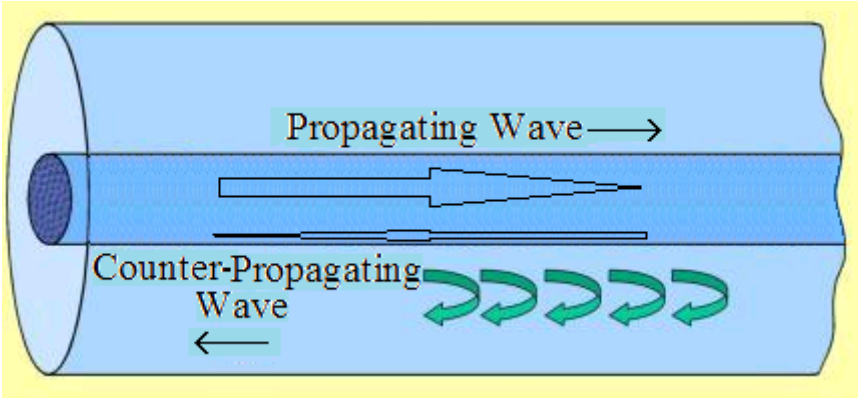

Fig. 2.6 Counter-propagating wave generated by Rayleigh backscattering in fibres.

The Rayleigh backscattered wave can in turn generate Rayleigh scattering, and a secondary Rayleigh backscattered wave (double Rayleigh backscatter). However, given the low value of $\alpha_{\text{Rayleigh Backscatter}}$, multiple Rayleigh backscattered reflections are negligible in most practical situations.

2.4.2 Inelastic scattering: Raman Scattering

In Raman scattering an electromagnetic wave is inelastically (i.e. without photon energy conservation) scattered by molecules in the medium of propagation. In fibre optical communication systems it is an undesired effect, since it can generate and amplify noise. However, Raman scattering can also be used for numerous applications such as determining the energy of vibrational modes of a medium by observing the Raman gain spectrum. In optical fibres, Raman scattering can be used to amplify signals with a pump of different frequency and thus compensate for fibre losses, or create ultralong Raman fibre lasers (as discussed in sections 3.5 and 3.6, and chapter 5).

2.4.2.1 Spontaneous Raman scattering

If the optical scattering properties of the medium are not modified by the incident optical intensity, the process is called spontaneous scattering. In this case, the properties and probability of scattering of each photon are independent of the properties and intensity of the incident optical wave. Spontaneous Raman scattering was discovered by C.V. Raman in 1928 and can occur in any molecular medium. In condensed matter, the spontaneous Raman scattered power ratio to the incident radiation is typically $\sim 10^{-6}$ cm^{-1}.

Raman scattering can be explained at a quantum-mechanical level. In the case of Stokes Raman scatter, a molecule/atom of the medium absorbs a photon of the incident (or pump) radiation with a frequency v_p, and transits to a virtual higher energy level E_n.

Then, the molecule/atom transits to a state of energy E_1 higher than the initial ground state E_0, emitting a photon (signal radiation) with a frequency v_s lower than the pump photon. The energy and momentum differences between the pump and the signal photons are therefore compensated by the molecule/atom, which absorbs a phonon of frequency Ω. Raman anti-Stokes scatter occurs in a similar way, but the initial state of the molecule/atom has a higher energy than the final state, and therefore the signal photon has a higher frequency than the pump photon (see Fig. 2.4). Since the upper levels are virtual, the incident and scattered photons can have any frequency, as long as the energy difference between them ($h\Omega$), where h is the Planck constant, can be absorbed/released by the medium.

The rates at which the Stokes (W_S) and Anti-Stokes (W_{AS}) scatterings occur in thermal equilibrium are proportional to the population of the states with energy E_0 and E_1 and, therefore, the ratio between these quantities is given by the Boltzmann factor [19]

$$\frac{W_{AS}}{W_S} = e^{-\frac{h\Omega}{k_B T}}, \tag{2.27}$$

where k_B is the Boltzmann constant and T is the absolute temperature. Depending on the frequency shift Ω, the Raman Anti-Stokes rate of scattering can be much lower than the Raman Stokes scattering rate at room temperatures. Also, since the Boltzmann factor is strongly dependent on the temperature, the ratio between Stokes and Anti-Stokes Raman scatterings can be used to determine the temperature along optical fibres [20].

2.4.2.2 Stimulated Raman Scattering (SRS)

If high radiation intensities already exist in the medium in the Raman gain spectrum, the Raman scattering process will occur in the presence of seed photons (Fig. 2.7) and the process is called Stimulated Raman Scattering (SRS). In this case, not only does the scattered radiation tend to have the same frequencies of the pre-existent radiation, but the scattering rate is also much higher, becoming intensity dependent [7].

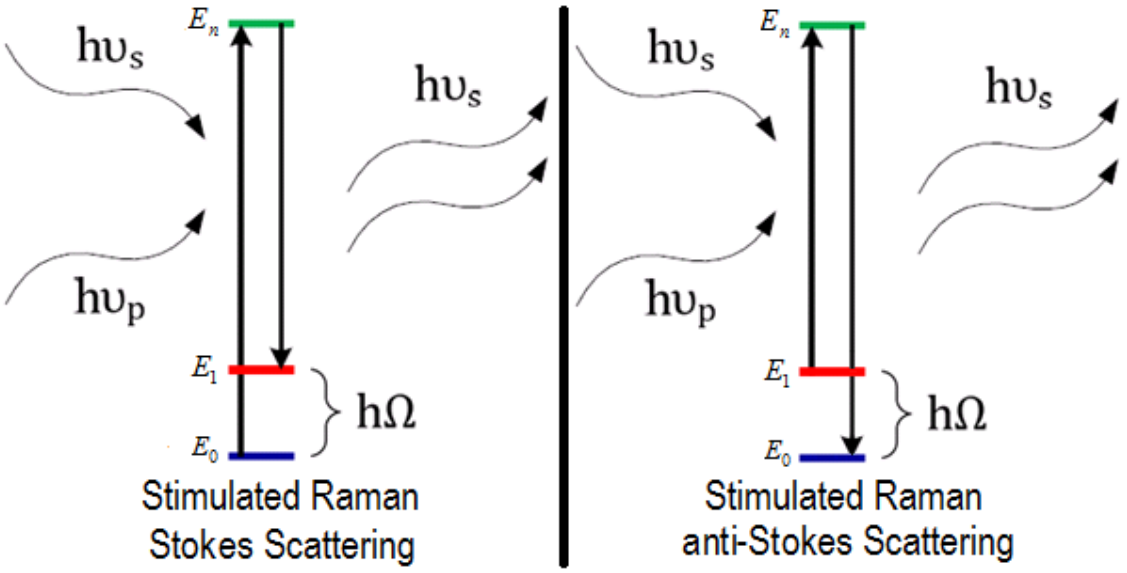

Fig. 2.7 Stimulated Raman a) Stokes and b) anti-Stokes scattering.

SRS was discovered by Woodbury and Ng (1962), and later described in more detail by Eckhardt et al. (1962) [21], and can be used to amplify a signal (υ_s) in the medium with a Raman pump (υ_p) of different frequency. In this case, the Raman amplification can be described by

$$\frac{dI_S}{dz} = g_R(\Omega) I_s I_p, \tag{2.28}$$

where $g_R(\Omega)$ is the Raman gain for the frequency shift Ω (see Fig. 2.8), and I_s and I_p are the intensities of the signal and Raman pump, respectively. Therefore, the pre-existent radiation experiences an exponential growth, in a similar process to the stimulated emission of a laser.

SRS is a process with some similarities to fluorescence in erbium doped fibres, which can also be used to amplify optical signals. In this case, however, the upper level is real, and therefore the pump and scattered photons will only have certain allowed energy (and frequency) levels, while in SRS the incident and scattered photons can have any frequency, as long as the frequency difference between them is Ω. On the other hand, the time that the molecule spends in the E_n level is longer than in the case of a virtual level. Therefore, the probability of the fluorescence process to occur in the presence of other photons is higher than in Raman scattering, and the threshold intensity for stimulated emission will be lower for fluorescence.

2.4.2.3 Raman Gain Spectrum

In a molecular medium, there are several vibrational modes with different energies. Since the energy difference between incident and scattered photons is absorbed/released by molecules of the medium, these modes will determine the Raman gain spectrum, i.e., the Raman scattering frequency shifts allowed and scattering rates for each frequency, characteristic of the medium. In crystalline materials, these vibrational modes have well defined energies and are associated with specific Raman frequency shifts. In this case, $g_R(\Omega)$ is typically a set of narrowband peaks at well-defined frequencies. In amorphous materials, however, the energy of vibrational modes can spread out and overlap of different bands can generate a continuum. This is the case of amorphous fused silica (the basic material of silica fibres), whose Raman gain spectrum is a continuum that extends up to 40 THz [9], with a maximum at around 13 THz and a local maximum peak at around 14.5 THz. The typical Raman gain spectrum for fused silica using a pump wavelength λ_p=1 μm is presented in Fig. 2.8.

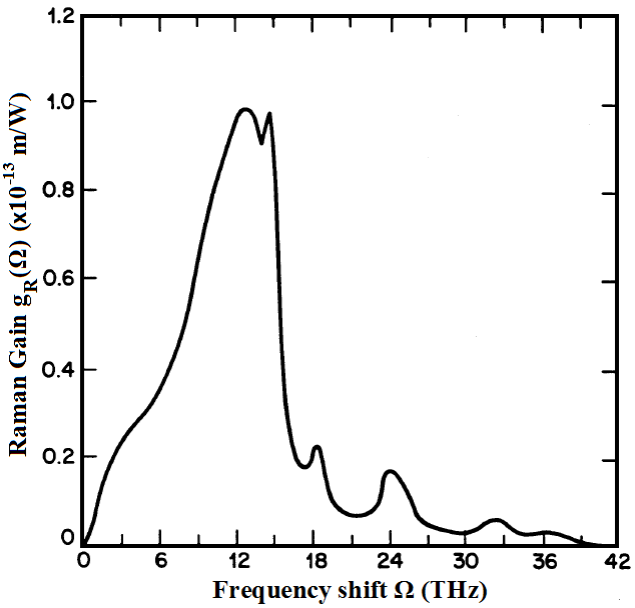

Fig. 2.8 Raman gain spectrum $g_R(\Omega)$ for fused silica (Adapted from ref. [9]).

Using several Raman pump lasers with different frequencies, their gain spectra will overlap. Therefore, with a careful choice of these frequencies and intensities, a flatter broadband Raman gain spectrum can be obtained. The Raman gain generated by a primary Raman pump has also been used as a secondary Raman pump to generate a second-order Raman gain spectrum [22]. In this case, the second-order Raman gain spectrum will have twice the frequency shift from the primary Raman pump.

2.4.2.4 Intensity evolution and threshold for noise amplification

When a Raman pump (frequency υ_p, intensity I_p, loss α_p) is used to amplify a signal (frequency υ_s, intensity I_s, loss α_s) along an optical fibre (z) using SRS, the variations of the intensities of the two waves, in the CW case, are described by the two following coupled equations [9]:

$$\frac{dI_p}{dz} = -\frac{\upsilon_p}{\upsilon_s} g_R(\Omega) I_s I_p - \alpha_p I_p \tag{2.29}$$

$$\frac{dI_S}{dz} = g_R(\Omega) I_s I_p - \alpha_s I_s . \tag{2.30}$$

Assuming that $I_p >> I_s$, the Raman pump depletion (variation of I_p due to the gain provided to I_s) can be neglected [23], and eq. 2.29 and 2.30 are then modified to

$$\frac{dI_p(z)}{dz} = -\alpha_p I_p \tag{2.31}$$

$$\frac{dI_S}{dz} = g_R(\Omega) I_s I_{p0} e^{-\alpha_p I_p} - \alpha_s I_s . \tag{2.32}$$

From which the evolution of the I_p and I_s along the fibre (z) can be derived, setting as boundary conditions the initial intensities of Raman pump (I_{p0}) and signal (I_{s0}) at the fibre beginning (z=0):

$$I_p(\mathrm{z}) = I_{p0} \cdot e^{-\alpha_p z} \tag{2.33}$$

$$I_S(\mathrm{z}) = I_{s0} \cdot \exp\left(g_R(\Omega) I_{p0} \left[\frac{1 - e^{-\alpha_p z}}{\alpha_p} \right] - \alpha_s z \right). \tag{2.34}$$

From this solution, it is derived that a reduction of the effective interaction length (z_{eff}) occurs due to α_p:

$$z_{\mathrm{eff}} = \left[\frac{1 - e^{-\alpha_p z}}{\alpha_p} \right]. \tag{2.35}$$

z_{eff} will be lower than z, and for long fibre lengths ($\alpha_p z >> 1$) z_{eff} is reduced to $1/\alpha_p$, which is of the order of ≈20 km for a typical fibre loss, at 1550 nm, of α_p ≈0.047 km^{-1} ≈0.2 dB/km.

A theoretical model and numerical calculations of the evolution of the intensities of the Raman pump and of the signal along an optical fibre is presented in section 3.4. In this simulation, two counter-propagating Raman pumps are launched from each end of the fibre.

From eq. 2.34 it is derived that if there is no signal launched at the fibre entrance (i.e., I_{s0}=0), SRS should not occur. In this case however, spontaneous Raman scattering will generate radiation which will then act as a seed that will be amplified though SRS. A broadband spectrum is generated this way, which can build up to high intensities if the Raman pump is strong enough.

This process can be modelled using a fictitious photon in each frequency mode of the $g_R(\Omega)$ at z=0, from which it can be derived that the threshold Raman pump power (P_{p0}^{th}), defined as the Raman pump power at which the amplified spectrum power becomes equal to the Raman pump power at the end of the fibre, is given by [9]:

$$P_{p0}^{th} = 16\frac{A_{\text{eff}}}{g_R \cdot z_{\text{eff}}} \tag{2.36}$$

Using the typical values of a SMF at a wavelength of 1550 nm (effective mode area A_{eff}=50 μm^2, g_R=6.6·10^{-14} m/W) for a long fibre length ($\alpha_p z$>>1, z_{eff} ≈1/α_p ≈20 km), a threshold Raman pump power of P_{p0}^{th}≈600 mW can be estimated.

3 Phase-sensitive OTDR (ϕOTDR) for distributed vibration sensing

3.1 Introduction

In this chapter, we present an extensive investigation on the use of phase-sensitive optical time domain reflectometry (ϕOTDR) for distributed vibration sensing, which includes experimental and theoretical descriptions using different configurations.

Firstly (section 3.2), in order to clarify the context of the technique to the reader, the principles of operation and a detailed state-of-the-art of the use ϕOTDR for distributed vibration sensing is presented, comparing the problems and performance trade-offs between previously reported configurations. Then, an overview of the characteristics and performance of the different existing distributed fibre optic sensors (DFOS) is presented in order to provide a frame for comparison between ϕOTDR and other DFOS.

Then (section 3.3), the ϕOTDR operation is described under normal operation. A theoretical model describing the signal statistics, fading probability and noise, is presented and used for comparison with the experimental results. The performance of the ϕOTDR is then characterized for distributed vibration sensing. Distributed measurement of ultrasonic vibrations is achieved, to the best of our knowledge, for the first time.

Next (section 3.4), a study aimed to identify the limitations in terms of ϕOTDR pulse peak power, imposed by nonlinearities, is presented. MI is identified as the first nonlinear effect to arise under normal operation conditions and its impact on the performance of ϕOTDR is thoroughly described, both theoretically and experimentally. This study provides an important basis for understanding the problems and limitations of this system, and thus it helps to maximize its performance when used for both dynamic and static measurements.

In the last two sections of this chapter, the uses of first-order (section 3.5) and second-order (section 3.6) Raman amplification to assist ϕOTDR operation, with the intent of greatly increasing the sensing range, are described and compared. Using first-order Raman assistance (section 3.5), the ϕOTDR pulse is optically observed at different points, thus clearly depicting its evolution along the setup and evidencing the impact of the different setup components on it. The quality of the obtained ϕOTDR trace along the fibre is evaluated using different Raman pump powers and compared with the theoretical predictions. The noise is characterized both optically and

electrically, with special emphasis being given to the RIN transfer from the Raman pumps. Then, vibration measurements performed over 110 km and 125 km of SMF are described. In section 3.6, the performance of the sensor is compared with a scheme using ϕOTDR assisted by second-order Raman amplification under similar measurement conditions.

The main results presented in this chapter were published in Optics Letters and Journal of Lightwave Technology [2, 3, 5].

3.2 ϕOTDR: Principles, Limitations and State-of-the-art

In this section, the principles of operation, historical evolution, limitations and state-of-the-art of ϕOTDR operation, including an explanation of the characteristics and performance trade-offs between different configurations, are presented. The challenges and solutions to increase the range and the bandwidth of ϕOTDR for dynamic measurements are also discussed. Lastly, an overview of the evolution of the performance of the reported ϕOTDR sensors is presented and the technique is compared with other distributed sensor schemes.

The possibility to use ϕOTDR for static measurements (such as temperature, strain or birefringence) is discussed in chapter 4.

3.2.1 ϕOTDR principle of operation

ϕOTDR works very similarly to a traditional Rayleigh based OTDR, but uses coherent light (linewidth below a few MHz) instead of broadband (incoherent) light. In both cases, light pulses are sent to the fibre and the backscattered signal is analyzed in the time domain, at the same fibre end. The backscattered signal is associated with a position along the fibre, based on the time of flight between the sent pulse and the detection of the backscattered signal. A simplified setup of an OTDR is shown in Fig. 3.1.

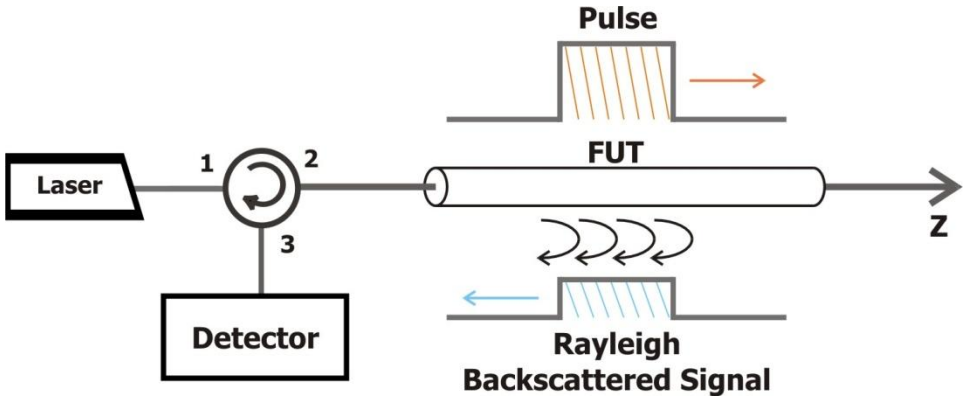

Fig. 3.1 Setup of an OTDR based system. FUT: fibre under test.

In order to explain the operation of OTDR based systems, a schematic evolution of the pulse propagation along the fibre and the respective backscattered signal generated are shown in Fig. 3.2. A light pulse travelling with group velocity $V_g = c / n_g$ (where c is the speed of light in the vacuum and n_g is the group refractive index of the fibre) with a temporal width Δt (spatial width $W = \Delta t \cdot V_g$), which has its front edge (F) sent from the

fibre beginning z=0 and the time t=0, is considered. The back edge (B) of the pulse will therefore enter the fibre at the time $t=\Delta t$.

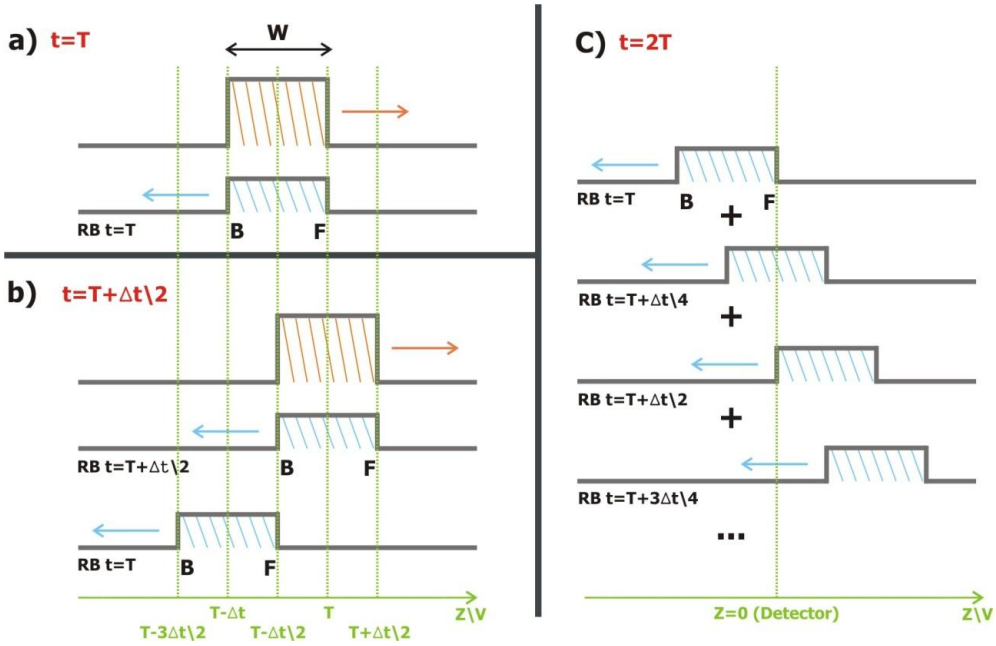

Fig. 3.2 Propagation of an OTDR pulse in the fibre and respective Rayleigh backscattered signal generated at a time: a) t=T; b) t=T+Δt/2.; c) the backscattered signals reflected at different times reaching the detector (z=0) at t=2T.

Assuming, for simplicity, that the Rayleigh scattering centres along the fibre are homogeneously distributed, each part of the pulse (of infinitesimal width) will generate a counter-propagating Rayleigh backscattered wave when the pulse travels in the fibre. At each instant t, a backscattered signal with the same width W of the initial pulse will be generated from the fibre position reached by the pulse. The backscattered signal is therefore continuously generated, and different parts of backscattered signals generated at different instants can overlap.

At an arbitrary time $t=T$, the pulse is located at $z=[T-\Delta t;T]\cdot V_g$, and therefore generates a Rayleigh backscattered signal (RB t=T) at the same position (Fig. 3.2a). At a later time $t=T+\Delta t/2$, another Rayleigh backscattered signal is created (RB t=T+Δt/2) at $z=[T-\Delta t/2;T+\Delta t/2]\cdot V_g$, and the RB t=T has moved to $z=[T-3\Delta t/2;T-\Delta t/2]\cdot V_g$ (Fig. 3.2b). In this case, the front edge of RB t=T and back edge of RB t=T+Δt/2 are overlapped and will be detected at the same time. The signal received at a detector placed at the beginning of the fibre (z=0) at the instant $t=2T$ will be the sum of the incoming Rayleigh backscattered signals between the front edge of the RB t=T and the back edge of the RB t=T+Δt/2 (Fig. 3.2c).

In this case, the detected signal at $t = 2T$ will be the sum of the fields reflected from the scattering centres contained in the fibre section $z = [T - \Delta t/2; T] \cdot V_g$ (which were reflected in the time interval $t = [T; T + \Delta t/2]$) and perturbations occurring in this fibre section are indistinguishable as they will equally affect the detected signal. The spatial resolution of the sensor is therefore half of the spatial pulse width:

$$\text{Spatial Resolution} = \frac{W}{2} = \frac{\Delta t \cdot c}{2n_g}. \tag{3.1}$$

Using a typical value for silica fibres of n_g=1.46, the spatial resolution will be 10.3 m for a 100 ns pulse width.

In order to avoid the superposition of backscattered signals, only one pulse can travel in the fibre at a time. The repetition rate at which pulses are sent to the fibre is, therefore, limited by the (roundtrip) flight time of the pulse in the fibre, which is limited by the fibre length L:

$$\text{Maximum Pulse Repetition Rate} = 2L\frac{n_g}{c}. \tag{3.2}$$

As an example, monitoring a length of 0.97 km of fibre requires the pulse repetition rate to be below 100 kHz (each trace is 10 μs long), which limits the maximum readable frequency at each position to 50 kHz, as given by Nyquist –Shannon theorem.

The difference between conventional OTDR and ϕOTDR can be understood by calculating the optical intensity I resulting from the addition of two waves $\vec{E}_1, \vec{E}_2$ with amplitudes E_1, E_2 and frequency ω:

$$I(t) \propto \left|\vec{E}_1(t)e^{i\omega t} + \vec{E}_2(t)e^{i\omega t + \Delta\varphi(t)}\right|^2 = E_1(t)^2 + E_2(t)^2 + 2E_1E_2\cos\left(\theta_p(t)\right)\cos\left(\Delta\varphi(t)\right), \tag{3.3}$$

where $\theta_p(t)$ is the relative polarization angle and $\Delta\varphi(t)$ the phase difference between the two waves. In the case of conventional OTDR, the reflected fields interfere incoherently, i.e., the phase difference $\Delta\varphi(t)$ between the two waves is randomly varying over time, and the interference term is averaged away. For this reason, an OTDR presents a smooth trace which is only sensitive to intensity variations (Fig. 3.3a). In a ϕOTDR, however, due to the use of highly coherent light, the reflected fields interfere coherently and the interference terms have a fixed value, dependent on

$\Delta\varphi(t)$. The optical intensity of the detected signal is therefore sensitive to the changes in the relative phases among the reflected fields. Since the position of the scattering centres is randomly distributed along the fibre, the ϕOTDR trace typically has random oscillations around the average reflected power (Fig. 3.3b).

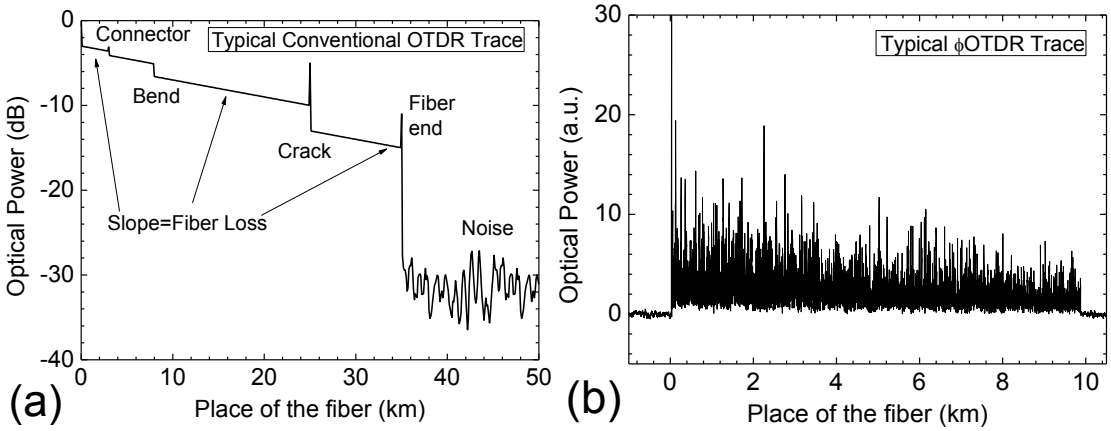

Fig. 3.3 Typical trace of: a) conventional OTDR; b) ϕOTDR.

In OTDR operation, this random pattern is a detrimental feature called fading or coherent noise [24], but for ϕOTDR it constitutes the core of its operation. This pattern remains constant over time if the scattering centres do not suffer any change, as a "fingerprint" of the fibre. However, if the relative phases among the reflected fields coming from the different scattering centres are changed at a given location due to a disturbance (e.g. due to local strain or temperature changes), the ϕOTDR trace at that

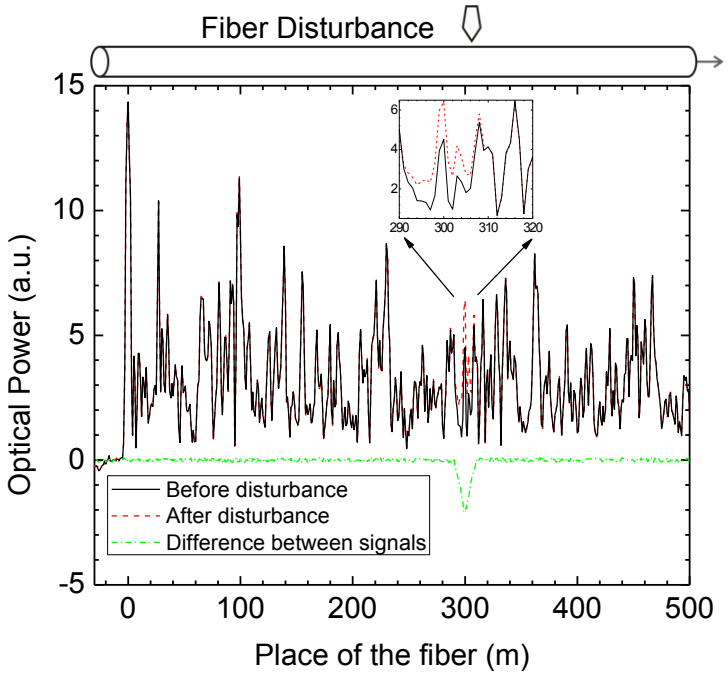

Fig. 3.4 ϕOTDR trace before and after a disturbance occurs at a point in the fibre.

position (but only at that position) will vary (Fig. 3.4). In the case of localized vibrations, the ϕOTDR trace will show local variations synchronized with the vibration frequency.

An important feature of ϕOTDR operation is that the signal detected from one point in the fibre is completely independent from the signal originated from another point (as long as the two points distance is not within the spatial resolution of the sensor). This is an important advantage when compared to other systems which present cumulative effects along the fibre, such as OTDR (in which the detection of a signal requires an intensity variation and therefore a decrease of the sensing range) or polarization OTDR (POTDR) (where an event at one point affects the entire fibre signal after that point), as discussed in section 3.2.8.

3.2.2 ϕOTDR Historical Perspective

Nowadays, the phase-sensitive OTDR designation is the most commonly used in the scientific literature to refer to an OTDR using highly coherent light, although a few early papers used simply "phase-OTDR" [25, 26]. Authors have also used coherent OTDR (COTDR) [27] to refer to an OTDR using heterodyne (also called coherent) detection and highly coherent light. Commercial systems often use "distributed acoustic sensing" to refer to the distributed detection of vibrations along optical fibres, usually using ϕOTDR.

ϕOTDR was initially introduced by Henry F. Taylor and Chung E. Lee in 1993 as a powerful tool for fibre optic intrusion sensing [28]. The invention described a system sensitive to the phase modulation of the light which exploited a phenomenon (coherent interference of light) previously regarded as a detrimental effect in OTDR operation (fading or coherent noise) [24], for sensing purposes. Despite being proposed over two decades ago, the principles of operation remain the same in modern configurations: highly coherent light pulses are injected into a fibre and the backscattered signal is observed in the time domain.

Following preliminary experimental results which confirmed the potential for intrusion detection [29, 30], the same authors investigated and thoroughly characterized a spectrally stable Er-Fibre laser with the specific intent of application in ϕOTDR operation [31] which used a long (25 km) optical-feedback loop to achieve a narrow

linewidth (<3 kHz) and low frequency-drift rate (<1 MHz/min). Using this type of laser, a ϕOTDR with enough sensitivity to detect people walking on top of a buried fibre in field tests [32] was later demonstrated. The used setup is presented in Fig. 3.5. Although the features of 1 km spatial resolution over 12 km were rather modest, this was historically an important test which presented a clear demonstration of the potential of ϕOTDR in practical applications. The tests were later improved to include the detection of intruders on foot and vehicles over 19 km with 200 m spatial resolution [33].

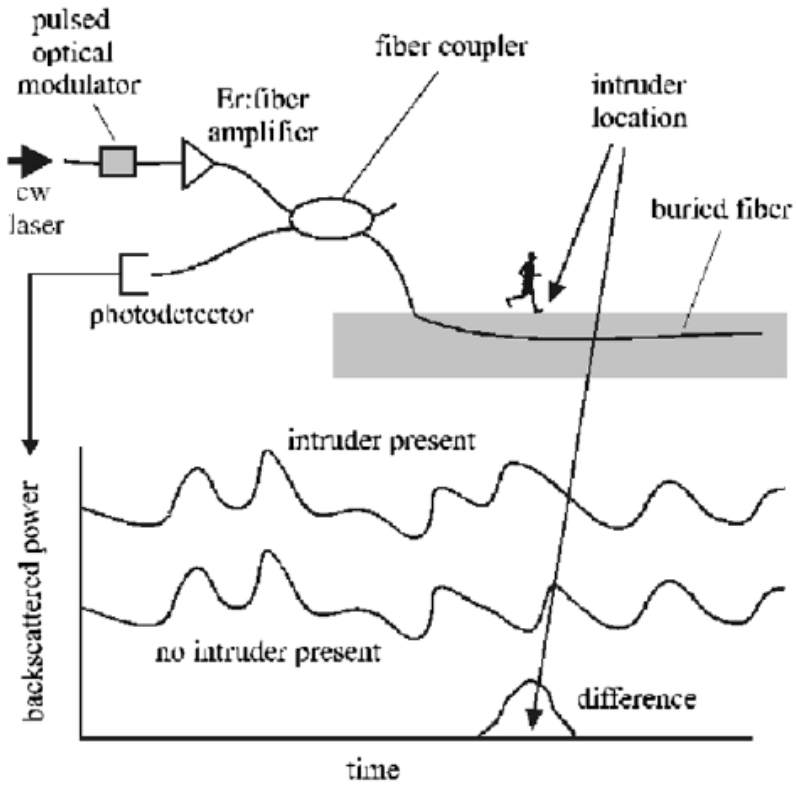

Fig. 3.5 ϕOTDR setup used for intrusion sensing in fields tests (adapted from ref. [32]).

Another important initial demonstration of the potential of ϕOTDR was presented by Shatalin, et al., when the technique was used for the detection of piezoelectrically induced length changes and rapidly increasing temperatures. The potential to perform measurements with spatial resolutions similar to those of a conventional OTDR, with more than 1000 resolved points over distances of ~10 km, was demonstrated [34].

3.2.2.1 Events and vibration detection

After the initial demonstration of ϕOTDR, intense research in the subject has been developed by several institutions around the world [25],[32],[35],[36],[37],[38],[3]. A number of schemes have been proposed to improve the performance of ϕOTDR not

only for dynamic but also for static measurements [27]. The characterization of ϕOTDR for dynamic measurements reported in the literature can generally be divided into the detection of events and vibrations.

The detection of events corresponds to the application of a discrete perturbation at a given time (an impact such as a pencil break next to the fibre [25], hitting a pipe [38], or footsteps [39]) and then observing the changes of the trace in the time domain. The signal-to-noise ratio (SNR) is given by the ratio of the maximum power variation of the trace (signal) against the power fluctuations of the trace at a different time/spatial point when/where the impact is not felt (noise). Averaging of the trace is usually used to reduce the noise and highlight low frequency signals.

As for the detection of vibrations, it is usually produced by applying a pure vibration (usually stationary, although the detection of non-stationary vibrations has also been characterized [40]), using a piezoelectric element (PZT) [41],[38] or a mechanical actuator [3], and monitoring the signal in the frequency domain. In this case, the SNR is given by the amplitude of the central frequency (signal) against the amplitudes of the rest of the frequency spectrum (noise). The use of trace averaging is avoided as it decreases the detection bandwidth of the system.

Surely the frequency spectrum of an event, and variations over time of a pure frequency, can also be analyzed, but the detection of events is typically more associated with intrusion detection, while the detection of vibrations can be used to properly characterize the true frequency bandwidth of the detection system, rather than simply estimating it based on the pulse repetition rate (eq. 3.2). It is used, as well, for the characterization of complex signals (for instance, distinguishing patterns corresponding to different types of machinery), having also important applications in structural health monitoring.

3.2.3 Detection Schemes and Noise

An overview of the main differences between direct and coherent detection schemes in ϕOTDR operation, as well as the main sources of noise involved and possible solutions for noise reduction is presented below.

3.2.3.1 Direct detection and noise in ϕOTDR operation

When the signal to detect is not critically low, as often happens if the sensing fibre is not very long, schemes using direct detection provide a simple and effective solution for ϕOTDR operation [32],[3]. Direct detection schemes present low complexity (the signal is detected directly in the time domain) and are also rather stable when compared to coherent detection schemes, where polarization and phase noises are much more an issue, often requiring averaging and post-processing denoising, as well as lasers of much higher coherence length [41]. The principle of operation and practical setup of a ϕOTDR using a direct detection scheme are as described in section 3.2.1.

There are several sources of noise which should be mentioned in ϕOTDR under normal operation (using direct detection), mainly: phase noise, laser frequency drift, polarization noise and finite extinction ratio (ER) of the ϕOTDR pulse. The phase noise can be understood as fluctuations in the values of $\Delta\varphi(t)$ (see eq. 3.3) and is essentially determined by the linewidth of the laser. In order to ensure low fluctuations of the relative phases $\Delta\varphi(t)$ of the reflected waves of the signal of interest (coming from a fibre section of length W/2), the coherence length of the laser should be longer than the pulse width. As an example, for a pulse width of ~50 ns (10 m in the fibre), a laser with linewidth of a ~few MHz is required [3]. Although a higher coherence of the laser will result in a decrease of the phase noise, it is not a straightforward deduction that the use of higher coherence lasers will improve the performance of ϕOTDR operation once above a coherence length equal to the pulse length. In fact, the use of extremely high coherence lasers may actually perform worse in a ϕOTDR system using direct detection, due to the increase of coherent noise, as discussed in section 3.3.2.2.

Since different laser frequencies will result in different ϕOTDR traces (different interference patterns) [27], the laser frequency drift, i.e., the variation of the central frequency ω over time, will result in a variation of the trace pattern over time, thus introducing noise in the measurement. For this reason, a ϕOTDR laser should not only have high coherence, but also high frequency stability over time. In theory, the laser frequency drift can also introduce phase noise in the measurement as the beginning and the end of the pulse will have different central frequencies. However, this effect should be very small, since it is proportional to the frequency drift over the time of the pulse width.

As for the polarization noise, it can be observed from eq. 3.3 that the amplitude of the interference terms will be dependent on the relative angle of polarization $\theta_p(t)$ of the interfering waves. If the polarizations of two interfering waves are aligned, maximum visibility will be achieved, while in the case when the polarizations are orthogonal, the interference terms are null and the visibility will be zero. The visibility of the ϕOTDR trace is therefore sensitive to changes in the relative polarization between interfering fields. Since in low birefringence fibres, such as SMF, the state of polarization (SOP) varies randomly along the fibre, the polarizations of the interfering waves may not be fully aligned, even if linear polarization is used at the input, and the visibility of the trace will decrease. Similarly to coherent detection schemes [27], scrambling the polarization can help to reduce the polarization noise in the ϕOTDR trace. Since the orthogonal polarizations of the backscattered waves do not interfere, it has been demonstrated that these can be split and monitored separately, thus obtaining two statistically independent channels with higher visibility, which improves the detection of intrusions using ϕOTDR [33, 39].

Lastly, a finite ER of the ϕOTDR pulse will result in a CW component between the pulses which will generate a CW backscattered noise that will be added to the signal. Since the power of the backscattered noise increases with the fibre length, it can be an important limitation, especially if very long fibres are used.

Using ϕOTDR with direct detection, vibration measurements of up to 40 kHz (limited by the flight time of pulses in the fibre) over 1.25 km, with a resolution of 5 m, were achieved. In this case, a semiconductor optical amplifier (SOA) was used to achieve high extinction ratios in the ϕOTDR pulses and therefore suppress coherent noise [3]. The simplicity of the scheme was maintained as no averaging, post-processing or extremely high coherence lasers (a semiconductor laser with a linewidth of 1.6 MHz was used) were required.

Further considerations on the noises and performance of ϕOTDR operation are discussed in section 3.3.2, where a theoretical model which includes the signal statistics of the ϕOTDR trace, before and after a perturbation, is presented.

3.2.3.2 Coherent detection

So far, the considerations regarding ϕOTDR operation assume a direct detection scheme. However, when detection of very weak signals is required, an interesting possibility is the use of coherent (also called heterodyne) detection which can potentially greatly increase the SNR.

The principle of coherent detection consists of mixing the optical signal with a local oscillator (LO)signal before reaching the photodetector [42] and was initially proposed in the context of the usage of ϕOTDR for distributed vibrations in [25], although its application in ϕOTDR for static measurements [27] had previously been reported as well. The practical setup of a ϕOTDR using coherent detection is shown in Fig. 3.6.

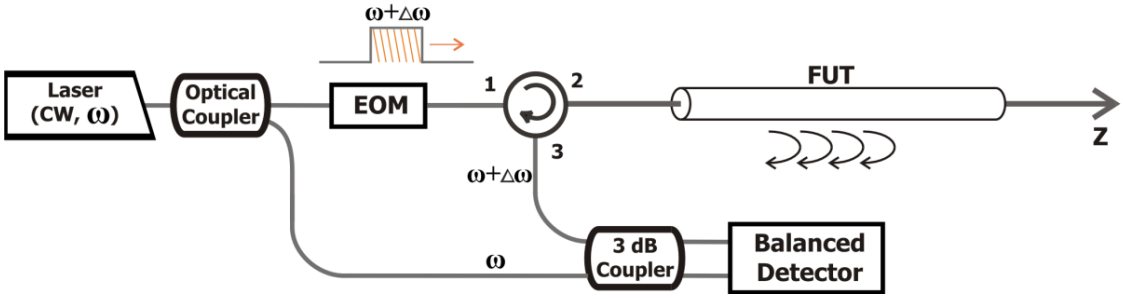

Fig. 3.6 Practical setup of a ϕOTDR using coherent detection.

The light coming from a high coherence CW laser source, with central frequency ω, is split by a coupler in two parts, one to be used as LO (E_{LO}) and the other to be used as the ϕOTDR pulse, which will generate the backscattered signal E_S. Before being launched into the sensing fibre, a frequency shift $\Delta\omega/2\pi$ (typically of a few hundred MHz [25],[38]) is applied to the ϕOTDR pulse using an electro-optical modulator (EOM). After the EOM, the ϕOTDR pulse is usually amplified before reaching the fibre. The backscattered signal (E_s) is then mixed (i.e., added) with the E_{LO} using a 3 dB coupler before reaching a balanced photodetector. In this case, the optical power $I(t)$ resulting from the interference of the LO signal (E_{LO}) with the backscattered signal (E_S) will be given by

$$I(t) \propto \left|\vec{E}_{LO}(t)e^{i\omega t} + \vec{E}_S(t)e^{i(\omega+\Delta\omega)t+\Delta\varphi(t)}\right|^2 = E_{LO}(t)^2 + E_S(t)^2 + 2E_{LO}E_S\cos\left(\theta_p(t)\right)\cos\left(\Delta\omega t + \Delta\varphi(t)\right), \quad (3.4)$$

where $\theta_p(t)$ and $\Delta\varphi(t)$ are the relative polarization angle and phase between the LO signal (E_{LO}) and the backscattered signal (E_S), respectively. Provided that the 180

degree phase shift between the two outputs of the 3 dB coupler is preserved, the use of balanced detection will eliminate the Direct Current (DC) and common mode components and improve the SNR by 3 dB [25]. The main differences between direct and heterodyne detection can be readily deduced from eq. 3.4.

The main advantage comes from the fact that the optical amplitude of the LO signal will be typically much higher than that of the backscattered signal ($|E_{LO}|>>|E_S|$). In this case, the intensity of the signal of interest ($\propto E_{LO}E_S$) will be higher than then intensity of the signal using direct detection ($\propto E_S^2$), even though there is no optical amplification. If the optical amplitude of the LO is made high enough, the SNR of heterodyne detection can be made shot noise limited [25] even for weak signals, while when using direct detection this can only be achieved with rather high signals powers. Therefore, coherent detection can provide a much higher sensitivity for detection of weak signals.

As for the disadvantages of coherent detection, apart from the problems which affect the quality of the backscattered signal (E_S), previously commented in the case of direct detection, these mainly derive from the requirement of coherently interfering the backscattered signal (E_S) and the LO signal (E_{LO}), which can be separated by as much as twice the fibre length. In this case, the relative phase noise and relative polarization between backscattered and the LO signals may lead to higher noise and instability when compared with the direct detection situation [42].

While in direct detection the required coherence length of the laser is of the order of the pulse width (~few MHz [3]), as interference occurs between waves separated by as much as that length, the required laser coherence length for coherent detection schemes will be much higher, the linewidth being typically of the order of a few kHz for a few kilometers of fibre [25],[41],[37],[35]. In long range (>100 km) operation, lasers with linewidth as low as 100 Hz have been used [43],[44], which can considerably increase the complexity and cost of the system. The drift of the laser central frequency will also introduce noise in the measurement.

The amplitude of the interference between E_{LO} and E_S strongly depends on their relative state of polarization and can even reach zero for the case of orthogonal polarizations. Coherent detection is therefore generally dependent on changes of the SOP along the optical paths of E_{LO} and E_S before these are mixed, and the setup is therefore very

sensitive to SOP changes. While scrambling the polarization can help to reduce the polarization noise in the ϕOTDR trace [27], another solution is to maintain the SOP constant along the sensing fibre: by using PMF, as well as polarization maintaining components, the SOP variations are eliminated, thus increasing the stability and performance of the system [26]. However, PMFs are expensive and, more importantly, present high losses, which severely limit the sensing range when compared to the use of SMF.

Using ϕOTDR with coherent detection, the detection of vibrations of up to 1 kHz has been demonstrated with 5 m of spatial resolution over 5 km of SMF [25]. Later, using PMF, of up to 2.25 kHz with a spatial resolution of 1 m over 200 m [26]. In this case, the detection bandwidth was limited due to the use of (moving) averaging of the traces, but also by the limited pulse repetition rate of the system (10 kHz). By using suitable post-processing denoising methods, these features were later improved to 8 kHz with 0.5 m spatial resolution over 1 km of SMF [41].

3.2.4 Post-processing

Similarly to other distributed fibre sensors, the backscattered signal to be analyzed in ϕOTDR operation is rather low and has to be carefully handled. Using direct detection, the use of optical amplification before detection can increase the SNR [39], but this may not be sufficient, depending on the application. As for coherent detection schemes, although the signal of interest has a higher power, the noise sources previously discussed will cause fluctuations in the ϕOTDR trace which can mask the phase modulation induced by a perturbation. In these cases, the use of post-processing denoising methods may be a solution and, in general, proper data treatment for specific applications can increase the performance of the sensors.

Averaging the ϕOTDR (by N) traces can reduce the signal fluctuations (by $\sqrt{N}$) and increase the SNR, but this will also result in a decrease of the detection bandwidth (by N). Although the use of moving averages can reduce this effect [25], the method essentially still removes high frequencies and retains low frequencies, and therefore a reduction of the detection bandwidth still occurs.

Other methods have been proposed aiming to reduce the noise in the signal without reducing the bandwidth of detection. Among these, wavelet denoising methods have

been used to assist ϕOTDR operation in several schemes [41],[40],[38]. The principle of the method is described in [41] and consists of decomposing the signal into a series of base functions of dilated and translated versions of the mother wavelet function. Using the wavelet transform (which can be continuous [40] or discrete[41]), wavelet coefficients are calculated and those considered to correspond to noise are removed. The signal is then reconstructed without the noise coefficients.

A very important feature for practical applications is then to identify what kind of event corresponds to a certain disturbance pattern. In this context, specific intruder signature analysis has been reported to distinguish the patterns of a person walking from a car [45].

3.2.5 Range increase

To achieve reliable vibration measurements, it is indispensable to achieve good visibility and high SNR in the measured trace. In addition, it is generally desired to have the best possible range and resolution. The visibility of the trace will remain high if the coherence of the ϕOTDR pulse is high (in comparison with its width) and remains so all along the fibre. As for the range, resolution and SNR, it should be established that these are tightly related parameters. For a given resolution (ϕOTDR pulse width), an increase in the dynamic range and SNR of a ϕOTDR sensor can be achieved by increasing the ϕOTDR pulse peak power. However, the ϕOTDR pulse peak power cannot be indefinitely increased due to the onset of nonlinear effects, mainly modulation instability (MI) [2]. Although specific signal post-processing can improve the performance of a ϕOTDR [41], as presented in the previous section (3.2.4) , a significant increase in the sensing range can only be achieved using optical amplification [46]. In particular, distributed Raman amplification seems an ideal route to achieve this range enhancement, as the amplification can be engineered to keep the power of the optical pulse almost constant along the whole fibre length [5],[38]. Unfortunately, the use of Raman amplification also presents drawbacks, mainly due to relative intensity noise (RIN) transfer from the Raman pumps [47]. Recently, the use of Brillouin amplification has also been proposed to extend the sensing range in ϕOTDR operation [43], although in this case several practical drawbacks also arise: several fibres with different Brillouin frequency shifts (which had to be precisely controlled) were required to tune the gain along the setup and the gain is also

temperature-dependent, which can lead to instability of the system. An overview of the main problems and solutions for increasing the sensing range in ϕOTDR operation is presented in this section.

3.2.5.1 ϕOTDR Peak power limitations due to nonlinearities

When the ϕOTDR pulse peak power is increased above a certain level, the increase of nonlinearities will degrade the performance of the system. The limitations imposed by some of these nonlinear effects have been briefly described in the general context of coherent OTDRs [48]. Among these nonlinear limitations, the first effect to arise in the usual conditions for ϕOTDR operation is MI [2].

MI in fibres results from the interplay of Kerr effect and anomalous dispersion, and, in the time domain, results in the breakup of a CW beam into a train of ultra-short pulses. In the spectral domain, MI manifests itself as the build-up of two sidebands at each side of the centre beam wavelength, as shown in section 2.3.2.1. MI was demonstrated to occur in optical fibres a long time ago [15], and its effects have been theoretically and experimentally described [9, 49], including in-depth descriptions of its spectral dependence [50]. In the strong conversion regime (i.e., when the sidebands grow up to powers comparable to the main line), the MI process exhibits a reversible power exchange between the main laser line and the sidebands known as the Fermi-Pasta-Ulam (FPU) recurrence [51]. In the specific context of distributed fibre sensors, MI has been shown to limit the performance of distributed fibre sensors based on stimulated Brillouin scattering (SBS) [16]. In the specific case of ϕOTDR, ref. [48] provided useful limits to avoid the effect of MI in the general case of coherent OTDRs. However, in this study, there was no description of the effect of MI on the trace.

An in-depth experimental and theoretical description of the impact of MI in the performance of a ϕOTDR is presented in section 3.4.

In some cases, MI may not be the main limitation to the ϕOTDR peak power (e.g., in fibres with normal dispersion at the operating wavelength). In this case, depending on the specific settings, the peak power may be limited by Brillouin or Raman effects. For SRS, the threshold Raman pump power (P_R^{th}) will be given by $P_R^{th} = 16\frac{A_{\text{eff}}}{g_R \cdot z_{\text{eff}}}$ (eq. 2.36), where A_{eff} is the effective mode area, g_R is the Raman gain coefficient and z_{eff} is the effective fibre length. As for the SBS effect, the threshold Brillouin pump power

(P_B^{th}) can be demonstrated [9] to be $P_B^{th} = 21\frac{A_{\text{eff}}}{g_B \cdot L_p}$, where g_B is the Brillouin gain coefficient and L_P is the pulse length (it is assumed that the pulse width is much longer than the phonon lifetime, which is usually the case in conventional settings). As it can be seen, for the Brillouin case, the relevant length to evaluate the threshold is reduced to the length of the pulse, as the scattered wave is counter-propagating with the pulse. Since g_R is ~10^3 times lower than g_B, the thresholds for the Brillouin and Raman effects will be similar when the length of the pulse is ~10^3 times lower than z_{eff}. For a long fibre (z_{eff}≈20 km), this occurs for a pulse width of 20 m. If the $\frac{g_B \cdot L_p}{g_R \cdot z_{\text{eff}}}$ is higher/lower than ~1, then the Brillouin/Raman will be the main limiting effect, respectively.

3.2.5.2 Raman Amplification

Raman amplification has been used for more than two decades to increase the performance of optical communication systems [52-54], and since then, it has been widely described theoretically and experimentally in the literature, for a number of long-distance applications [22, 23, 47, 55-60]. In optical sensing, a number of different architectures using Raman amplification have been proposed to assist distributed [23, 56, 57],[5],[38] and point [58] fibre sensors. Different pumping configurations have been studied using first [38],[5, 56],[23], second [22, 57],[61] and even third-order [59] Raman amplification. The noise introduced by the Raman gain process, mainly due to RIN transfer from the Raman pumps, is one of the main concerns when using this type of amplification [5, 47, 60, 62]. If not carefully handled, this can completely mask the signal.

In ϕOTDR operation, Raman amplification can be used to maintain the ϕOTDR pulse power high along the whole fibre length, thus extending the sensing range. Using direct detection, encouraging efforts were initially reported describing the use of first-order Raman amplification to assist ϕOTDR for intrusion sensing over distances of up to 62 km [63] and 74 km [46] with spatial resolutions of 100 m and 20 m respectively. In these cases, however, the performance as a vibration sensor was not clearly established, as no vibration measurement was performed, and no in-depth study of signal noise was developed. In ref. [63], averaging of 50 traces was required, which greatly reduces the detection bandwidth of the system. Recently, the use of first-order Raman amplification and balanced detection to reduce the RIN transfer from the Raman pumps was reported

[5], achieving distributed vibration measurements of up to 390/250 Hz over 100/125 km with a spatial resolution of 10 m. Theoretical simulations of the pulse power evolution and system noise evaluation were also included. The use of second-order Raman amplification has also been described, and a performance improvement over first-order Raman amplification under similar measurement conditions was reported: distributed vibrations measurements of up to 380 Hz over 125 km, with a spatial resolution of 10 m and higher SNR were achieved [61].

The use of Raman amplification to assist ϕOTDR for distributed intrusion and vibration sensing using coherent detection has also been described in [38], showing an improvement of SNR versus direct detection [5] over a similar range. Frequencies of up to 375 Hz (limited by the flight time of pulses in the fibre) over 125 km, with a spatial resolution of 8 m and higher SNR (up to 21.5 dB for intrusion sensing), were achieved. In this case, however, the complexity of the scheme was increased due to the use of coherent detection (previously discussed in section 3.2.3.2), which required a laser with a linewidth three orders of magnitude lower than in ref. [5]. The detection of events for intrusion sensing was also demonstrated, although in this case post-processing denoising was used as well as averaging of 32 traces, which limited the detection bandwidth to frequencies below 5 Hz.

The experimental and theoretical description of the advantages and limitations of using ϕOTDR assisted by first- and second-order Raman amplification, including simulations of the ϕOTDR pulse power evolution and noise dependency on several factors, such as RIN transfer, are presented in sections 3.5 and 3.6.

3.2.5.3 Brillouin Amplification

The use of Brillouin amplification to assist ϕOTDR operation has been recently proposed as an alternative to the use of Raman amplification. Since SBS presents a higher gain coefficient than stimulated Raman scattering (SRS), lower pump powers are required for signal amplification [43]. Since the Brillouin gain is dependent on the frequency difference between the signal and the pump, the gain can be tuned along the sensing fibre with a proper choice of fibres with different Brillouin frequency shifts. This, however, also constitutes a drawback of the technique, as the gain will also be dependent on the temperature of the fibre, which can lead to instability of the system. Using ϕOTDR assisted by Brillouin amplification, intrusion sensing was demonstrated

over 124 km [43]. In this case, a coherent detection scheme with an ultra-narrow linewidth (100 Hz) laser, and wavelet denoising, were used. By combining first and second-order Raman amplification with Brillouin amplification the sensing range was improved to 175 km [44].

3.2.6 Bandwidth increase

In conventional ϕOTDR operation, only one pulse can travel in the fibre at a time in order to avoid the superposition of backscattered signals. Therefore, the maximum pulse repetition rate is limited by the sensing fibre length (eq. 3.2). In order to increase the pulse repetition rate above this limit, a technique has been recently proposed. By using coherent detection, it is possible to distinguish between superimposed traces resulting from ϕOTDR pulses with different frequencies. In this case, ϕOTDR pulses separated by a time delay lower than the time interval corresponding to the fibre length can be used, thus increasing the sampling rate [64],[65]. By using two and four ϕOTDR pulses of different frequencies, the maximum sampling rate was increased by two times [64] (2·80 kHz over 1 km of fibre) and four times (4·10 kHz over 10 km of fibre) [65], respectively, when compared to that of a conventional ϕOTDR limited by the fibre length. However, it should be pointed out that the possibility of noise increase in the system, due to the detection of superimposed traces, was not properly analyzed. Therefore a straightforward deduction that the true frequency detection bandwidth of these systems will be increased by a factor of two and four is incorrect. The complexity of the demodulation process is also increased, thus requiring more processing power, which can present a limitation in real practical applications.

Another solution has been proposed to greatly increase the frequency detection bandwidth, which consists of combining a Mach-Zehnder interferometer (MZI) and a ϕOTDR [66],[67]. In the same fibre, CW light is used for the MZI measurements, which allows the detection of frequency vibrations in the MHz range. Narrow pulses (~10 m) were used for the ϕOTDR operation, which allows the localization of the vibration events. The technique allowed the detection of distributed frequency vibrations of up to 6 MHz of a pencil break event over ~1 km of fibre with 5 m of spatial resolution.

3.2.7 ϕOTDR for dynamic sensing: Performance overview

The historical evolution and respectibe performance data of the reported ϕOTDR sensors used for dynamic sensing (mainly intrusion and vibration detection) is presented in Table 3.1, which allows some intercomparison of the results.

Table 3.1 Evolution and performance data of ϕOTDR used for dynamic sensing

Date	REF	Sensing Range	Spatial Resolution	Detection Bandwidth	Laser linewidth	Detection Scheme	Optical Amplification
Mar-93	[28]	Intrusion Sensing Apparatus described					
Aug-98	[34]	~10 km	~10 m	Intrusion	YAG laser	Direct	-
Sep-98	[30][1]	6 km	400 m	30.5 Hz	<50 kHz	Direct	-
Jun-05	[32]	12 km	1 km	Intrusion	<3 kHz;	Direct	-
Dec-05	[39]	12 km	200 m	Intrusion	<3 kHz;	Direct	-
Apr-07	[33]	19 km	200 m	Intrusion	<3 kHz;	Direct	-
Apr-08	[68][1]	14 km	50 m	Intrusion	20 kHz	Direct	-
Oct-09	[63][1]	62 km	100 m	Intrusion	<3 kHz;	Direct	1st Raman
Nov-10	[25]	1.2 km	5 m	1 kHz	20 kHz	Coherent	-
Aug-11	[26]	~200 m (PMF)	1 m	2.25 kHz	20 kHz	Coherent	-
Nov-11	[37][1]	3 km	5 m	200 Hz	2 kHz	Coherent	-
Apr-12	[41]	1 km	0.5 m	8 kHz	4 kHz	Coherent	-
Aug-12	[40]	200 m tested; (estimated: up to 10 km)	0.2 m	Freq. Sweep between 500-1000 Hz (nonstacionary)	535 kHz	Coherent	-
Jan-13	[67] (3)	1 km	5 m (3)	3 MHz (3)	<50 kHz	Coherent	-
Feb-13	[46] (2)	74 km	20 m	Intrusion	2 kHz (?)(2)	Direct	1st Raman
Jul-13	[69]	<1 km	2 m	500-5000 Hz	Distributed-Feedback (DFB) laser	Direct	-
Sep-13	[36]	1 km	3 m	Intrusion	<50 kHz	Direct	-
Oct-13	[66] (3)	1.15 km	5 m (3)	6.3 MHz (3)	<50 kHz	Coherent	-
Dec-13	[3]	1.25 km	5 m	40 kHz	1.6 MHz	Direct	-
Apr-14	[5]	100/125 km	10 m	390/250 Hz	1.6 MHz	Direct	1st Raman
May-14	[38]	131.5 km	8 m	375 Hz	3 kHz	Coherent	1st Raman
Jun-14	[43] (1)	124 km	40 m	Intrusion	100 Hz	Coherent	Brillouin
Jun-14	[44] (1)	175 km	25 m	Intrusion	100 Hz	Coherent	1st+2nd Raman +Brillouin
Jun-14	[61] (1)	125 km	10 m	250 Hz	1.6 MHz	Direct	1st Raman
		125 km	10 m	380 Hz	1.6 MHz	Direct	2nd Raman
Jun-14	[65] (1, 4)	10 km	20 m	Sampling: 4·10 kHz (4)	Not specified	Coherent	-
		1.1 km	10 m	Sampling: 2·80 kHz (4)	<50 kHz	Coherent	-
Jun-14	[64] (1, 4)						

[1]Conference Proceedings
[2]Article written in Chinese
[3]MZI and ϕOTDR combined: MZI used for MHz frequency detection and ϕOTDR used to locate event
[4]More than one ϕOTDR pulse (with different frequencies) in the sensing fibre at a time

3.2.8 Comparison with other DFOS

In order to provide a comparison between the characteristics and performances of ϕOTDR and other distributed fibre optic sensors (DFOS), an overview of the features of the different existing DFOS is presented in this section.

Using a single interrogation unit, DFOS can currently provide up to hundreds of thousand or even million [70] resolved sensing points along an optical fibre distance which can range from a few metres [71] to hundreds of kilometers [72]. Such features cannot be matched by any other technology. Furthermore, the fibre is used as both the sensing element and the communication channel which, allied to the small size, geometric versatility and lightweight of fibres, renders DFOS a high potential to be used as the "nerve system" of modern structures, by mapping different parameters in real time. The 1D monitoring of vibrations over >100 km, which can be used for intrusion detection along gas pipelines [5], the 2D surface temperature mapping, for environmental purposes, of a coal waste pile in combustion [73] or the 3D internal strain measurement of a large building to assess its structural integrity [74], these are a few of the possibilities which DFOS can be used for.

DFOS can be classified according to the type of scattering they rely on, mainly Raman [20], Brillouin [75] and Rayleigh [76] scattering. The measurements of the signal can also be performed in the time or frequency domain. Comparisons between the characteristics of the different DFOS can be found in the literature [77],[74],[78]. Due to different underlying physical working principles, these sensors present trade-offs in their performance characteristics, and are therefore best suited for different applications. A short description of DFOS techniques is presented below in order to provide a comparison with ϕOTDR sensors.

3.2.8.1 Rayleigh based distributed sensing

Historically, Rayleigh based OTDR (commonly referred simply as "OTDR") was the first DFOS technique to be demonstrated, almost four decades ago [76, 79], and is still commonly used for distributed measurement of losses along the fibre (thus allowing the measurement of fibre attenuation and the location of broken points, optical connectors, micro-bending or discontinuities), providing typical spatial resolutions of sub-meter/hundreds of metres over a few kilometers/hundreds of kilometers. OTDR works

by sending light pulses into an optical fibre and monitoring the Rayleigh backscattered light in the time domain, at the same fibre end. OTDR uses low coherence (broadband) light and can, therefore, only measure intensity variations along an optical fibre. But other parameters can be measured by implementing suitable transducing mechanisms which can convert the quantity to be measured into intensity variations of the light propagating in the fibre. The use of heterodyne detection (also called coherent detection), which consists of combining the optical signal coherently with a LO signal before reaching the photodetector, has been demonstrated to allow a performance improvement when compared with direct detection OTDR [80], but can also lead to amplitude fluctuations in the coherent OTDR trace introduced by the fading noise resulting from the interference between the signal and the LO signal [42, 81].

A few years after the OTDR implementation, POTDR, which works similarly to OTDR but using polarized light, was introduced [82]. POTDR attracted a considerable amount of attention due to the possibility of performing nondestructive distributed measurements of birefringence (inversely proportional to the polarization beat length) [83] and coupling length, which allowed the measurement of the PMD [84-87] and polarization dependent loss (PDL) [87]. Later, POTDR was also proposed for intrusion sensing, based on the high sensitivity to external perturbations of the SOP [88-90]. A preliminary work showed the possibility of intrusion detection over more than 100 km using POTDR assisted by second-order Raman amplification [88]. The main limitation of the technique is that, due to the nature of the SOP, when an event occurs in a point of the fibre, it affects the entire trace after that point. POTDR can therefore detect the starting point of a perturbation very precisely, but not its end [89]. Nevertheless, the detection of pure vibration frequencies of up to 5 kHz over 1 km, with 10 m of spatial resolution in multiple points, has been demonstrated [90].

In the time domain, the backscattered signal is associated with a position of the fibre based on the time between the sent pulse and the detection of the backscattered signal. In this case, the spatial resolution is ultimately limited by the pulse width in the optical domain and the bandwidth of the photodetector/digitizer in the electric domain. For high spatial resolution, these systems become very expensive and complicated due to the low SNR of the received signal and the high bandwidth required. An alternative solution to perform high spatial resolution measurements is optical frequency domain reflectometry (OFDR). In this case, a tuneable laser frequency is continuously swept and reflections

from the fibre under test (FUT) interfere at the detector with a fixed reflection, the LO signal. After performing a Fourier transform, the amplitude of each frequency has information corresponding to power reflected at a given fibre position [91]. OFDR presents a spatial resolution inversely proportional to the tuneable frequency range of the laser [91, 92]. As for the sensing range, it is limited, among other factors, by the laser coherence length [91], being typically of up to a few tens to hundreds of metres. Using a laser with a typical tuning range of up to 40 nm, a spatial resolution of 22 μm over 35 m has been reported [71].

3.2.8.2 Raman based distributed sensing

Raman based distributed temperature sensing (DTS) relies on the principle that the temperature can be determined from the ratio of measured Stokes and anti-Stokes Raman scatterings. This principle is owed to the fact that the intensity of the Stokes and anti-Stokes Raman scatterings depends on the populations of the initial states of the material of the fibre, which in turn depend on the temperature. The technique was initially demonstrated by Dakin et al. [20], and commercial Raman based DTSs were made available in the 90's, before Brillouin based ones [93]. Although less commonly used, temperature can also be determined from the ratio of the anti-Stokes to the Rayleigh backscattered light intensities.

The weak anti-Stokes Raman signal, which is 20-30 dB lower than the Rayleigh scattered light, presents one of the main challenges to the use of Raman based DTS. To overcome this problem, high power lasers and long signal averaging times are typically required. Early works used multimode fibres (MMF) to enhance the sensitivity [94], but this limited the sensing range due to the high losses of such fibres.

Using Raman OTDR, different spatial/temperature resolutions and sensing ranges have been demonstrated, ranging from 0.01 m/3ºC over a 3 m of fibre with 60 s integration time (using single photon-counting techniques) [95], to 17 m/5ºC over 40 km [96] (using a 255 bit Simplex coding and discrete Raman amplification). Currently available commercial systems provide spatial resolutions of 5 m over 30 km with measurement time of a few minutes [78]. Raman OTDR has also been combined with Brillouin frequency-based sensing to perform temperature compensated strain measurements, achieving a spatial/strain/temperature resolution of 0.24 m/97 με/2.5ºC over 135 m [97].

3.2.8.3 Brillouin based distributed sensing

In the Brillouin scattering process, an electromagnetic wave is scattered by an acoustic wave. The Brillouin frequency shift between the incident and the scattered wave is dependent on the strain and on temperature applied to a fibre, and can therefore be used to measure these quantities. The possibility of strain measurement as well as the longer sensing ranges achievable as compared to Raman based DTS [93], led to intensive research on Brillouin based distributed sensing in the last two decades, and a number of configurations based on this principle have been reported. In the time domain, Brillouin optical time domain reflectometry (BOTDR) makes use of spontaneous Brillouin scattering, requiring only access to one end of the fibre [98], while Brillouin optical time domain analysis (BOTDA) [99] makes use of SBS, thus achieving higher SNR, but requiring access to both ends of the fibre. Recently, a spatial/temperature/strain resolution of 5 m/1.9ºC/38 με over a 240 km fibre loop (120 km sensing range) was demonstrated using first and second-order Raman-assisted pulse-coded BOTDA [100]. A BOTDA can operate in two different configurations: Brillouin gain [101] and Brillouin loss [102].

The phonon lifetime in a silica fibre (~6 ns) sets a "natural" resolution of ~1 m for standard BOTDA. In order to overcome this limitation and further increase the resolution, a number of techniques have been recently proposed, such as dark pulse [103], dynamic grating [104], differential pre-excitation [105], Brillouin echoes [106] or Differential Pulse-Width pair (DPP) [107], [72]. Among these, DPP-BOTDA presents the best features for long range sensing, and spatial/temperature resolutions ranging from 0.02 m/2ºC over 2 km [107] to 0.5 m/2.9ºC over 100 km [72] (assisted by Raman amplification) have been demonstrated.

An important feature of the Brillouin based sensing is that it has been already demonstrated to provide absolute measurements of temperature and strain unlike temperature measurement using ϕOTDR, which requires a comparison between two fibre measurements. The long-term stability of the ϕOTDR "fingerprint" of a given optical fibre remains an unsolved question, which has to be seriously addressed. A limitation of Brillouin-based sensors in general is that the Brillouin scattering signal (for spontaneous scattering) is generally lower than the Rayleigh scattering one and therefore averaging of traces is usually required to increase the SNR. This limits the maximum readable frequency in dynamic measurements. In fact, for sensing distances

of a few kilometers, Brillouin sensors are typically limited to a few tens of Hz, which is far from the tens of kHz demonstrated using ϕOTDR [3].

3.3 ϕOTDR for distributed vibration sensing

3.3.1 Introduction

In this section, the performance of a ϕOTDR used for distributed vibration sensing, using a direct detection scheme, is characterized both theoretically and experimentally, using the best measuring conditions which avoid nonlinearities (discussed in section 3.4). An analysis of the statistics and noise of the ϕOTDR signal is also presented. Distributed measurement of ultrasonic vibrations is achieved, to the best of our knowledge, for the first time.

3.3.2 Theoretical Model

3.3.2.1 Signal statistics

We start by developing a theoretical model for a ϕOTDR, which will allow us to understand the performance of the experimental system described later on. For the theoretical model, we assume that a short spatial width (W) ϕOTDR pulse of highly coherent light is delivered into a fibre with constant loss (α) and isotropic propagation. This pulse reaches the position z in the fibre at time T. The ϕOTDR signal received from the pulse at that position (at instant $2T$) will be the sum of the fields reflected from the M scattering points contained in the section of fibre $z \in [T \cdot V_g - W/2; T \cdot V_g]$ (as deducted in section 3.2.1), and will be

$$E(t = 2T, z = 0) = E_0 e^{-2\alpha \bar{z}} e^{i\omega 2T} \sum_{m=1}^{M} r_m e^{i\phi_m} \quad , \tag{3.5}$$

where V_g is the group velocity and $\bar{z} = [T \cdot V_g - W/4]$ is the position corresponding to the centre of the fibre section from which the signal is being collected. It should be noted that the signal received $E(t=2T, z=0)$ accounts for the contributions generated by the passage of the whole pulse (from leading to trailing edge), despite being the sum of the fields reflected from a fibre section of length $W/2$, as discussed in section 3.2.1. The m^{th} scattering centre has a reflectivity $r_m \in [0,1]$ (usually $r_m << 1$), and the phase introduced in the reflected field by both the optical path and the scattering centres is ϕ_m (where $\phi_m \in [0, 2\pi]$ is assumed to be uniformly distributed). The amplitude of the reflected field will follow a Rayleigh distribution, as shown in previous papers [81]. The

normalized intensity (I) received at the beginning of the fibre (z=0), neglecting the losses, will therefore be [108]

$$I = |E|^2 = \left|\sum_{m=1}^{M} r_m e^{i\phi_m}\right|^2 = \sum_{m=1}^{M} r_m^2 + 2\sum_{i=1}^{M-1}\sum_{j=i+1}^{M} r_i r_j \cos(\phi_i - \phi_j). \quad (3.6)$$

This addition of M ($M \to \infty$; $\sum_{m=1}^{M} |r_m| << 1$) wave amplitudes is a random walk process, and its probability distribution will follow an exponential distribution [108]:

$$P(I_M) = \frac{1}{M} e^{\left(-\frac{I_M}{M}\right)}. \quad (3.7)$$

It is interesting to note that the average intensity of the detected field from a given position will be proportional to the number of scattering centres M ($< I_M >= \int_0^{+\infty} I_M P(I_M) dI_M = M$) within the pulse length at that position.

It can be seen that there is a certain probability of having a close-to-zero signal at a given position (a signal below the noise level of the detector, δ). This probability is termed "fading probability", since the system "loses" completely the signal at this position. The fading probability ($P(I_M<\delta)$), as a function of the detector noise level δ, will be the cumulative probability of the intensity distribution function.

If a perturbation is introduced in the q^{th} ($q \in [1, M]$) scattering centre with a corresponding phase perturbation φ_p, then the corresponding intensity variation (I_Δ) between the unperturbed (I) and the perturbed (I') signals will be given by

$$I_\Delta = I - I' = 2\sum_{i=1}^{q-1}\sum_{j=q}^{M} r_i r_j [\cos(\phi_i - \phi_j) - \cos(\phi_i - \phi_j - \varphi_p)]. \quad (3.8)$$

It is clear that the response of the system is generally nonlinear, except for very small values of the perturbation φ_p. The perturbed and unperturbed signals have correlated exponential probability distributions. Thus, the probability distribution of the intensity variation will be Laplace-distributed [108, 109] (a different form of exponential distribution). In the case of an applied vibration, a ϕOTDR should therefore provide better information regarding the form (frequency) of the perturbation rather than from its amplitude. Again, the signal variation is proportional to M and the ϕOTDR signal intensity. A higher average back-reflected intensity (I) will result in higher values of I_Δ, increasing the sensitivity of the system and decreasing the fading probability of the

signal of interest (I_Δ). The most obvious solution to reduce the fading probability is then to raise the ϕOTDR pulse power. However, this approach is limited by the onset of optical nonlinearities [2], as discussed in section 3.4.

3.3.2.2 Signal-to-noise ratio (SNR)

As previously, the minimum detectable signal will be limited by noise in the optical detection. Two types of noise sources are present in a ϕOTDR system: electrical noise caused by the photodetection process (including shot noise and thermal noise), and optical noise which causes fluctuations in the input power to the detector (introduced by optical amplifiers, and coherent noise due to leakage of the pulse generation system). Considering high performance photodetectors, like the ones available commercially in fibre-optic instrumentation, the noise contributions introduced by the photodetection process are close to the fundamental minimum. Considering typical values of the parameters (pulse peak power on the order of hundreds of milliwatts, pulse length of a few metres, Rayleigh backscatter coefficient ($\alpha_{Rayleigh\ Backscatter}$) of -72 dB/m), the SNR given by pure detection processes in a 100 MHz detector is of the order of 20 dB, using the traditional formula for a p-i-n receiver [110]. Optical noise is generally much more a problem, as we will see next.

For a ϕOTDR system like the one described in section 3.3.3, we can consider two main sources of optical noise: signal-spontaneous and spontaneous-spontaneous beating caused by the backscattered amplified spontaneous emission (ASE) from the optical amplifiers and the non-infinite ER of the pulse generator. Fig. 3.7 presents the power distribution along the fibre for a ϕOTDR pulse with finite ER. Intra-band noise is generated due to the fact that there is optical power, at the ϕOTDR pulse frequency, outside the ϕOTDR pulse. The ratio between the peak power of ϕOTDR pulse (P_1) and the leaked power at the master frequency (P_2) is the *ER* of the pulse generator used ($ER=P_1/P_2$). Considering an incoherent type of noise, then:

$$\text{Incoherent Intra-band noise:} \qquad SNR \propto ER(L_{pulse} / L_{fiber}), \tag{3.9}$$

where L_{fibre} and L_{pulse} are, respectively, the lengths of the fibre and of the pulse in the fibre. However, if the coherence length of the master laser is much longer than the pulse length, and spreads over the complete extension of the fibre (which is the case in most typical high-visibility ϕOTDRs reported in the literature), then the backscattered *CW*

component will be interfering coherently with the backscattered pulse. In this case, the detected power will have terms proportional to the ϕOTDR pulse power ($[\alpha_{Rayleigh\ Backscatter}]P_1L_{pulse}$) (signal), the background ($[\alpha_{Rayleigh\ Backscatter}]P_2L_{fibre}$) (background noise) and the interference of the two ($\alpha_{Rayleigh\ \text{Backscatter}}\sqrt{P_1L_{pulse}P_2L_{fiber}}$) (coherent noise). Considering typical parameter values ($P_1L_{pulse}>>P_2L_{fibre}$), the SNR will therefore be:

Coherent Intra-band noise: $$SNR \propto \sqrt{ER(L_{pulse}/L_{fiber})} \tag{3.10}$$

For typical values, 10 km range and 10 m pulse length, it is required an ER of 50 dB to achieve a SNR of the order of 10 dB. This is not easily attainable with conventional pulsing methods, such as using an electro-optic modulator (EOM). A high ER is therefore essential for reliable measurements. It is interesting to notice that an extremely high coherence laser will actually perform worse in a conventional system, as there is no significant improvement in the signal once the pulse coherence is higher than its length, but there will be an increase in the length over which coherence noise is introduced.

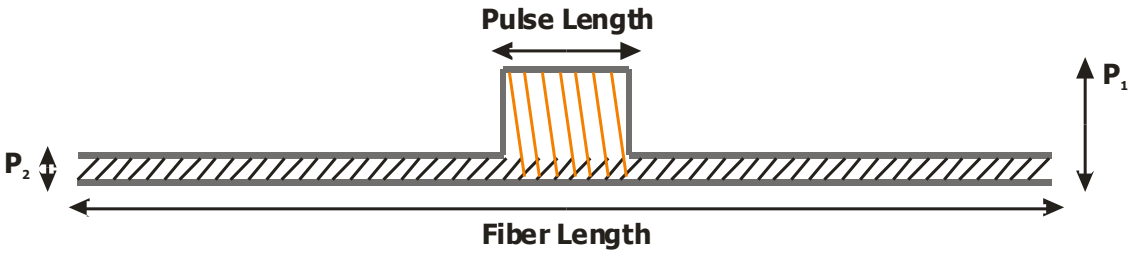

Fig. 3.7 Power distribution along the fibre for a ϕOTDR pulse with finite ER.

3.3.3 Experimental Work

3.3.3.1 Setup

The experimental setup used to characterize the performance of a ϕOTDR, when employed for distributed vibration measurements, is shown in Fig. 3.8. A laser diode (LD), with a linewidth of 1.6 MHz and emitting at 1546 nm, was used as the laser source. This LD presents a high enough coherence for the experiment (LD coherence length ≈50 m while the pulse length in the fibre is ≈10 m), but not too high, thus minimizing the generation of coherent noise between pulses (as discussed in section 3.3.2) while maintaining the simplicity of the scheme (the LD is driven by a standard current and temperature controller), and not presenting the technological challenges

typically associated with lasers with sub-MHz linewidths. An optical isolator (ISO) was placed at the laser output to avoid disturbances in the laser coherence due to back-reflections. A SOA, with rise/fall times on the order 2.5 ns, driven by a waveform signal generator (SG), was used to create 50 ns almost square pulses. A polarization controller (PC) was placed before the SOA to optimize the modulation properties and avoid any polarization sensitivity problem. Between the signal pulses, the SOA was negatively biased so as to enhance the ER of the delivered pulses. An ER above 50 dB was achieved this way. In this configuration, the ER has a very high impact on the SNR of the detected trace. An Erbium-Doped fibre Amplifier (EDFA) was used to boost the power of the ϕOTDR pulses and reach pulse peak powers of several hundred milliwatts. In order to minimize the effect of ASE added by the EDFA, we inserted a tuneable fibre Bragg grating (FBG) working in reflection. The spectral profile is the typical spectrum of a 100 % reflection FBG, and its spectral width is 0.8 nm. For the used settings, the leaked ASE power is below the leaked power of the master signal, and therefore the ER decrease is not significant after the EDFA+FBG [111]. Before being coupled into 9.9 km of SMF-28 fibre (FUT), light passed through an attenuator, which allowed varying the input ϕOTDR pulse power in the fibre. The average optical input power was measured at this position using a calibrated tap coupler (not shown in the figure), and the signal back-reflected from the fibre was recorded with a 125 MHz p-i-n photodetector and a high-speed digitizer. Since the ϕOTDR traces exhibit high-contrast rapid oscillations, the detector bandwidth should ideally be much larger than the pulse spectral bandwidth. In our case, the detector has a bandwidth (125 MHz) roughly six times higher than the pulse spectral bandwidth which is enough to adequately represent the process. The ϕOTDR pulse power was adjusted to achieve the best performance and

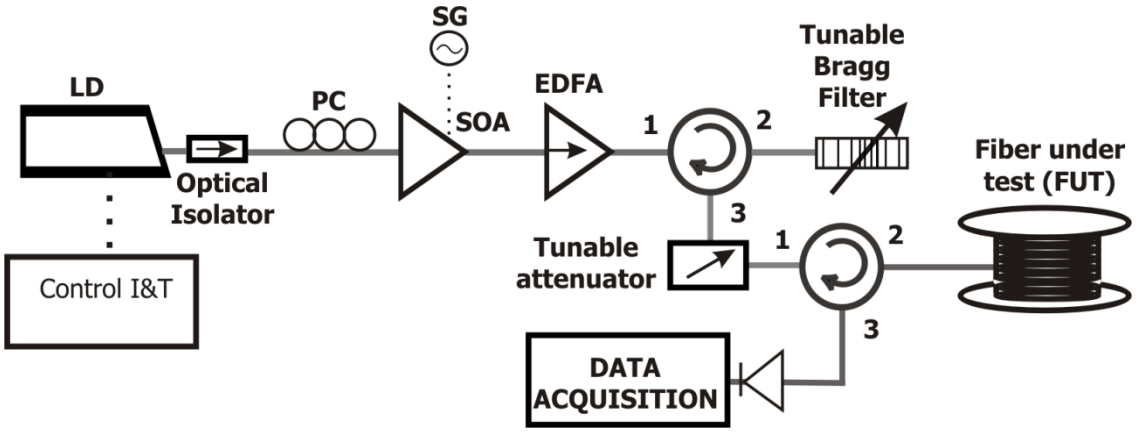

Fig. 3.8 Experimental setup of the ϕOTDR used for distributed vibration sensing.

avoid nonlinear effects (discussed in section 3.4) [2]. For visibility characterization, a 9.9 km fibre was used. We chose a long fibre in order to reliably ensure that the visibility conditions are kept in the final setup used for the vibration measurements, where a 600 m fibre was used.

In this experiment, the use of a SOA is very important due to the noise suppression between pulses which results in a much lower intra-band noise. Furthermore, due to spectral hole burning in the active material, the SOA enhances the spectral purity of the laser spectrum in the active state, as narrowband amplification of the central laser line occurs [112]. To evidence the impact of the SOA on the coherence of the launched spectrum, the laser was biased with a noisy current, leading to some spectral broadening of the central laser line. The spectrum of the laser was observed with an optical spectrum analyzer (OSA) before and after passing the SOA (Fig. 3.9). The effect of the SOA is clearly visible, as the spectrum after the SOA presents a much narrower linewidth (in fact limited by the 0.02 nm resolution of the OSA). For the conventional settings, the SOA helps to reduce noise introduced by the side modes of the laser, improving the trace noise.

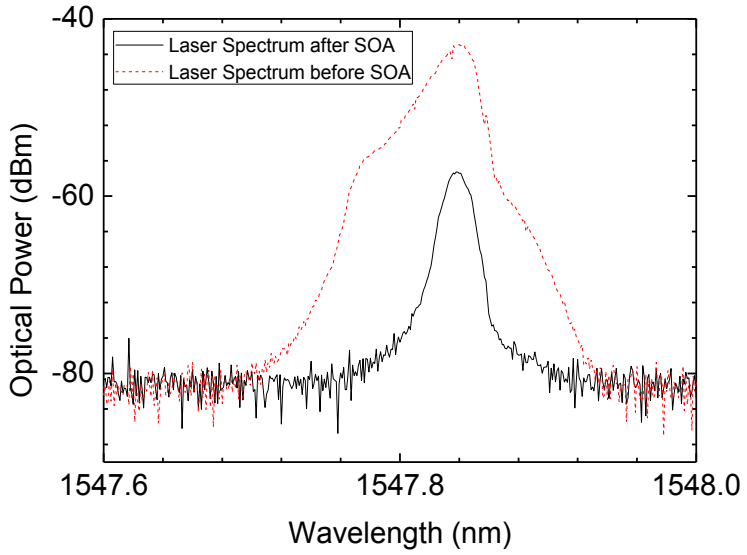

Fig. 3.9 Spectrum of a low coherence laser before and after passing through the SOA.

3.3.3.2 ϕOTDR trace characterization

The main picture of Fig. 3.10 shows a ϕOTDR trace recorded with an ϕOTDR pulse peak power of ~400 mW. In the figure inset, the same trace is shown but the losses along the fibre have been numerically eliminated to improve the visualization. The trace displays the expected random oscillations around the average reflected power. The top

figure shows the visibility of the ϕOTDR interference signal along the fibre, computed as $V=(T_{max}-T_{min})/(T_{max}+T_{min})$ where T_{max} and T_{min} are the maximum and minimum values of the trace over a window of 40 m. Despite the fact that the amplitude of the oscillations and average reflected power decrease exponentially along the fibre due to the losses, the interference does not loose contrast along the propagation (the visibility remains close to 1). Since the sensitivity of ϕOTDR depends mostly on the visibility of the interferences, we can conclude that it remains high along the complete fibre length, although a normal decrease of sensitivity is to be expected towards the fibre end due to the ϕOTDR pulse power attenuation along the fibre. The power limit (which ensures the maximum possible signal amplitude while avoiding nonlinear effects) obtained in this experiment will be later used also as the power limit for the shorter fibre. This way we ensure no visibility impairment due to MI (see section 3.4) [2].

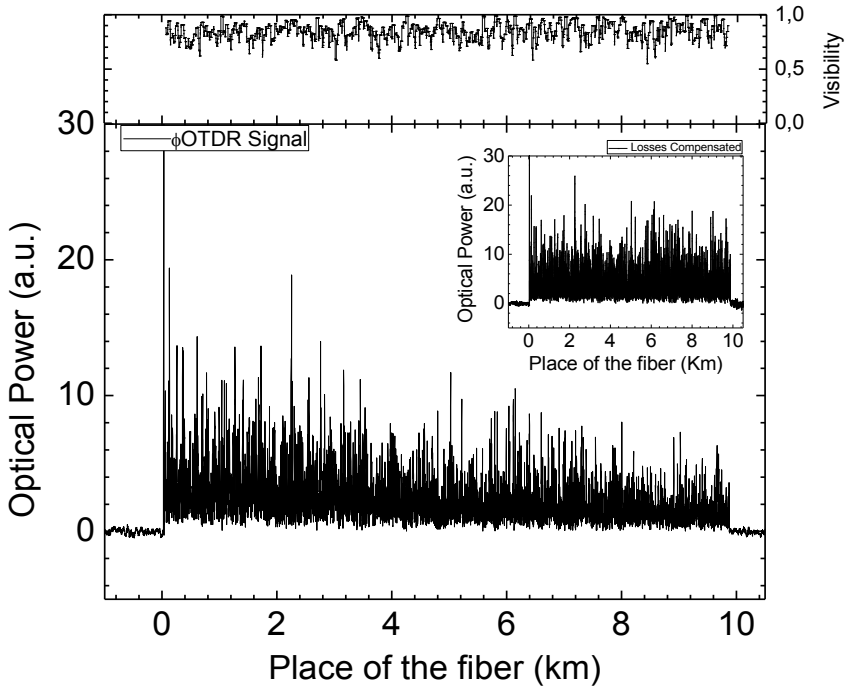

Fig. 3.10 ϕOTDR trace for a pulse peak power of ~400 mW (figure inset: losses have been numerically compensated to improve visualization). The top figure shows the visibility of the trace.

To characterize the intensity statistics and the fading probability in our setup, we built a histogram of the normalized intensities obtained from each position (fibre losses are numerically compensated), for $5 \cdot 10^6$ traces recorded under the same conditions of the one presented in Fig. 3.10, over ≈10 min. The histogram is presented in Fig. 3.11. The beginning and end points of the fibre were excluded to avoid taking into account connector reflections and splice-induced reflections. The theoretical distribution curve

(exponential) is also presented, showing a good agreement with the experimental results. For low and high powers, some discrepancies are observed which we consider acceptable given the bandwidth limitation of the detector and the perturbations induced by noise (they become relevant at four orders of magnitude below the peak). The inset in Fig. 3.11 presents the cumulative probability function of the histogram, i.e., the reflectance fading probability for each optical power level. Again, good agreement between the theory and the experimental results is obtained.

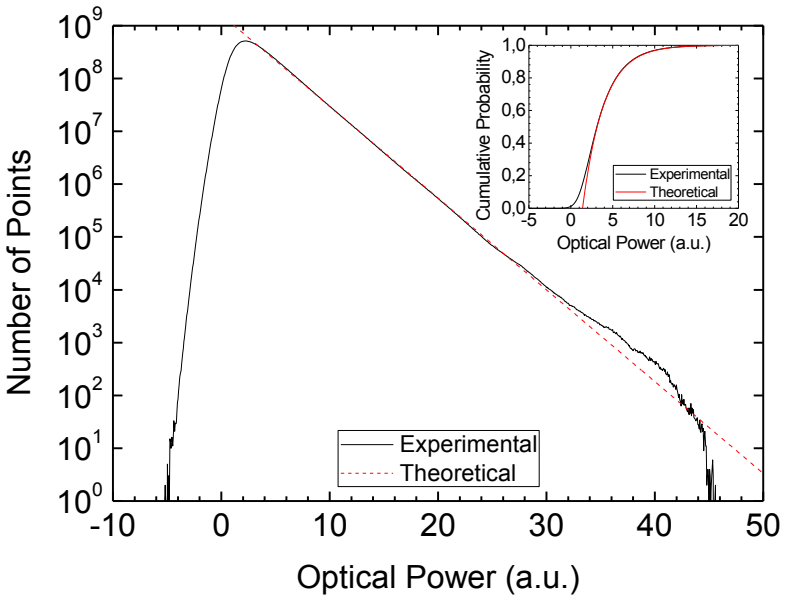

Fig. 3.11 Experimental ($5 \cdot 10^6$ traces obtained under the same conditions of the one presented in Fig. 3.10, over ≈10 min) and theoretical optical intensity distribution in the ϕOTDR trace (figure inset: cumulative probability function).

3.3.3.3 Vibration Measurements

Vibration measurements are carried out by measuring consecutive traces and obtaining the power evolution as a function of time, at each point along the fibre. The sampling frequency at each position corresponds, therefore, to the frequency at which the ϕOTDR pulses are launched into the fibre, which is limited by the maximum fibre length that can be inspected (see eq. 3.2). For ultrasonic vibration measurements, the FUT was replaced with 600 m of SMF-28. Due to the limited re-trigger capability of our acquisition system, the pulse repetition rate could not be made larger than 80 kHz, and therefore the maximum readable frequency corresponds to 40 kHz, as given by Nyquist-Shannon theorem. The far end of the fibre (around 590 metres) was glued with tape inside a PVC tube, 2 m long and 0.08 m of diameter, to which mechanical vibrations of different frequencies were applied using a small vibration exciter with a maximum bare table acceleration of 736 ms^{-2} (with a 75 g mass attached). The fibre was

clamped outside the tube in order to avoid the propagation of vibrations outside this zone. The optical power variation of the ϕOTDR signal was monitored for the 590 metre position (inside the tube) along consecutive traces. We started by using a 20 Hz vibration and monitoring with a sampling rate of 20 kHz during 5 s, without post-processing. This gives traces with very good SNR in the spectral domain, which allowed the characterization of the statistical response of our system without being impaired by noise issues. The first 500 ms of the optical power temporal variation are presented in Fig. 3.12a. A clear pattern, with peaks synchronized with the applied frequency, is observed.

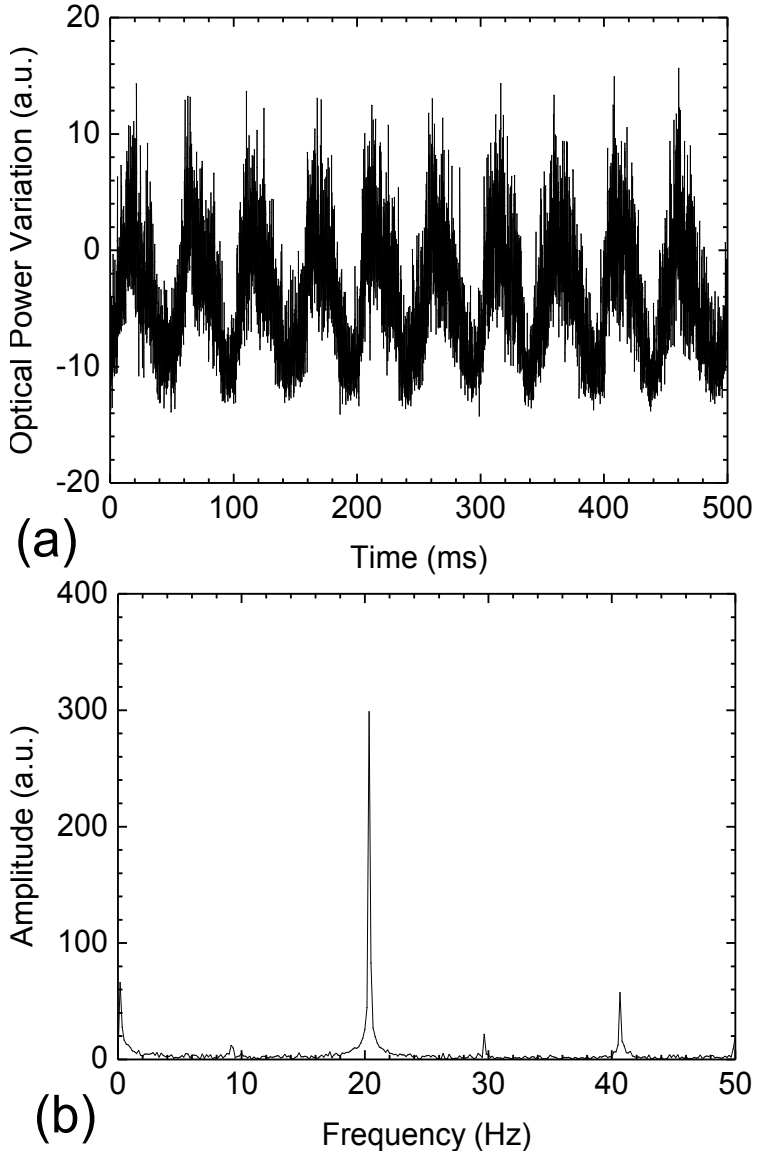

Fig. 3.12 ϕOTDR signal at the position corresponding to the metre length inside the tube (590 m) for an applied vibration of 20 Hz: a) Optical power variation along time and b) respective FFT.

The Fast Fourier Transform (FFT) of the optical power variation at the shaker location is presented in Fig. 3.12b. A clear peak at 20.3 Hz appears, as well as smaller peaks in the second harmonic (40.6 Hz), and multiples of half of the fundamental frequency (10 Hz, 30 Hz). This nonlinear behaviour is partly related to the nonlinear response of the ϕOTDR itself, and also to the mechanical response of the tube. Anyway, given the amplitude difference between the peaks, it can be envisaged that this nonlinearity can be corrected to some extent, if the input stimulus is not too large. Considering the ϕOTDR pulse width (50 ns), the expected resolution should be 5 m. This is in agreement with our measurements since, when the monitored position was more than 5 m away from the shaker position, the optical power variations and respective FFTs no longer showed sensitivity to the applied vibrations.

To characterize the sensitivity statistics of the ϕOTDR, we varied the centre frequency of the LD over a range covering 20 GHz (160 pm). This was done by changing the bias current settings of the LD over a range of approximately 35 mA (with μA resolution). This allowed us to record the vibration at the position of the shaker with varying settings in terms of average detected intensity (as the relative phases depend on the frequency of the laser, the interference in the shaker position experiences many maxima and minima over this sweep). For this entire sweep, we continuously recorded the amplitude of the applied 20 Hz mechanical vibration. Fig. 3.13 presents the normalized amplitude of the 20 Hz peak in the FFT of the optical power variation at the shaker position as a function of the average optical power recorded in that metre. Both axis were divided by the average optical power recorded in order to compare equally all the points. The figure clearly shows that the sensitivity increases for higher average optical powers of the ϕOTDR trace at the measured point, in agreement with the theoretical model. In addition, the histogram shown on the right displays again the expected exponential behaviour.

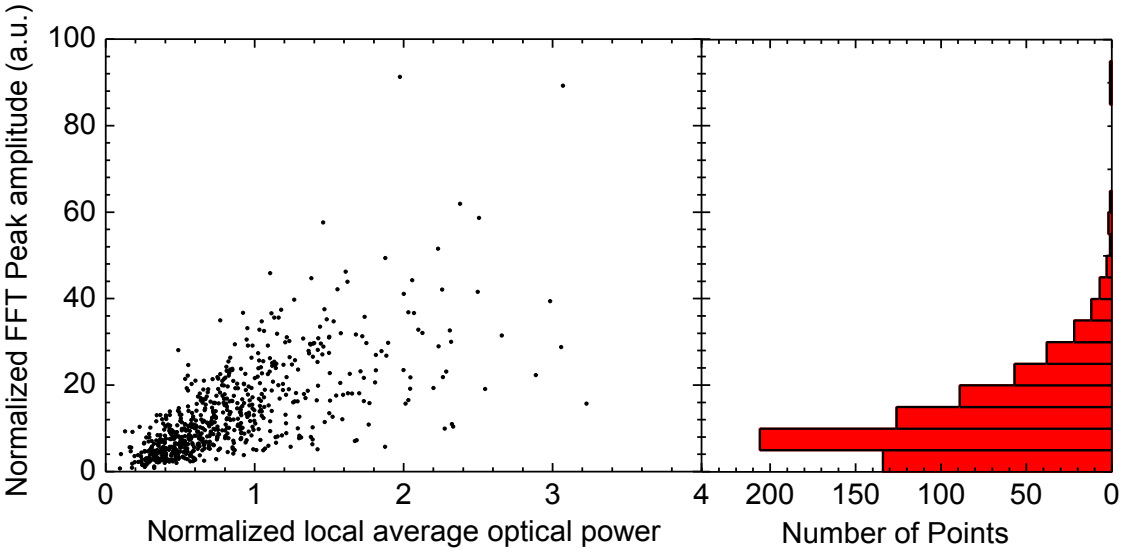

Fig. 3.13 Normalized sensitivity of the measurement as a function of the normalized average optical power of the ϕOTDR trace at the measured point (left) and its histogram (right).

In order to test the acquisition limits of the system, the sampling rate was increased to 80 kHz (maximum allowed by the trigger hold off of the acquisition system, 12 μs) and the acquisition time reduced to 1 s. Fig. 3.14 presents the FFT spectra of the optical power variation recorded by the ϕOTDR at the position of the shaker (590 m) when the frequency applied to the tube is raised from 2 kHz to 39.5 kHz. The recorded spectra show clearly visible peaks at all the applied frequencies, with higher SNR and also higher nonlinearity for lower applied frequencies. This corresponds to the fact that, as the frequency is reduced, the tube displacement is larger. For the maximum frequencies tested, the estimated displacement of the tube is in the sub-micrometer range, which illustrates clearly the extreme sensitivity of this technique. At low frequencies, multiples of 50 Hz are observed below 500 Hz, which we believe could be owed to the mechanical actuator. Considering the clearly visible peak at 39.5 kHz, we believe that higher frequencies could still be recorded with higher sampling rates (not attainable with our acquisition system and this fibre length). Furthermore, although measurements were demonstrated in a fibre span of 600 m, considering the previously demonstrated high visibility of the system for longer distances, no problem should be envisaged in extending the monitored fibre span to 1.25 km (limit allowed by the 80 kHz sampling rate), if the trigger hold off of the acquisition system could be reduced to zero. It is worth mentioning that the presented spectra are not averaged or treated in any way, which means that the performance of the sensor could be increased with proper data treatment for specific applications.

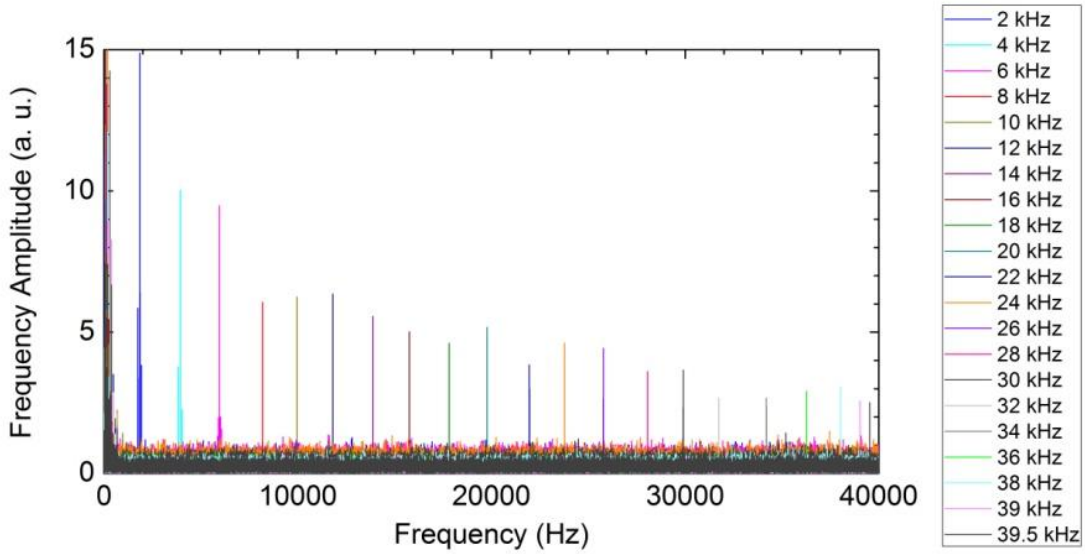

Fig. 3.14 FFT spectra of the optical power variation of the ϕOTDR time signal at a given position for an applied vibration frequency from 2 kHz to 39.5 kHz.

3.3.4 Conclusions

In this section, an experimental and theoretical description of the performance of a high-visibility ϕOTDR used for distributed vibration measurements was presented. The distributed measurement of ultrasonic vibration measurements was achieved, to the best of our knowledge, for the first time. The use of a SOA allowed signals with high SNR, and the ϕOTDR trace was shown to have high visibility over the entire sensing range. The optical intensity distribution and the reflectance fading probability in the ϕOTDR trace was measured and found to be in good agreement with the theoretical model. The sensitivity of the vibration measurement is shown to increase with the average intensity of the trace at the measured point, as predicted. An exponential distribution of the sensitivity was also found, again in good agreement with the theoretical expectation. As for vibration sensing, the optical power variations of the ϕOTDR trace were shown to be synchronized with the applied mechanical vibrations. Frequency measurements in the limits set by the time of flight of light were achieved while maintaining the simplicity of the scheme, as no post-processing, extremely high coherent lasers or coherent detection were required. The sensor was able to measure vibrations of up to 39.5 kHz, with a resolution of 5 m in a range which could go up to 1.25 km. This could be used in vibration-based structural damage identification or monitoring, where ultrasonic waves are sometimes used to detect damages in the structures [113],[114].

3.4 ϕOTDR Pulse Peak Power limitation: Modulation Instability (MI)

3.4.1 Introduction

For a given spatial resolution, the dynamic range and SNR of a ϕOTDR sensor can be achieved by increasing the ϕOTDR pulse peak power. However, the ϕOTDR pulse peak power cannot be indefinitely increased due to the onset of nonlinear effects (see section 3.2.5.1).

In this section, a study aimed to identify the limitations imposed by nonlinearities in ϕOTDR operation is presented. MI is identified as the most important limiting factor, as it is the first nonlinear effect to arise under normal operation conditions. The effects of MI on the performance of ϕOTDR are thoroughly described, both theoretically and experimentally. This study provides an important basis for the understanding of the problems and limitations of ϕOTDR operation, which allows a better maximization of the performance of these systems, when used for both dynamic and static measurements.

3.4.2 Theoretical Model: Pulse propagation affected by MI

The physical principles which lead to the onset of MI, and its consequences in the general case of light propagating on a dispersive medium, have already been discussed in section 2.3.2.1. In this section, in order to provide a proper description of the effects of MI in ϕOTDR operation, we start by theoretically describing the impact of MI on the spectrum of a pulse propagating along an optical fibre. This is done by numerically solving the Nonlinear Schrödinger Equation (NLSE) for the scalar electric field envelope *A(z, t)*:

$$\frac{\partial A}{\partial z}+\frac{i\beta_2}{2}\frac{\partial^2 A}{\partial t^2}-\frac{\beta_3}{6}\frac{\partial^3 A}{\partial t^3}+\frac{\alpha}{2}A=i\gamma\,|A|^2\,A \tag{3.11}$$

Eq. 3.11 was solved using a split-step Fourier algorithm [9] with adaptive step size. The fibre parameters used in the simulation were those of a typical SMF at the wavelength of 1546 nm (the same of the laser used for characterization of the ϕOTDR performance in section 3.3.3): attenuation coefficient α=0.2 dB/km, nonlinear coefficient γ=1.3 $W^{-1}\cdot km^{-1}$, GVD coefficient β_2=-22.8 ps^2km^{-1} (corresponding to a dispersion coefficient D=18 $ps\cdot nm^{-1}km^{-1}$), third-order dispersion (TOD) coefficient

β_3=-0.1 ps^3km^{-1}, and a fibre length of 10 km. The input noise spectrum was considered flat, and different pulse peak powers were simulated.

As expected, for low ϕOTDR pulse peak powers, the effect of MI is negligible and the spectrum remained unaltered along the propagation, being only affected by the fibre losses. However, for high ϕOTDR pulse peak powers, the increase of the MI gain leads to a depletion of the main laser line in favour of the sidebands. This effect is shown in Fig. 3.15, where the simulation of the spectrum evolution for a ϕOTDR pulse peak power of 1.25 W is presented. With increasing distance, this power transfer is observed to be reversed after a certain "minimum" point, and the sidebands transfer back some power to the central line. This is in agreement with previous works describing FPU recurrence exhibited by MI in the strong conversion regime [49, 51]. Over long distances, this reversible power transfer process between the central peak and the sidebands can oscillate several times, although the overall power in the main laser line is observed to decrease rapidly along the fibre length. With increasing powers, the position of the first "minimum" point comes closer to the input end of the fibre, and the number of "minimum" points is increased.

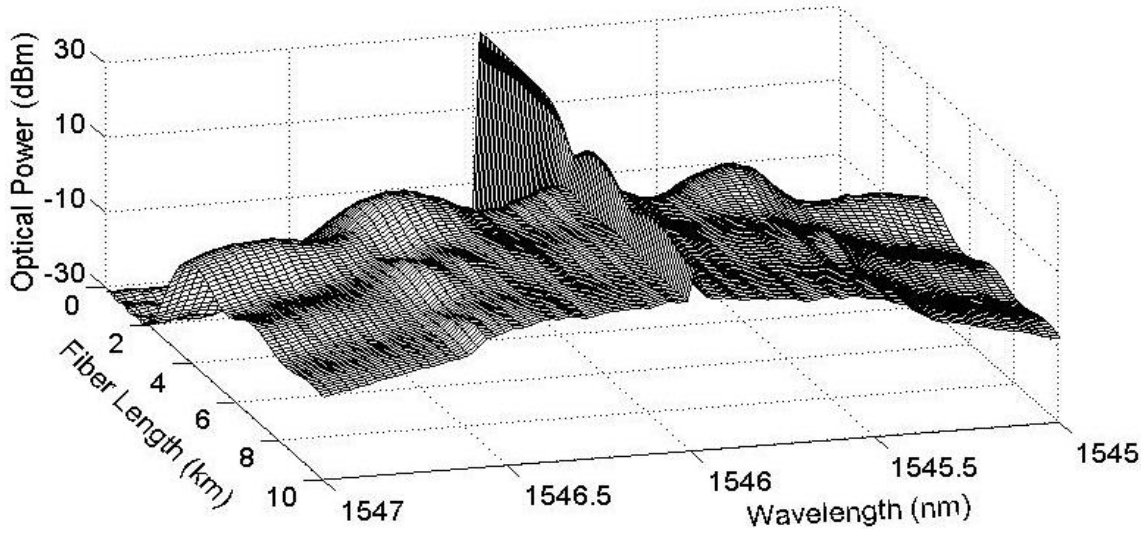

Fig. 3.15 Simulation of the ϕOTDR pulse spectrum evolution along an SMF for a ϕOTDR pulse peak power of 1.25 W.

3.4.3 Experimental Work

The experimental setup used to observe the effect of MI on ϕOTDR is based on a minor adaptation of the setup presented in the previous section (shown in Fig. 3.8). ϕOTDR traces were recorded with increasing values of ϕOTDR pulse powers, and an OSA with

a resolution of 20 pm was used to observe the signal spectrum at the end of the fibre. As for the pulse width, 50 ns square pulses were used.

3.4.3.1 MI impact on the ϕOTDR trace

Fig. 3.16 shows the evolution of the ϕOTDR trace along the fibre for low (~0.35 W, figure inset) and high (~1.25 W, main figure) ϕOTDR pulse peak powers. fibre losses have been numerically compensated along the trace to improve visualization. The theoretical fraction of power contained in the central wavelength is also presented in both cases. The top figure shows the visibility of the ϕOTDR interference signal along the fibre for the main figure signal, computed as $V=(T_{max}-T_{min})/(T_{max}+T_{min})$, where T_{max} and T_{min} are the maximum and minimum values of the trace over a window of 40 m.

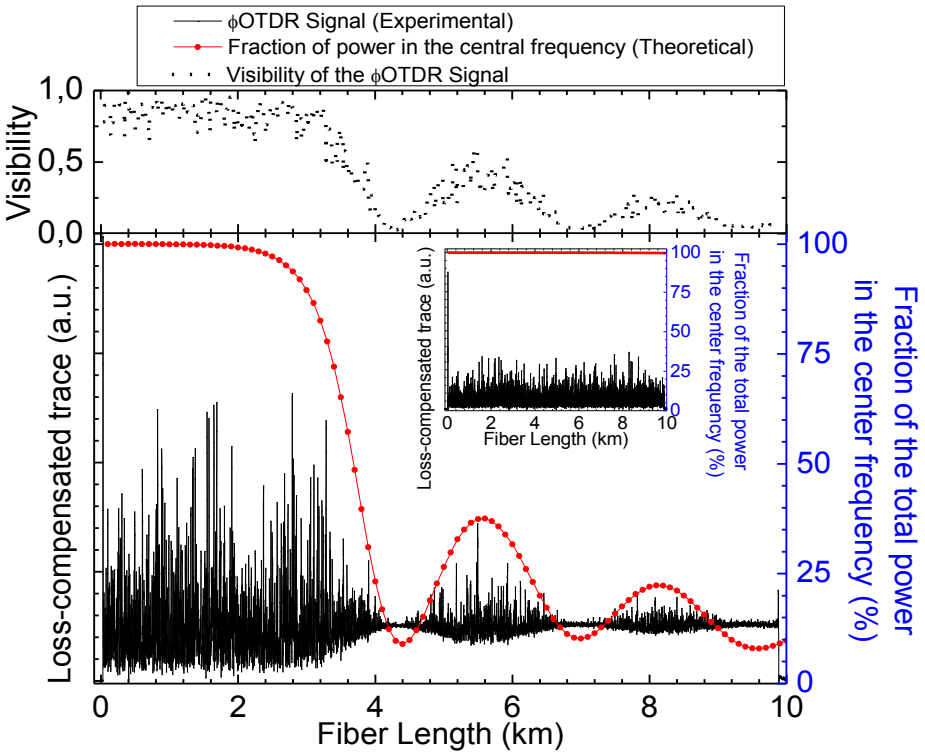

Fig. 3.16 ϕOTDR trace and theoretical fraction of power contained in the central wavelength along the FUT for a ϕOTDR pulse peak power of ~1.25 W (main figure) and ~0.35 W (figure inset). The top figure shows the visibility of the ϕOTDR signal of the main figure.

For low ϕOTDR pulse peak powers (<400 mW), the traces displayed a behaviour similar to the one described in section 3.3. As it is visible, the trace displays the expected random oscillations, where the amplitude of the oscillations remains constant all along the fibre (the interference does not loose contrast along the propagation). With higher ϕOTDR pulse peak powers, we could record complete fading of the trace oscillations (i.e. very low visibility) at specific positions, as shown in Fig. 3.16 (e.g. for 1.25 W pulse peak power, we could record complete signal fading at 4.4 km, 6.8 km

and 9.5 km). Since the sensitivity of the ϕOTDR depends on the visibility of the interferences, we can conclude that at these positions we would have almost no vibration sensitivity. It is also noticeable that the overall sensitivity would also be decreasing rapidly, thus severely reducing the performance of the sensor.

These results can be interpreted as follows: for low powers (<400 mW), the effect of MI is negligible and the coherence of the pulse (and therefore the visibility of the interference) remains high along the fibre. For higher powers, however, the appearance of spectrally broadband sidebands due to MI greatly decreases the coherence of the ϕOTDR pulse (and therefore the visibility of the interference) and the contrast of the oscillations will diminish. When the power transfer is reversed and the sidebands transfer back some power to the central line, the coherence of the pulse is again increased and the ϕOTDR trace recovers the contrast in the recorded interferences. FPU recurrence will therefore lead to an oscillatory behaviour of the visibility of the interferences measured along the fibre.

In this case, the experimental results obtained show an excellent agreement with the theoretical model presented in section 3.4.2. To provide an easier comparison, we plot in Fig. 3.16 the fraction of power contained in the centre wavelength of the simulation as a function of the fibre length (using the same input ϕOTDR pulse power conditions as those recorded for Fig. 3.16). As it is visible, the positions where the contrast of the trace is higher correspond to positions where the theoretical model predicts a high fraction of power in the central wavelength. On the contrary, the positions where the ϕOTDR trace provides the smallest contrast correspond to positions where the power in the central peak is minimal. It is worth remarking that, at the fading points, the peak power in the central line estimated from simulation reached ~10 % of the spectral power, while the measured visibility at these positions was 3-5 %. We believe that this discrepancy may be caused by a non-ideal visibility of the experimental input ϕOTDR pulses and also by a non-flat distribution of the input noise. We have verified by simulation that introducing a higher input noise close to the central peak leads to a deeper depletion of the central line.

3.4.3.2 Pulse spectra at the fibre end (in transmission)

Further insight into this explanation can be obtained by looking at the transmission output pulse spectra. Fig. 3.17 shows a plot of the optical power in the peak frequency

and the integrated power contained in the MI sidebands, as recorded by the OSA at the end of the fibre for different input ϕOTDR pulse powers. The results have been normalized by the total power recorded, and by subtracting the DC component given by the ASE of the EDFA. We can observe an effect similar to the evolution along the fibre, as recorded in Fig. 3.16. For powers below 400 mW, the spectrum recorded at the fibre output shows that >90 % of the power is contained in the central wavelength. Therefore, the visibility of the interference signal is expected to remain high all along the fibre. With increasing input ϕOTDR pulse powers, more power is contained in the sidebands until reaching a minimum. This minimum power recorded in the central peak is also coincident with a minimum contrast of the interferences recorded at the far end of the ϕOTDR trace. The insets of Fig. 3.17 show the output spectra for: (a) 24.5 dBm, (b) 27.8 dBm and (c) 28.8 dBm input ϕOTDR pulse peak powers. A clear peak power decrease and sidebands power increase is observed between the spectra recorded at 24.5 dBm and 27.8 dBm input ϕOTDR pulse power, and then a smaller increase of peak power and decrease of sidebands power can also be observed between the spectra collected at 27.8 dBm and 28.8 dBm input ϕOTDR pulse peak power. This corresponds also to an increase of the interference visibility at the far end of the fibre. A clear signature of the FPU recurrence can therefore be also recorded with this simple graph.

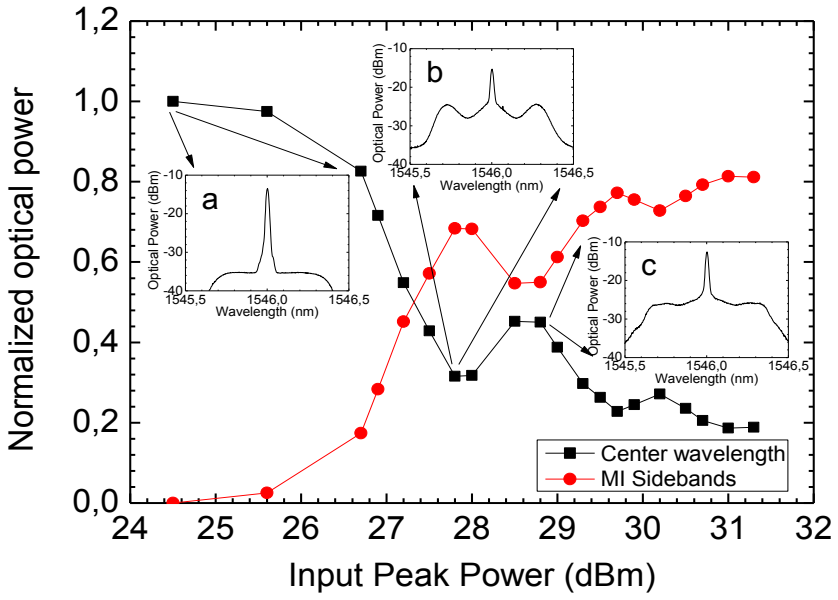

Fig. 3.17 Normalized optical power of the peak and sidebands at the end of the FUT for different ϕOTDR pulse powers (inset figures: spectrum for ϕOTDR pulse powers of: a) 24.5 dBm, b) 27.8 dBm and c) 28.8 dBm).

3.4.4 Conclusions

In this section, we have provided an in-depth explanation of the effects of MI on ϕOTDR traces. We have shown that MI leads to fading (and therefore to loss of sensitivity) in the ϕOTDR trace, associated with loss of power at the narrow laser wavelength in favor of the MI sidebands. The process is position-dependent due to the reversibility of the power transfer between the main ϕOTDR pulse laser line and the MI sidebands (FPU recurrence). The evolution of the interference signal recorded is in agreement with the spectral measurements obtained at the fibre end, the theoretical model and our own qualitative explanation of the obtained results. The presented description of the limitations imposed by MI in ϕOTDR operation provides an important basis to the optimization of schemes using ϕOTDR for both dynamic and static measurements.

While this effect is detrimental in the context of distributed vibration analysis using ϕOTDR, it can also be a convenient and highly visual way of evidencing the FPU recurrence associated with the MI process in optical fibres.

3.5 Extending the sensing range: ϕOTDR assisted by first-order Raman

3.5.1 Introduction

Having achieved frequency measurements in the limits set by the time of flight of light in section 3.3, in this section we focus on extending the sensing range of ϕOTDR operation by using first-order Raman gain to assist it. The spectrum of the ϕOTDR pulse was observed at different points, thus clearly depicting its evolution along the setup and evidencing the impact of the different setup components. The quality of the obtained ϕOTDR trace along the fibre is evaluated using different Raman pump powers, and the results are compared with the theoretical predictions. The noise is characterized both optically and electrically, with special emphasis being given to RIN transfer from the Raman pumps. Special care was also taken to ensure high ER ϕOTDR pulses. Then, distributed vibration measurements were performed over 110 km and 125 km of fibre.

3.5.2 Theoretical Model: ϕOTDR pulse power evolution along the fibre

In this section, we provide a mathematical model for the evolution of the Raman-assisted ϕOTDR trace along the distance. This model just reflects the "average" behaviour of the trace evolution, and not the statistical fluctuations expectable in any ϕOTDR. A detailed statistical analysis of these fluctuations has already been discussed in section 3.3.

For the theoretical model, we assume that two similar continuous-wave (CW) Raman pumps (at 1455 nm) are launched at both ends of the fibre, providing Raman gain (g_R) at the wavelength of the ϕOTDR pulse (1550 nm). The ϕOTDR pulse is shaped from highly coherent light and its wavelength is located near the peak Raman gain of the fibre. In our analysis, the pulse is delivered at $z=0$ into the fibre and propagates in the forward direction (towards increasing values of z). As it travels along the fibre, the Rayleigh backscattered light from the ϕOTDR pulse will create a ϕOTDR signal (at the same wavelength), which propagates backwards until the input end of the fibre, where it is detected. The fibre is supposed to present constant loss at the wavelength of the Raman pump (α_R) and also at the ϕOTDR pulse wavelength (α_P).

In normal operation of a Raman-assisted ϕOTDR, the pulse peak power is about two orders of magnitude below the power of the Raman pumps. Therefore, pump depletion

effects are neglected [23]. For the purpose of knowing the signal evolution along the fibre, our model also neglects ASE created by the Raman pumps and double Rayleigh backscatter. With the above assumptions, the evolution of the forward (+) and backward (-) propagating Raman pump powers along the optical fibre can be obtained by solving the following equations [23]:

$$\frac{dP_R^{\pm}(z)}{dz} = \mp\alpha_R P_R^{\pm}(z). \tag{3.12}$$

As for the evolution of the ϕOTDR pulse power, it can be obtained solving the equation:

$$\frac{dP_P(z)}{dz} = -\alpha_P P_P(z) + g_R P_P(z)[P_R^{+}(z) + P_R^{-}(z)]. \tag{3.13}$$

Considering the boundary conditions given by the optical powers launched into the fibre ($P_R^{+}(0)$ and $P_R^{-}(L)$ are the forward (+) and backward (-) input Raman pump powers, and $P_P(0)$ is the ϕOTDR pulse peak power), the evolution of the Raman pump powers and the ϕOTDR pulse peak power along the optical fibre will be given by [23]:

$$P_R^{+}(z) = P_R^{+}(0)\cdot e^{-\alpha_R \cdot z} \tag{3.14}$$

$$P_R^{-}(z) = P_R^{-}(L)\cdot e^{\alpha_R \cdot (z-L)} \tag{3.15}$$

$$P_P(z) = P_P(0)\cdot e^{-\alpha_P \cdot z}\exp\left\{\frac{g_R}{\alpha_R}P_R^{-}(L)\cdot\left[e^{\alpha_R\cdot(z-L)} - e^{-\alpha_R\cdot L}\right] - \frac{g_R}{\alpha_R}P_R^{+}(0)\cdot\left[e^{-\alpha_R\cdot z} - 1\right]\right\}. \tag{3.16}$$

When the ϕOTDR pulse goes through a given point z_0, the power of the ϕOTDR signal reflected at that point ($P_S^{z_0}(z_0)$) will be given by

$$P_S^{z_0}(z_0) = \alpha_{RayleighBackscatter}\cdot P_P(z_0), \tag{3.17}$$

where $\alpha_{RayleighBackscatter}$ is the Rayleigh backscatter coefficient. Please note that in this case a fully incoherent treatment is given to the scattered power P_S. This considerably simplifies the treatment of the equations and does not harm the main objective of our analysis, which is to determine the overall evolution of the back-scattered signal.

From that point (z_0), the backscattered signal has to travel back to the detector, and therefore should also experience fibre losses and Raman gain. The evolution of the

power of the ϕOTDR signal corresponding to z_0 along the fibre can be obtained by solving the equation

$$\frac{dP_S^{z_0}(z)}{dz} = +\alpha_P P_S^{z_0}(z) - g_R P_S^{z_0}(z)\cdot[P_R^+(z) + P_R^-(z)]. \quad (3.18)$$

Considering the previous equations, we can now establish the evolution of the backscattered ϕOTDR signal corresponding to z_0 for any position $z<z_0$. The evolution of the backscattered power will be given by

$$P_S^{z_0}(z \le z_0) = P_S^{z_0}(z_0)e^{\alpha_P(z-z_0)} \exp\left\{-\frac{g_R}{\alpha_R}P_R^-(L)\left[e^{\alpha_R(z-L)} - e^{\alpha_R(z_0-L)}\right] + \frac{g_R}{\alpha_R}P_R^+(0)\left[e^{-\alpha_R z} - e^{-\alpha_R z_0}\right]\right\}. \quad (3.19)$$

At the detection point (input of the fibre), the ϕOTDR signal corresponding to z_0 ($P_S^{z_0}(0)$) will be:

$$P_S^{z_0}(0) = \frac{P_P(z_0)}{P_P(0)}P_S^{z_0}(z_0) = \frac{P_P(z_0)^2}{P_P(0)}\alpha_{RayleighBackscatter}. \quad (3.20)$$

The values of the parameters used in the theoretical modelling are presented in Table 3.2.

Table 3.2: Values of the parameters used in the theoretical modelling

Symbol	Parameter	Value	Units
$P^+_R(0)$, $P^-_R(L)$	Forward (+) and backward (-) input Raman pump power	600	mW
α_R	Fibre loss at the wavelength of the Raman pump (1455 nm)	0.0553	km^{-1}
g_R	Raman gain at the wavelength of the ϕOTDR pump	0.3	$W^{-1}km^{-1}$
P_P	ϕOTDR pulse peak power	10	mW
α_P	Fibre loss at the wavelength of the ϕOTDR pulse (1550 nm)	0.047	km^{-1}
$\alpha_{Rayleigh\ Backscatter}$	Rayleigh Backscatter coefficient	-72	dB/m

3.5.3 Experimental Work

3.5.3.1 Setup

The experimental setup used to characterize ϕOTDR assisted by first-order Raman amplification is shown in Fig. 3.18, consisting of an improvement of the setup reported in sections 3.3 and 3.4 (described in detail after Fig. 3.8), to which a first-order Raman amplification scheme and balanced detection were added.

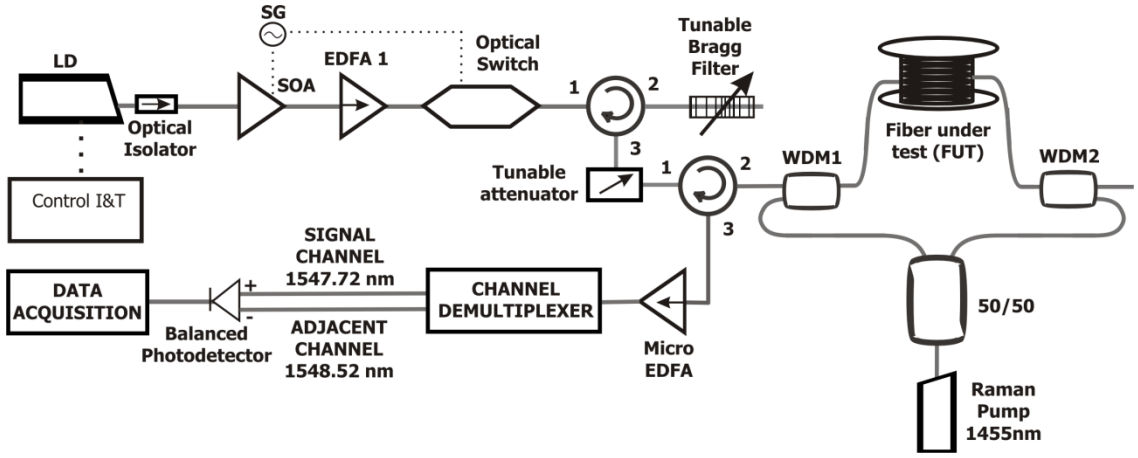

Fig. 3.18 Experimental setup of ϕOTDR assisted by first-order Raman amplification.

The initial part of the setup (used to generate the ϕOTDR pulse before coupling it into the FUT) was, therefore, very similar to the setup depicted in Fig. 3.8, having a few (but critical) adaptations: the length of the ϕOTDR pulse was 20 m (instead of 10 m) and an optical switch was placed after the EDFA. The optical switch had rise/fall times of 200 ns and a typical ER of 25 dB. It was driven so as to have a sub-microsecond transmission window synchronized with the pulse. This system allows a further increase in the ER, reducing the noise delivered into the fibre outside the pulse interval. As shown in section 3.3, the ER has a very high impact on the SNR of the detected trace in normal ϕOTDR operation [3].

Regarding the first-order Raman amplification scheme, the FUT (110 km of SMF-28) was connected to the common ports of two wavelength division multiplexers (WDMs) (1450/1550 nm) which have an isolation >60 dB in the pass channel. The ϕOTDR pulse was launched into the FUT through the 1550 nm port of the WDM1. The Raman pump is a CW Raman fibre Laser (RFL) emitting at 1455 nm with a RIN <-110 dBc/Hz. The power of this laser can be tuned up to 2 W. The RFL beam was divided by a calibrated 50/50 coupler in two beams, and each beam was then coupled into the 1450 nm ports of the WDMs.

The signal back-reflected from the fibre was amplified (using a micro-EDFA) and then fed into a 100 GHz channel demultiplexer, which filtered out the channel of the signal (centered at 1547.72 nm) and an adjacent channel (centered at 1548.52 nm), thus filtering out the ASE added by the micro-EDFA. The signal channel and the adjacent channel were then respectively coupled to the “+” and “-” ports of a p-i-n balanced photodetector with amplification, and 100 MHz bandwidth. In this case, the “+” port

received the sum of signal and noise with a bandwidth of 100 GHz and the "-" port received the noise of an adjacent channel with the same bandwidth. Since the optical paths leading to the "+" and "-" ports were the same (within 1 cm tolerance), a maximum cancelation of the RIN was ensured. The detector's bandwidth should ideally be much larger than the pulse spectral bandwidth, since the ϕOTDR traces exhibit high-contrast rapid oscillations. In our case, the detector has a bandwidth roughly ten times larger than the pulse spectral bandwidth which is enough to adequately represent the process. The signal was then recorded using a high-speed digitizer.

3.5.3.2 Noise Considerations: ASE, RIN transfer and Balanced detection

As discussed in section 3.3.2.2, noise suppression between the ϕOTDR pulses in these types of systems is very important since it reduces the intra-band coherent noise of the setup. In the conventional setups, the use of a SOA allows achieving a high ER (>50 dB), and enhances the spectral purity of the laser spectrum in the active state due to spectral hole burning in the active material [3].

In the present setup, an optical switch was also used in order to further increase the ER of the ϕOTDR pulses. This switch "windows" the ϕOTDR pulses and, therefore, avoids the leakage of a significant amount of noise between the ϕOTDR pulses. To illustrate the impact of the optical switch, the spectrum of the ϕOTDR pulse after the FBG, with the switch "on" and "off", is presented (Fig. 3.19). The effect is clearly visible as a strong reduction in the ASE noise (as much as 22.5 dB reduction). This combination of SOA and optical switch results in a ϕOTDR pulse with very high ER and coherence, and a very low ASE noise delivered into the fibre.

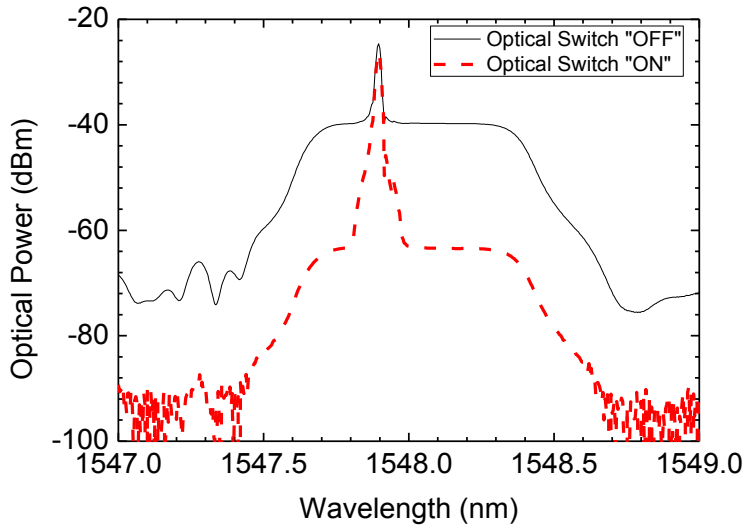

Fig. 3.19 Spectra of the ϕOTDR pulses after passing the optical switch in the "on" and "off" states

Fig. 3.20a shows the spectrum reflected from the FUT (i.e., the ϕOTDR signal) before the micro-EDFA. As expected, a background noise (with the spectral power distribution similar to the Raman gain curve) is observed due to the ASE introduced by the Raman amplification in the FUT. Further amplification in the micro-EDFA introduces more ASE noise. Even after spectral filtering, this ASE noise is comparable to the signal level, and therefore requires some kind of elimination strategy. Moreover, the effect of RIN is strongly manifested in this ASE noise.

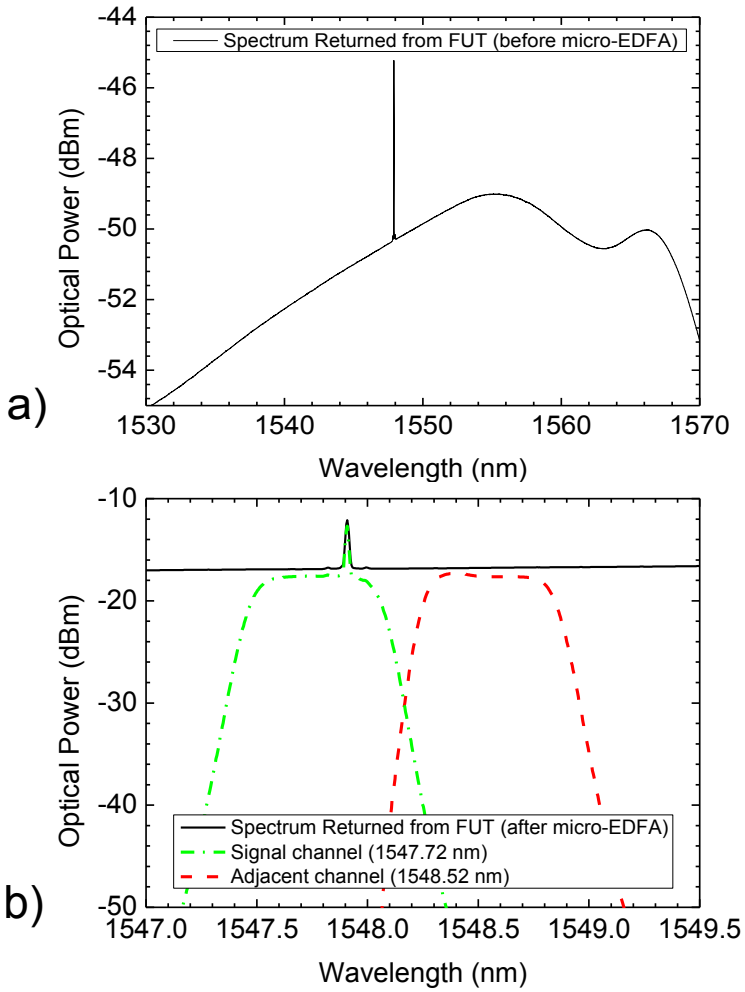

Fig. 3.20 Optical spectrum returning from the FUT: a) before the micro-EDFA and b) after the micro-EDFA (including signals received in the "+" and "-" ports of the balanced detector (signal channel and adjacent channel)).

The use of balanced detection between two adjacent channels (one with signal+ ASE noise and the other with ASE noise only) allows suppressing the strong and very noisy DC component given by Raman ASE noise. The optical spectra of the signal channel (1547.72 nm) and the adjacent channel (1548.52 nm) received in the balanced detector are shown in Fig. 3.20b. As we see, the amount of ASE noise subtracted is roughly equal in both channels. Furthermore, a power fluctuation in the Raman pump laser at a

given time will similarly affect the ASE level in both channels and, therefore, by using the difference between them, the effect of the RIN in the detected power along time is greatly diminished. Of course, for this noise cancellation to be efficient, the optical paths of the "+" and "-" signal in the detector have to be the same, as length mismatches are translated into a reduction of the bandwidth over which a perfect noise cancellation is achieved. For a bandwidth of 100 MHz, the detected power for each point is the average of the power which reaches the detector over ~10 ns (i.e. average of a light pulse that covers ~2 m of fibre) and therefore we can assure that noise cancellation will be effective with tolerances on the order of 1 cm in the optical paths of the "+" and "-" signal.

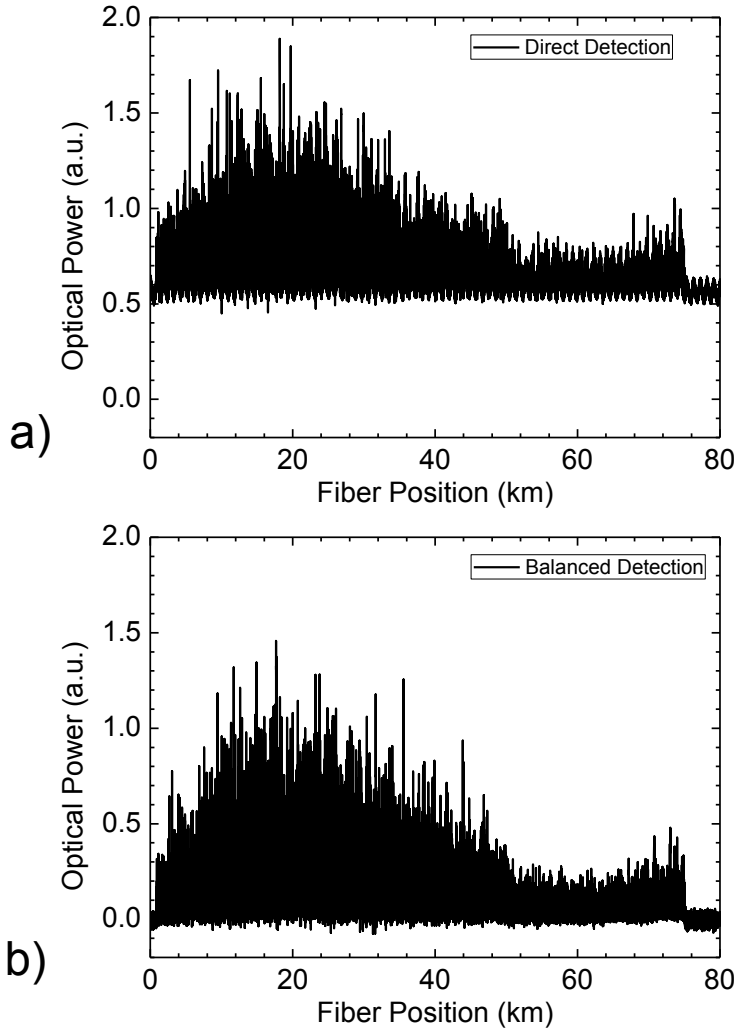

Fig. 3.21 Comparison of the RIN for a) Direct b) Balanced detection in a 75 km FUT.

To illustrate the improvement of balanced detection in comparison with direct detection, the two schemes are compared in a situation in which the RIN is very high and its effects are noticeable (even in the time domain) in a 75 km fibre span (Fig. 3.21). Fig.

3.21a shows the trace detected employing conventional direct detection, and Fig. 3.21b shows the trace detected with our balanced detection scheme. The improvement is clearly visible as the periodical noise of the RIN shown using direct detection (Fig. 3.21a) is greatly reduced using balanced detection (Fig. 3.21b). Also, as expected, the DC component of the trace is eliminated.

In order to characterize the RIN transferred from the Raman pumps, a Raman pump power of 0.6 W was launched from each end of a 125 km FUT without input ϕOTDR pulse. The signal returning from the fibre was then measured (photodetector+electrical spectrum analyzer, ESA) using direct and balanced detection. Results are presented in the electrical spectrum domain (Fig. 3.22). It was observed that the direct detection presents a periodical structure with peaks at 140 kHz (which are coincident with the period of ~700 m of the RIN observed in Fig. 3.21a). This period comes from the cavity length of the RFL. Strong low frequency noise (<100 kHz) is also observed in the direct detection, which would greatly affect the comparison of equivalent points from different traces and, therefore, the vibration measurements. Using balanced detection, only white noise is observed, proving the usefulness of this approach.

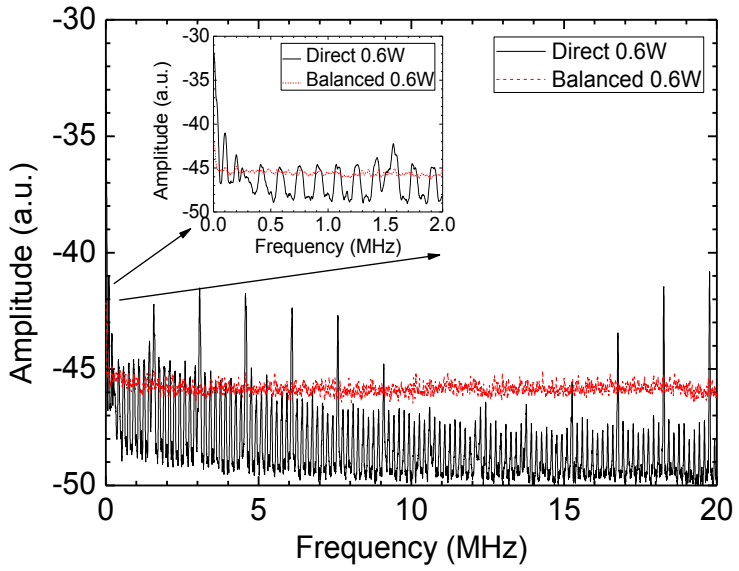

Fig. 3.22 RIN noise returned from 125 km FUT for a Raman pump power of 0.6 W launched on each end of the fibre, without input ϕOTDR pulse, using balanced and direct detection.

3.5.3.3 ϕOTDR Traces

Fig. 3.23 shows the ϕOTDR traces recorded for fibre spans of 110 km (Fig. 3.23a) and 125 km (Fig. 3.23b). As expected, the traces display random oscillations and their amplitudes vary with the ϕOTDR pulse power evolution along the fibre. In both cases,

the Raman pump power launched on each end of the fibre was 0.6 W (the same power which was used for RIN characterization). As for the input ϕOTDR pulse peak power (estimated to be below 10 mW for both Fig. 3.21a and Fig. 3.21b), it was chosen so as to ensure the best performance along all points of the fibre, i.e., the highest possible power before the appearance of nonlinearities (mainly MI, which leads to a fast decrease of the visibility, as discussed in section 3.4) [2].

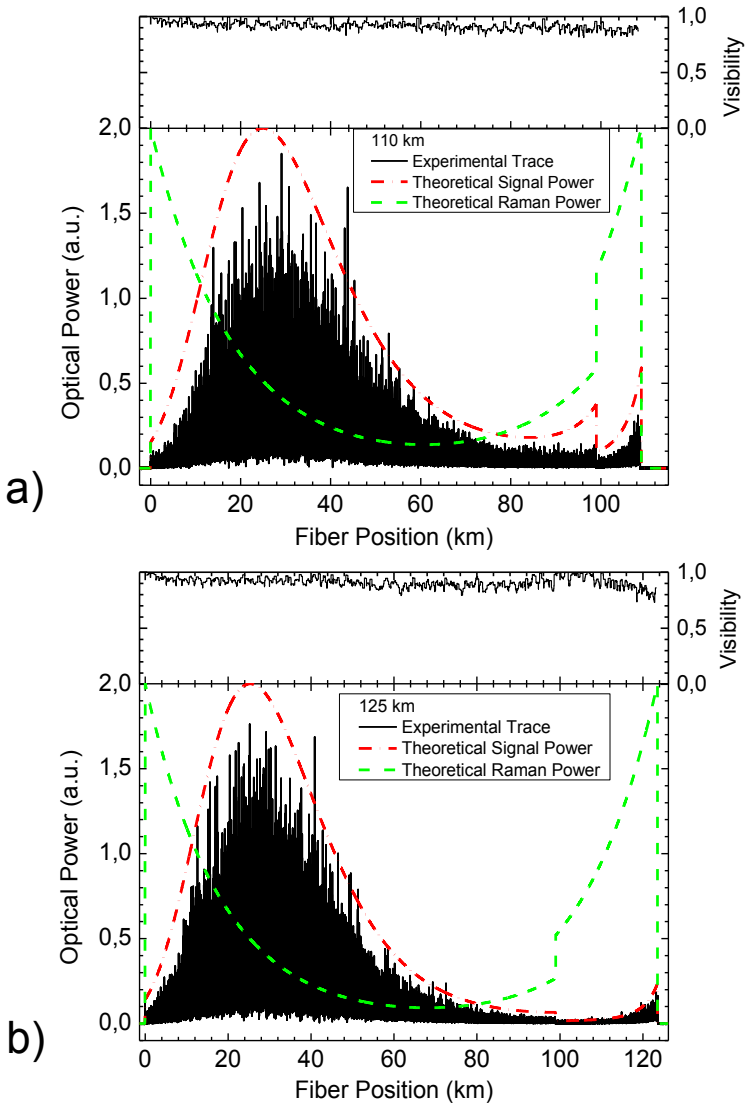

Fig. 3.23 ϕOTDR trace for a FUT of a) 110 km and b) 125 km. The Raman pump power launched on each end of the fibre was 0.6 W and the ϕOTDR pulse power was chosen as the one ensuring the best performance in both cases. The theoretical modeling of the Raman pump power and ϕOTDR pulse power along the FUT is also presented. The top figure shows the visibility of the interference signal.

As clearly visible in Fig. 3.23a, a considerable decrease in the amplitude of the trace oscillations at ≈98 km is observed. A similar oscillations' amplitude decrease occurs at the same point in Fig. 3.23b. This is due to a connector loss at this point (estimated as 3 dB). It is important to mention that the point where the measurements were performed

was immediately after the connector loss. Therefore, if the fibre was spliced at that point, this amplitude drop of the trace oscillations would not occur and better results could have been obtained. However, as the vibrations were clearly measured, this loss was kept so as to prove the efficiency of our setup even in deteriorated conditions. It essentially proves that reliable vibration measurements can be performed well beyond the range of 100 km using this scheme.

The evolutions of the Raman pump power and of the ϕOTDR pulse power, given by the theoretical model (which includes the 3 dB loss due to the connector at ~98 km), are also presented and shown to be in good agreement with the experimental results. Although small differences can be expected for several reasons (the fibre may present small inhomogeneities along the distance, some of the parameters in Table 3.2 may show small errors), the evolution of the amplitude of the trace oscillations is shown to be coincident with the ϕOTDR pulse power evolution along the fibre and the Raman pump power evolution is as qualitatively expected. The top figures show the visibility of the ϕOTDR interference signal along the fibre, computed as $V=(T_{max}-T_{min})/(T_{max}+T_{min})$, where T_{max} and T_{min} are the maximum and minimum values of the trace over a window of 500 m. Despite the fact that the amplitude of the oscillations and the average reflected power present large variations along the fibre, the variations of the contrast of the interference are much lower (the visibility remains close to 1). Since the visibility of the ϕOTDR trace is not altered along the fibre, we can conclude that reliable vibration measurements can be performed at any position along the fibre as long as it can be ensured that vibration measurements are possible in the position of worst signal level (around km 100 in both cases). Thus, the vibration measurement tests were done in this position.

Although only bi-directional Raman amplification results are presented in this thesis, the co-propagating and counter-propagating Raman amplification configurations were also tested, and observed to perform worse. The reason for this is that larger signal variations are obtained with these configurations. The bi-directional configuration ensures the minimum variation of signal power along the fibre, and therefore the best possible performance.

3.5.3.4 Evolution of the ϕOTDR trace for different Raman Pump powers

The evolution of the trace profile for increasing Raman pump powers (0.6, 0.9, 1.2 and 1.5 W of total Raman input power, half inserted on each side) using a FUT of 110 km is shown in Fig. 3.24. Again, the input ϕOTDR pulse power was adjusted for each Raman pump power to achieve the best possible performance while avoiding nonlinearities. Thus, for increasing Raman pump powers, the input ϕOTDR pulse power was decreased. It was observed that for Raman pump powers higher than 1.2 W (0.6 W on each side), the point with the lowest amplitude of trace oscillations was at the beginning of the fibre. This high pumping level is, nevertheless, not used in practice, as the Raman noise is too large for performing reliable vibration measurements.

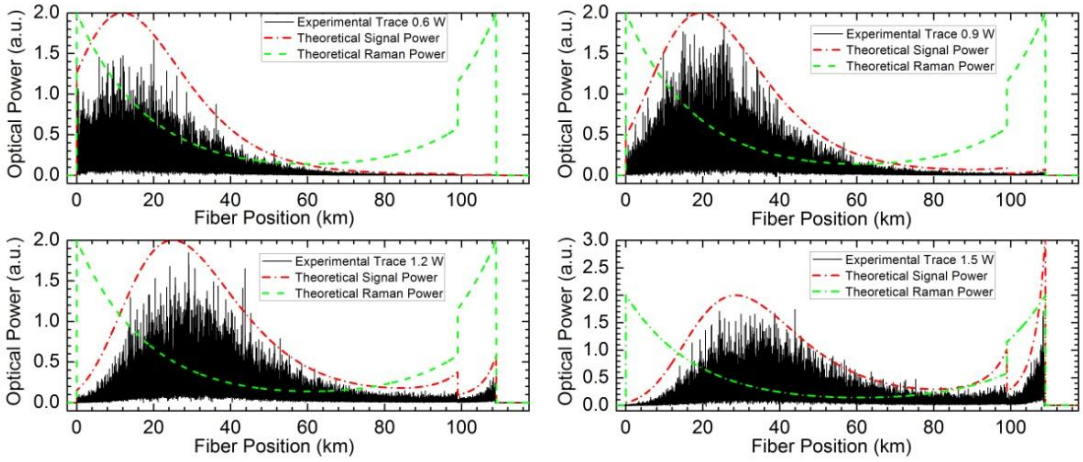

Fig. 3.24 Experimental and theoretical evolution of the trace profile for different Raman pump powers (total Raman input power), using a FUT of 110 km. The ϕOTDR pulse power chosen for each Raman pump power was the one ensuring the best performance.

In agreement with eq. 3.16, it can be seen that, for increasing Raman pump powers, the maximum of the input ϕOTDR pulse power (when the Raman gain equals the fibre losses) occurs further into the fibre. This is the point at which Raman gain and linear fibre loss are equal. This condition will occur always for a certain level of Raman pump power, so for higher input Raman powers, this maximum comes obviously further inside the fibre.

3.5.3.5 Vibration Measurements

Vibration measurements were carried out in a similar manner to the methodology described in section 3.3. For each point along the fibre, the optical power evolution as a function of time was obtained by measuring the equivalent point in consecutive traces and plotting the signal levels recorded for that point against the time. The sampling frequency at each position will, therefore, be the frequency at which the ϕOTDR pulses

are launched into the fibre, which is limited by the fibre length to be monitored (see eq. 3.2).

Two FUT lengths were tested: 110 km and 125 km. These consisted of two fibre spools of 50 km and one fibre spool of 10/25 km of SMF-28, all linked by optical connectors. The ϕOTDR pulse repetition rate was 781/625 Hz, which limits the maximum detectable frequency to 390.5/312.5 Hz (Nyquist-Shannon theorem) and the theoretical maximum fibre span to be monitored to 131/163 km.

The Raman pump power and the input ϕOTDR pulse power were the same as the ones used in the traces of Fig. 3.23a and Fig. 3.23b. The point with the lowest amplitude of the trace oscillations, which in both cases was observed to be after the connector at ≈98 km, was placed inside a 2 m long PVC tube with 0.08 m of diameter, to which mechanical vibrations of controllable frequency were applied using a small vibration exciter with a maximum bare table acceleration of 736 ms^{-2} (with a 75 g mass attached). The fibre was clamped outside the PVC tube in order to avoid the propagation of vibrations outside it.

Fig. 3.25a shows the optical power variation of the ϕOTDR signal at the point inside the PVC tube, when a 40 Hz vibration was applied to the tube. The trace was recorded using the same conditions of Fig. 3.23a (FUT=110 km) with no post-processing. A clear pattern, with peaks synchronized with the applied frequency, is observed. The FFT of the optical power variation is presented in Fig. 3.25b. The ϕOTDR signal is observed to present a nonlinear response, as a clear peak appears at 40 Hz followed by a smaller peak in the second harmonic (80 Hz). The optical power variations of the ϕOTDR signal and respective FFTs of fibre points, which were more than 10 m away from the PVC tube, did not show sensitivity to the applied vibrations. This is in agreement with the expected resolution of 10 m (corresponding to a 100 ns pulse).

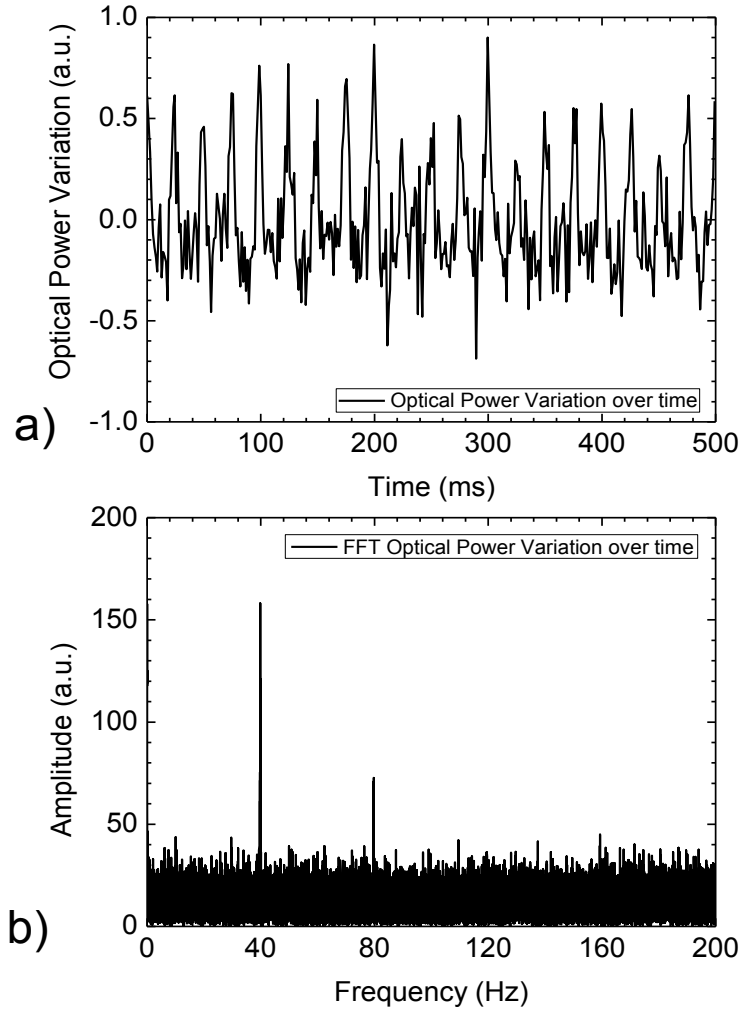

Fig. 3.25 ϕOTDR signal at the fibre point with the minimum amplitude of the trace oscillations (km 98) of the 110 km FUT, using the same conditions of Fig. 3.23a, for an applied vibration of 40 Hz: a) Optical power variation along time and b) respective FFT.

In order to test the acquisition limits of the system, frequencies up to nearly the maximum detectable by the ϕOTDR pulse repetition rate were applied to the PVC tube, for each FUT. Fig. 3.26 presents the FFT spectra of the optical power variation recorded by the ϕOTDR at the position of the shaker when the frequency applied to the PVC tube was raised from 10 Hz to 300 Hz using the FUT of 110 km (Fig. 3.26a), and 10 Hz to 250 Hz using the FUT of 125 km (Fig. 3.26b). In both cases, the measurement conditions are the same as those used in Fig. 3.23 for each FUT.

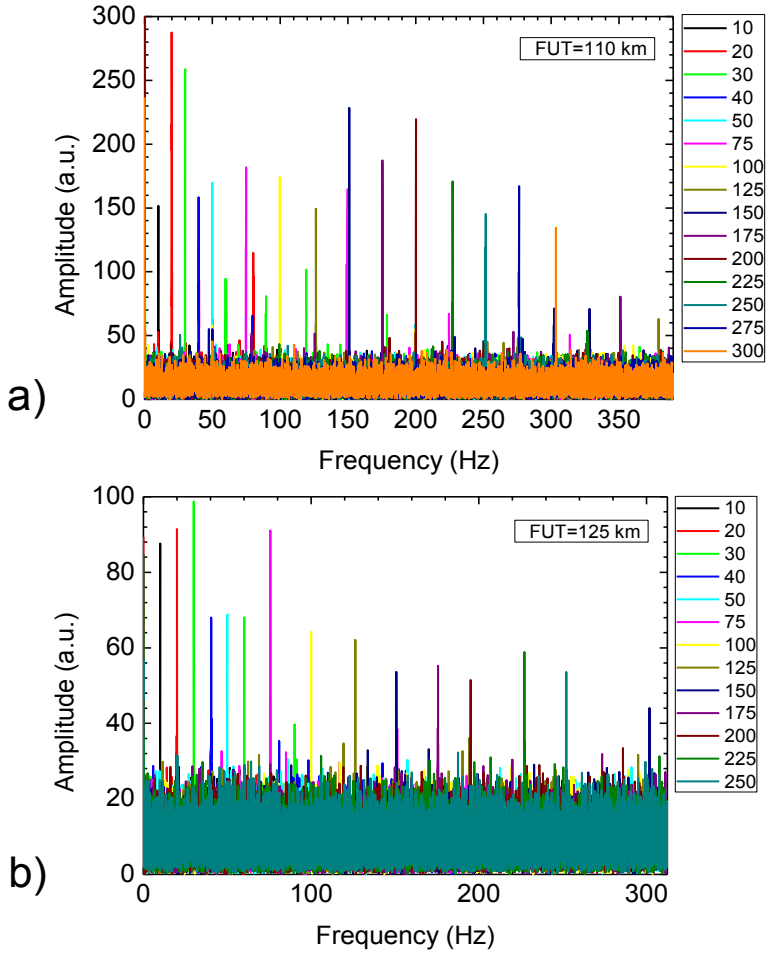

Fig. 3.26 FFT spectra of the optical power variation of the ϕOTDR signal along time in the fibre point with minimum amplitude of the trace oscillations (after km 98) of the a) 110 km and b) 125 km FUT for applied frequencies between 10 Hz and a) 300 Hz and b) 250 Hz, using the same conditions of Fig. 3.23 for each FUT.

The recorded spectra showed clearly visible peaks at all the applied frequencies, although the amplitude of the detected frequencies was observed to have some instability. As expected, the measurements using the FUT of 110 km presented a higher SNR than when using the FUT of 125 km.

For the maximum frequencies tested, the estimated displacement of the PVC tube was in the sub-millimeter range. It is important to stress that the point where the measurements were performed was immediately after a lossy connector, in the position with the lowest sensitivity of the whole trace. Also, no post-processing was used in the presented data and therefore, to some extent, the performance of the sensor could be increased with proper data treatment for specific applications.

3.5.4 Conclusions

This section, presents experimental and theoretical descriptions of the use of first-order Raman amplification to improve the performance of a ϕOTDR, when used for vibration measurements. The evolution of the ϕOTDR signal along the fibre is shown to be in good agreement with the theoretical model for different Raman pump powers. The Raman amplification combined with the noise reduction provided by the use of balanced detection, a SOA and an optical switch, allows to greatly increase the SNR and the sensing range of the ϕOTDR. Frequency measurements close to the limits set by the time of flight of light pulses were achieved this way in a range which, to our knowledge, is the highest for ϕOTDR vibration sensing achieved at the time of publication of ref. [5]. The sensor was able to detect vibrations of up to 250/300 Hz at a distance of 125/110 km, with a resolution of 10 m, without post-processing. This sensor could be used to monitor intrusions in large structures, such as national borders or pipelines. The best performance was achieved using the scheme of bi-directional Raman pumping, which is a clear drawback of the setup, as access to both fibre ends is required. However, unlike the case of Brillouin Optical Time Domain Analyzers, in this scheme there are no restrictions in terms of having the two access points in the same place, as the Raman pumps on each side can be physically separated. In addition, depending on the application (for instance, using a circular geometry to monitor the perimeter of a military base), the use of bi-directional pumping may not be at all a limitation.

3.6 Extending the sensing range: ϕOTDR assisted by second-order Raman

3.6.1 Introduction

The use of second-order Raman amplification to assist ϕOTDR operation is presented in this section. The noise, signal evolution along the fibre and spatial resolution are discussed, and the distributed detection of vibrations over 125 km is characterized. The sensor is compared with the first-order Raman-assisted ϕOTDR presented in the previous section (3.5), and observed to present a better performance.

3.6.2 Experimental Setup

The experimental setup used to characterize the second-order Raman-assisted ϕOTDR (shown in Fig. 3.27) is based on a couple of minor adaptations of the setup used in the previous section (3.5) to characterize first-order Raman amplification (Fig. 3.18): (1) a second-order (instead of first-order) Raman amplification scheme was used, (2) a different tuneable filter was used after the EDFA, which presented an approximate gaussian profile with 0.2 nm FWHM, replacing the 0.8 nm FBG with a typical spectrum of a 100 % reflection which was previously used. Similarly to the first-order Raman setup (Fig. 3.18), the ϕOTDR pulse length was also 20 m and an optical switch was used after the EDFA, with rise/fall times of 200 ns and a typical ER of 25 dB, driven as to realize a sub-microsecond transmission window synchronized with the pulse. This ensures a reliable comparison between the performance of the two schemes.

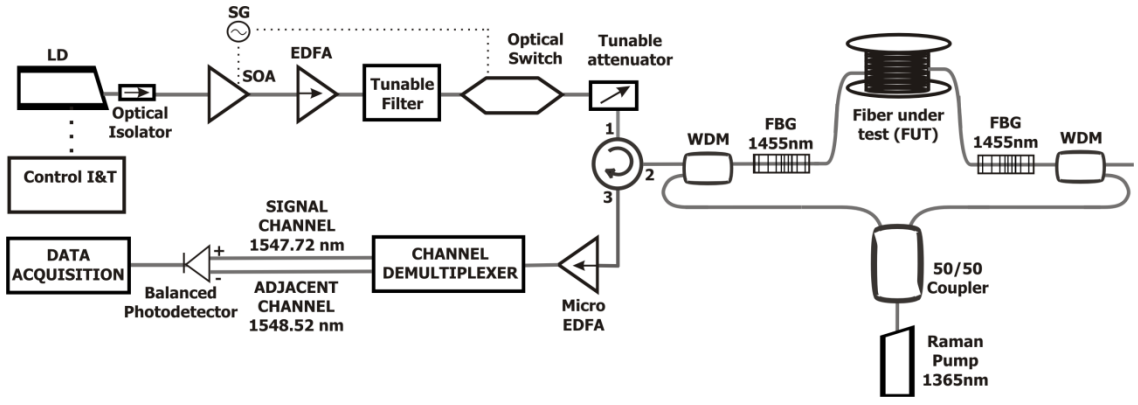

Fig. 3.27 Experimental setup of ϕOTDR assisted by second-order Raman amplification.

A full description of the initial part of the setup (used to generate the ϕOTDR pulse before coupling into the FUT) can be found in the description of Fig. 3.8, for the ϕOTDR scheme without amplification. Regarding the second-order Raman

amplification scheme, the FUT (125 km of SMF-28) is connected to the common ports of two WDMs (1310/1550 nm). The ϕOTDR pulse is launched into the FUT through the 1550 nm (1460-1620 nm) port of WDM1. The primary Raman pump is a Raman fibre Laser (RFL) emitting at 1365 nm with RIN <-105 dBc/Hz. The power of this laser can be tuned up to 5 W. The RFL beam is divided by a calibrated 50/50 coupler in two beams, and each beam is then coupled into the 1310 nm (1270-1350 nm) ports of the WDMs. Two FBGs centred at 1455 nm, with 0.5 nm FWHM and with 80 % reflectivity, are placed at both ends of the fibre, thus creating an ultralong Raman fibre laser (URFL) cavity. It is important to understand the dynamics of this URFL in order to understand the advantage of this setup over first-order Raman assistance. If the URFL had a resolvable mode structure, it would have a spectral mode spacing of $\Delta\upsilon \approx 0.8$ kHz$=c/(2nL)$, where c is the velocity of light in the vacuum, n is the refractive index, and L is the FUT length. In practice however, and depending on the pump power applied, the mode structure can be partially or totally erased due to Rayleigh backscattering and the four-wave mixing between the multiple modes [55]. Either way, the RIN introduced by the second-order Raman amplification (see Fig. 3.28) is mostly transferred to a much lower frequency range [62] than the typical frequencies (~10's of MHz) of schemes using first-order Raman amplification (see Fig. 3.22). This is a key advantage, as the balanced detection implemented in the setup will provide a better suppression of the common-mode noise. The power variation of the URFL along the FUT will also be lower than the power variations of the primary RFL pumps.

Similarly to the first-order Raman assisted setup (Fig. 3.18), the signal back-reflected from the fibre is amplified (using a micro-EDFA) and then goes through a 100 GHz channel demultiplexer before reaching a balanced photodetector. Since the optical paths leading to the "+" and "-" ports are the same (within 1 cm tolerance), effective cancelation of the RIN noise is ensured. The signal was then recorded using a high-speed digitizer.

3.6.3 RIN noise: Balanced VS Direct detection

Fig. 3.28 shows the signal returning from the fibre in the electrical spectrum domain when a 28.5 dBm Raman pump power was launched on each side of the FUT without input ϕOTDR pulse, for direct and balanced detections. This was observed as the best Raman pump power for balanced detection (and was later used for the measurements), since for higher powers the noise of the signal was observed to increase abruptly, due to

strong RIN transfer from the Raman pumps. As we see, most of the RIN noise in this case is transferred to a frequency region below 5 MHz, where the balanced detection should be very effective eliminating the noise. In the balanced detection case, only white noise and a small peak at 0.2 MHz were observed. This frequency comes from the cavity length of the RFL, which is approximately 500 m. As expected from the results of section 3.5 (see Fig. 3.22), direct detection performed much worse and a periodical structure with peaks every 0.2 MHz was observed for the same Raman pump powers. In addition, peaks with ~4 MHz spacing appeared in the electrical spectrum, corresponding to the cavity round-trip time of the master pump laser in the RFL.

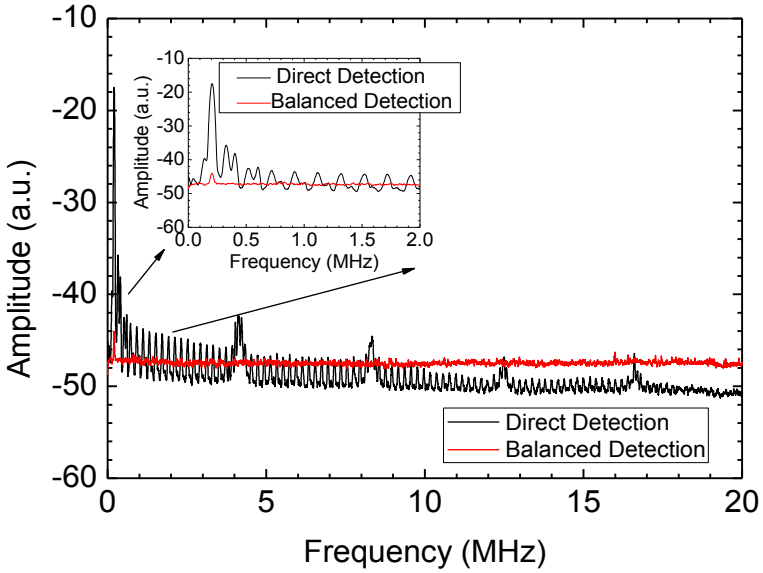

Fig. 3.28 Characterization of the noise in the electrical spectrum domain of the signal returning from the fibre when a Raman pump power of 28.5 dBm is launched on both ends of the FUT without input ϕOTDR pulse, using balanced and direct detections.

3.6.4 ϕOTDR trace

Fig. 3.29 shows the ϕOTDR trace recorded with a Raman pump power launched on each end of the FUT of 28.5 dBm. The ϕOTDR pulse peak power was estimated to be below 10 mW, and was chosen as the highest possible power before the appearance of nonlinearities (mainly MI, which leads to a fast decrease of the visibility, as discussed in section 3.4). This way, the best performance along all points of the fibre is ensured. As expected, random oscillations are observed along the trace. The FUT was the same which was used to test first-order Raman amplification over 125 km (section 3.5) and it consisted of two fibre spools of 50 km and one fibre spool of 25 km of SMF-28, all linked by optical connectors. Due to a connector loss at ≈98 km (estimated as 3 dB), a decrease of the amplitude of the trace oscillations is observed at that point. The

vibrations were measured immediately after this connector loss, as it was clearly the worst sensitivity point along the fibre. Although better results could have been obtained if the fibre was spliced in this point (the amplitude drop of the trace oscillations would not occur), this loss was kept in order to provide a reliable comparison of the results using first- and second-order Raman amplification. And also to demonstrate that the system can detect vibrations over 125 km even under non-ideal conditions, as the vibrations were clearly measured. Another advantage of using second-order over first-order Raman amplification is clear, as the trace presents higher flatness along the fibre under similar measurement conditions (see Fig. 3.23b). This ensures the best performance as higher amplitude of the oscillations, and therefore higher SNR, is achieved at the lowest sensitivity point. The visibility of the ϕOTDR trace along the FUT (computed as $V=(T_{max}-T_{min})/(T_{max}+T_{min})$, where T_{max} and T_{min} are the maximum and minimum values of the trace over a window of 500 m) is presented in the top figure. Although the amplitude of the oscillations of the ϕOTDR trace varies along the FUT, the visibility remains close to 1 (even after the connector loss), i.e., the interference does not lose contrast along the propagation. In this case, the sensor is shown to perform reliable vibration measurements at any position along the FUT, if satisfatory vibration measurements are demonstrated at the position of worst signal level (after the connector loss, around km 98). For this reason, the vibration measurement tests were performed at this position.

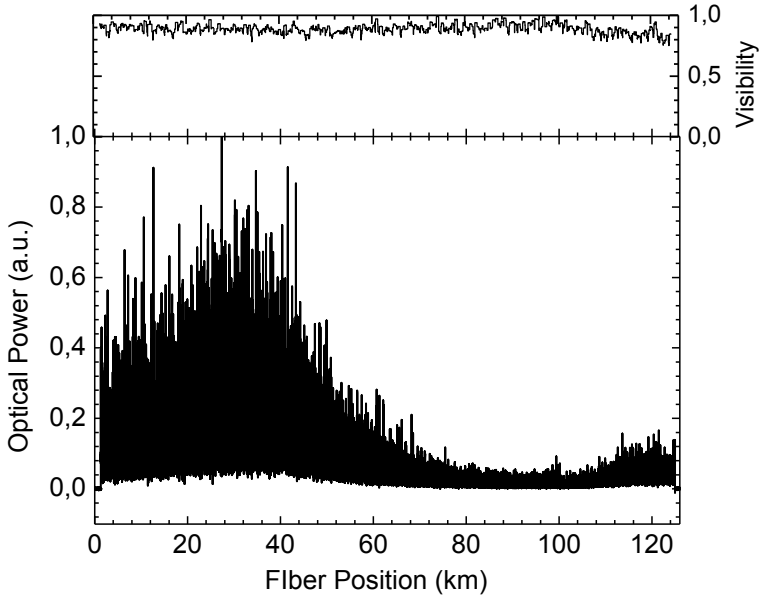

Fig. 3.29 ϕOTDR trace when the Raman pump power launched on each end of the FUT was 28.5 dBm. In this case, the ϕOTDR pulse power was chosen as the one ensuring the best performance. The top figure shows the visibility of the trace.

3.6.5 Vibration measurements

The procedure used to perform the vibration measurements was again similar to the one used in section 3.5.3.5, in order to provide a reliable comparison of the results using first- and second-order Raman amplification. The power evolution as a function of time for each point along the FUT was obtained by monitoring equivalent points in consecutive traces. The FFT of this power evolution will, therefore, present the frequencies measured at each point.

The sampling frequency of the sensor will be the ϕOTDR pulse repetition rate, which in this case was 781 Hz. Theoretically, this limits the maximum fibre span to be monitored to 131 km, and the maximum detectable frequency to 390 Hz (Nyquist frequency). As for the Raman and ϕOTDR pulse powers, they were the same as the ones used in Fig. 3.29.

As demonstrated in Fig. 3.29, the position of the worst signal level of the trace (lowest oscillations amplitude of the trace) was after the connector at km 98. Vibrations were applied to this point by placing the fibre inside a 2 m long PVC tube with 0.08 m of diameter, in which mechanical vibrations of controllable frequency were applied using a small vibration exciter with a maximum bare table acceleration of 736 ms^{-2} (with a 75 g mass attached). In order to avoid the propagation of vibrations outside the PVC tube, the fibre was clamped at its exits. Frequencies between 20 Hz and 380 Hz (nearly the theoretical maximum detectable by the sensor) were applied to the PVC tube and the FFT spectra of the optical power variation recorded by the ϕOTDR at this position are presented in Fig. 3.30. In this case, for the range of frequencies applied, the estimated displacement of the PVC tube was estimated to be in the sub-millimeter range. The sensor was able to successfully detect all the vibration frequencies applied, presenting peaks with amplitudes 6-10 times higher than the noise level in the rest of the spectrum of the FFT, i.e., a SNR of 8-10 dB. The presented sensor was therefore able to detect vibrations at higher frequencies and with a SNR improvement of ≈4-5 dB when compared to the case where first-order Raman amplification was used (see Fig. 3.26b), where vibrations of up to 250 Hz with a SNR of 3-6 dB were detected under similar measurement conditions.

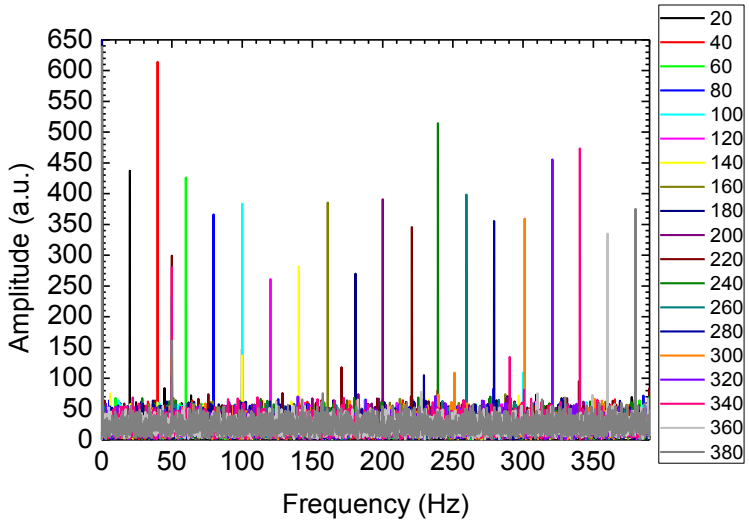

Fig. 3.30 FFT spectra of the optical power variation of the ϕOTDR signal along time at the point of the FUT with minimum signal, for applied frequencies between 20 Hz and 380 Hz, using the same conditions of Fig. 3.29.

The frequency of 50 Hz was also recorded in the vibration measurements due to the proximity of electrical instruments. It is important to notice that the presented data does not include any post-processing and, therefore, there is room for improvement of the performance of the sensor, if adequate signal processing is used for specific applications.

3.6.6 Spatial Resolution

Fig. 3.31 shows the normalized energy density of vibrations around 20 Hz (computed for each fibre position as the Root mean square (RMS) of the interval 18-22 Hz (signal) divided by the RMS of the interval 350-390 Hz (noise) of the FFT of the optical power variation of the ϕOTDR signal) along the FUT, when a vibration of 20 Hz was applied to the PVC tube (located at ≈98.8 km). At the points which are not affected by the vibration, the energy of the vibrations around 20 Hz is comparable to the energy of the noise, and the normalized vibration energy is ≈1. At the points affected by the vibration, however, the energy of the vibrations around 20 Hz is higher than the noise. In this case, the energy of the vibrations increased by more than 4 times at the points of the fibre where vibration was applied. The vibration was applied along 2 m of fibre and an increase of vibration energy was detected along 11 m of fibre (98865-98876 m). This means that the resolution, without any further processing, is ~10 m, as expected considering a ϕOTDR pulse width of 100 ns.

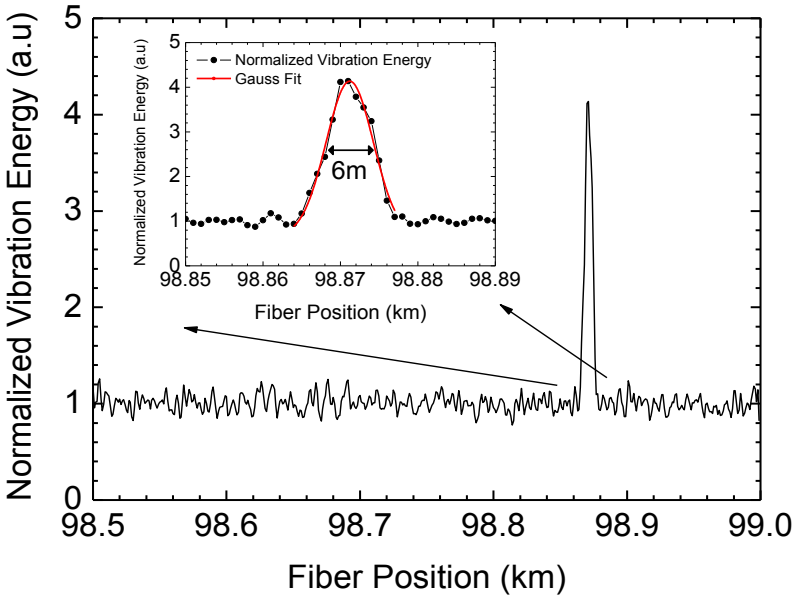

Fig. 3.31 Normalized energy density of vibrations around 20 Hz along the FUT when a vibration of 20 Hz was applied to the PVC tube (at ~98.8 km). In the figure inset a gaussian fit of the points where the vibration was detected is shown, presenting 6 m at FWHM.

3.6.7 Conclusions

To the best of our knowledge, a description of the use of a ϕOTDR assisted by second-order Raman amplification for distributed detection of vibrations is presented for the first time. Compared to the first-order Raman-assisted ϕOTDR (presented in the previous section), this scheme shows an enhanced SNR. This is due to the fact that the RIN introduced by the Raman amplification is mostly transferred to a lower frequency range, where the balanced detection implemented in the setup provides better suppression of the common-mode noise. Also, the ϕOTDR trace presented higher flatness and, therefore, higher amplitude of the oscillations at the lower sensitivity points. The sensor was able to measure vibrations of up to 380 Hz (limit set by the time of flight of light pulses) in a distance of 125 km, with a resolution of 10 m and an average SNR of 8 dB, without post-processing. This implies a >3 dB improvement in SNR over the first-order Raman-assisted setup with similar characteristics. As explained in the previous section, monitoring of intrusions over large structures, such as national borders, military bases or pipelines, are a few of the possible applications for this sensor.

3.7 ϕOTDR for distributed vibration sensing: Conclusions

In this chapter, an extensive investigation was presented on the use of ϕOTDR for distributed vibration sensing, which included theoretical and experimental descriptions of the signal and the noise for different configurations.

Over short fibre lengths, a simple ϕOTDR scheme without amplification allowed the detection of frequencies of up to 39.5 kHz over 1.25 km (section 3.3). The noise and signal statistics were characterized, showing good agreement with the theoretical model. Under normal operation, MI was identified as the limiting nonlinear effect on the performance of a ϕOTDR, leading to position-dependent fading (FPU recurrence) in the ϕOTDR trace when the pulse peak power is increased (section 3.4).

In order to extend the sensing range, the use of first-order (section 3.5) and second-order (section 3.6) Raman amplification to assist ϕOTDR operation were described and intercompared, and allowed distributed vibration sensing over more than 100 km. The RIN transfer from the Raman pumps was observed to be one of the main drawbacks of these schemes. However, the use of balanced detection was demonstrated to greatly reduce its impact on the detected signal. The scheme using ϕOTDR assisted by second-order Raman amplification was observed to perform better, allowing the detection of frequencies up to 380 Hz over 125 km.

In short, distributed vibration measurements up to frequencies in the limits set by the time of flight of light were achieved when using ϕOTDR over distances ranging from 1.25 km (section 3.3) to 125 km (section 3.6), while maintaining the simplicity of the schemes, as no post-processing, extremely high coherent lasers or coherent detection were required. To the best of our knowledge, the presented results include records in ϕOTDR distributed vibration sensing for the highest vibration frequency detected (39.5 kHz) and the highest sensing range (125 km) at the time of publication of ref. [3] and [5], respectively.

Schemes optimized for short fibre lengths (high frequency detection) could be used in vibration-based structural damage identification or monitoring, where ultrasonic waves are sometimes used to detect damages in the structures, while the schemes with amplification could be used for monitoring intrusions over large structures, such as national borders, military bases or pipelines.

4 ϕOTDR for distributed birefringence measurements

4.1 Introduction

After the description of ϕOTDR for dynamic measurements in chapter 3, in this chapter we focus in describing the use of ϕOTDR for static measurements. Distributed measurement of birefringence is achieved with a technique based on the correlation of ϕOTDR measurements using two orthogonal states of polarization. Owing to the nature of ϕOTDR, the potential for high accuracy (measurable variations in the refractive index difference between the two polarization axis (Δn) of ~10^{-7}) over large distances (10's of kilometers), and with metre resolution, is demonstrated. Distributed birefringence measurements were performed over PMF and low birefringence SMF.

4.2 State-of-the-Art

As discussed in section 2.2.3, in a birefringent medium, two modes with the same frequency and orthogonal linear polarizations experience different refractive indices and travel at different velocities. This will cause broadening of a pulse propagating in the fibre which can significantly distort optical signals, especially over long distances and at very high data rates.

In optical fibres, birefringence can occur due to several factors that introduce asymmetries in the fibre refractive index profile. With current manufacturing techniques, low birefringence can be achieved in SMF, being typically ~10^{-7}. As for PMFs, these are built by introducing asymmetries in the fabrication process (see Fig. 2.2) which lead to high built-in birefringence (e.g. ~10^{-4}), and can preserve the SOP along the fibre, thus making them very attractive for several applications.

While several techniques have been proposed to characterize the birefringence of fibres [115-121], most of them only measure the average birefringence and cannot be used to discriminate local birefringence variations along the fibre [115-118]. However, birefringence typically presents fluctuations along the fibre due to inhomogeneities resulting from the fibre drawing process, bendings and twists introduced during the cabling and installation processes, as well as due to external environmental conditions such as temperature and strain variations. High birefringence can occur in short fibre sections and become an important factor in the scaling of the overall PMD. The

distributed measurement of birefringence can, therefore, be an important tool for the characterization of fibres.

The techniques reported for distributed birefringence measurements are essentially based on OFDR [119, 120] and dynamic Brillouin gratings (DBG) [121]. While OFDR has been shown to allow very high spatial resolution, the sensing range is typically limited to a few hundreds of metres [120], which can be an important limitation when characterizing long fibres employed in optical communication systems. As for the DBG-based method, it relies on a complex system [121], where high power and precise adjustment of frequency and polarization of the three interacting optical waves is required to generate the gratings by stimulated Brillouin scattering (SBS) and read them in the transversal polarization. Furthermore, the mentioned techniques have only been described for measurement of birefringence along PMFs, which present much higher birefringence than SMFs.

Owing to their nature, ϕOTDR systems are typically focused on providing measurements at much longer distances (10's of kilometers) and have been demonstrated to allow high measurand resolution for static measurements (0.01ºC) over long distances (8 km) with one metre spatial resolution [27]. The discrimination of signals corresponding to different polarization axes has also been demonstrated in ϕOTDR operation [39], which makes it a suitable candidate for measurement of distributed birefringence.

4.3 ϕOTDR for static measurements: Theoretical model

The general principles (section 3.2.1), signal statistics and noise (section 3.3.2) of ϕOTDR operation have previously been described in the context of dynamic measurements. Here, we present a theoretical model and measurement principle for static measurements using ϕOTDR.

We start by recovering eq. 3.6, which describes the normalized optical intensity I detected at the fibre beginning (z=0), resulting from the interference of the fields reflected from M scattering centres, contained in a fibre section with length W/2 and centred at $\bar{z}$. The reflection results from the propagation of a ϕOTDR pulse (length W –

i.e., double the length of the fibre section, as discussed in section 3.2.1 - and frequency ω), and losses are neglected:

$$I(\bar{z}) = |E|^2 = |\sum_{m=1}^{M} r_m e^{i\phi_m}|^2 = \sum_{m=1}^{M} r_m^2 + 2\sum_{i=1}^{M-1}\sum_{j=i+1}^{M} r_i r_j \cos(\phi_i - \phi_j), \quad (4.1)$$

where $r_m \in [0,1]$ (usually <<1; $\sum_{m=1}^{M}|r_m| << 1$) and $\phi_m \in [0, 2\pi]$ are the reflectivity and phase of the wave reflected from the m^{th} scattering centre. Considering a one dimensional model, then $\phi_i - \phi_j$ for two scattering centres *i*, *j*, placed at the positions z_i, z_j, will be written as

$$\phi_i - \phi_j = \omega\left[\frac{n \cdot 2(z_i - z_j)}{c}\right], \quad (4.2)$$

where *n* is the local refractive index at $z=[z_i ; z_j]$. In this case, the interference pattern $I(z)$ along the fibre will be dependent on ω, *n* and the position of the scattering centres z_m. The core concept of using ϕOTDR for static measurements relies on the principle that changes in *n* (and z_m) can be compensated by changes in ω. Then, the pattern $I(z)$ which results from using ω for a given *n* (and z_m) will be similar to $I(z)$ produced by using $\omega+\Delta\omega$ for another *n*' (and z_m'). By measuring the $\Delta\omega$ shift that compensates the *n* (and z_m) changes induced by temperature/strain applied to the fibre, the refractive index change can be measured with much higher resolution than those provided by Brillouin based sensing [122]: temperature/spatial resolutions of 0.01ºC/1 m have been demonstrated over 8 km using ϕOTDR [27]. Reported sensitivities to changes in temperature ΔT and strain $\Delta\varepsilon$ (for a central wavelength ~1550 nm) are [123],[27]:

$$\frac{\Delta\omega}{\omega} \approx -6.92 \cdot 10^{-6} \Delta T \quad (4.3)$$

$$\frac{\Delta\omega}{\omega} \approx -0.78 \cdot \Delta\varepsilon . \quad (4.4)$$

The standard procedure for static measurements is to perform ϕOTDR measurements while changing ω step by step and record the pattern $I(z)$ for each ω [$I(z, \omega)$], at a given time t_1. The measurement is then repeated at a different time t_2, and the cross-correlation between the two measurement sets is computed for each z. If changes in *n* do not occur between t_1 and t_2, then the maximum of the cross-correlation will occur for $\Delta\omega$=0. However, if a change Δn occurs, then the maximum of the cross-correlation will occur

for $\Delta\omega \neq 0$. A full mathematical description of the procedure can be found in [27]. Since $I(\bar{z})$ is only sensitive to local changes in n around $\bar{z}$ (within a length $W/2$), then the distributed measurement of variations in n can be performed along the fibre.

For each frequency step, the measurement is performed similarly to the dynamic ϕOTDR measurements. For this reason, all the considerations for noise and system stability (pulse coherence, laser stability and polarization noise) made in chapter 3 also apply to the case of static measurements. However, for static measurements, the comparison between ϕOTDR traces, which can be several minutes apart (depending on the number of frequency steps and averaging), is required. In this case, the long-term frequency stability of the laser plays a critical role, since a frequency drift $\Delta\omega$ of the laser will be indistinguishable from an actual change in n. Schemes using a laser with locked operating frequency, where the frequency of the ϕOTDR pulses is scanned using an electro-optic modulator (EOM), are therefore usually adopted [124]. Since the bandwidth is no longer a critical parameter, averaging of ϕOTDR traces is also typically used to reduce the fluctuations of the pattern $I(z)$ and improve the SNR.

If the induced $\Delta\omega$ is higher than the frequency range that is scanned, then the cross-correlation will show no peak and the measurement is inconclusive. In this case, a practical problem for ϕOTDR sensors can arise from their high sensitivity: the scan of a high frequency range (~GHz per ºC, for a central wavelength ~1550 nm) may be necessary to monitor modest temperature/strain changes.

4.3.1 Birefringence measurements

In order to perform birefringence measurements, the main difference, with respect to conventional ϕOTDR used for static measurements, is that the two measurements are performed at orthogonal states of polarization. Since birefringence is translated into a refractive index difference $\Delta n = n_s - n_f$ between the slow (n_s) and fast (n_f) polarization axes, then, from eq. 4.2, the expected cross-correlation peak shift $\Delta\omega = \omega_s - \omega_f$, between the measurements of the two axes can be derived as

$$n_s(\omega_s)\cdot\omega_s = n_f(\omega_f)\cdot\omega_f \Leftrightarrow -\frac{\Delta\omega}{\omega_s} = \frac{\Delta n}{n_f}. \tag{4.5}$$

If the two measurements are performed in the same polarization axis, then the cross-correlation peak shift is expected to be $\Delta\omega = 0$, since $\Delta n = 0$. In practice, this

correlation peak provides a measurement of the averaged laser frequency drift, as well as of the fluctuations of the fibre temperature during the acquisition time [27]. Since these effects can significantly impact on the accuracy of the frequency measurements, measuring the peak at $\Delta\omega=0$ provides a reliable method to evaluate the stability of the system, and to compensate for undesired cross-sensitivities.

4.4 Experimental Work

4.4.1 Setup

The experimental ϕOTDR setup (using polarized light) which was used for local phase birefringence measurements is shown in Fig. 4.1. A distributed-feedback (DFB) laser, operating at 1535 nm, and a semiconductor optical amplifier (SOA) are used to generate optical pulses with high extinction ratio (ER). The pulse width is set to 20 ns, corresponding to a spatial resolution of 2 m. While the laser temperature is tuned to coarsely scan the optical frequency of the pulses in a wide frequency range (many 10's of GHz), an electro-optic modulator (EOM), driven by a microwave source, is used to accurately scan the light frequency with steps of 10 MHz. A tuneable 10 GHz fibre Bragg grating (FBG) is utilized to select one of the sidebands generated by the EOM. Then, optical pulses are amplified by an Erbium-doped fibre amplifier (EDFA), followed by a tuneable optical filter (TOF) used to suppress the amplified spontaneous emission (ASE) noise. Before launching the pulses into the fibre under test (FUT) using a circulator, a polarization switch (PSw) and a polarization controller (PC) are used to launch light into the FUT with orthogonal states of polarization. Three different FUTs were evaluated: two PMFs (an 80 m Panda and a 100 m elliptical-core fibre) and one SMF (3 km). A polarizer followed by a power metre are placed at the output of the FUT. By monitoring the transmitted power at the power metre and maximizing/minimizing it, a maximum coupling of light into the slow/fast axis (in this case, the polarizer is aligned with the slow axis of the PMF) is ensured. With this procedure, the correlation peak amplitude is enhanced, thus improving the accuracy of the frequency measurements. At the receiver, the Rayleigh backscattered signals are sent to a 125 MHz bandwidth photodetector, and then acquired by a computer. Finally, the birefringence is computed based on the frequency shift of the peak of the cross-correlation between ϕOTDR measurements using pulses with orthogonal states of polarization, as discussed in section 4.3.1.

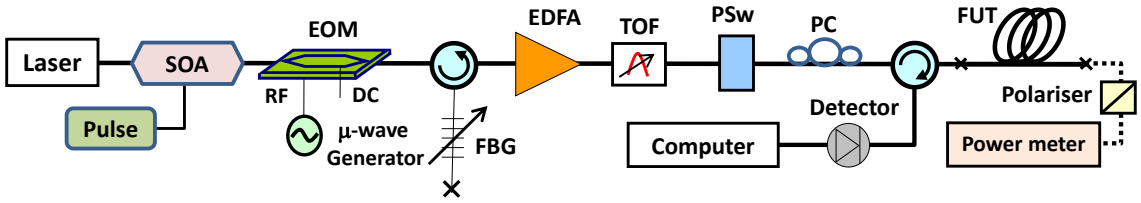

Fig. 4.1 Experimental setup of the ϕOTDR used for distributed birefringence measurements.

4.4.2 Birefringence of PMFs

We start by describing the birefringence measurements performed in the PMFs, using the setup described in Fig. 4.1. Fig. 4.2 shows the birefringence-induced frequency shift ($\Delta\upsilon = \Delta\omega/2\pi$) along the FUT, obtained from the cross-correlation of ϕOTDR measurements at the two orthogonal states of polarization for the Panda (Fig. 4.2a) and the elliptic-core (Fig. 4.2b) fibres. From $\Delta\upsilon$, the profile of the modal birefringence Δn (defined in eq. 2.14) along the fibre is computed (using eq. 4.5), and is presented in the right-hand side vertical axis. The average value of Δn was $\approx 56.2 \cdot 10^{-5}$ for the Panda fibre (Fig. 4.2a) and $\approx 32.6 \cdot 10^{-5}$ for the elliptic-core fibre (Fig. 4.2b). Fluctuations of Δn of the order of $\sim 0.1 \cdot 10^{-5}$ were clearly observed along both fibres.

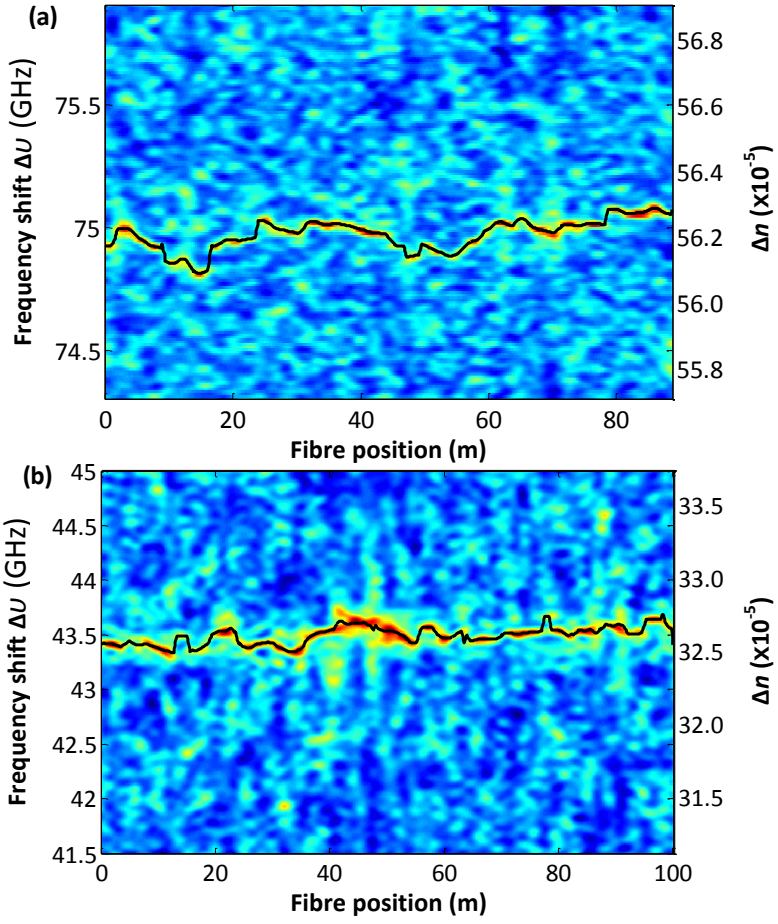

Fig. 4.2 Distributed profile of phase birefringence versus distance along a) 80 m Panda PMF and b) 100 m elliptical-core PMF.

4.4.3 Birefringence of SMFs

After characterizing the PMFs, the setup described in Fig. 4.1 was then used to perform distributed birefringence measurements along a 3 km standard SMF. The fibre corresponds to an old SMF drawn in the mid 80's, and therefore non-uniformities and larger birefringence values are expected with comparison to more recent SMFs. In this case, the fibre does not have clearly defined polarization axis, and therefore there is no polarization adjustment to be made. However, the measurement in two orthogonal states of polarization are still essential to ensure that no correlation fading impairs the measurements along the fibre.

Since SMFs are characterized by very low birefringence (are therefore small induced shift $\Delta\nu$), the measurement accuracy has to be highly controlled. For this reason, the laser frequency was locked on an absorption line of a gas cell, corresponding to a hollow-core photonic crystal fibre (PCF) filled with acetylene gas at 5 mbars. A lock-in amplifier was used in a feedback system that provides injection current corrections to the laser driver, thus compensating for the laser frequency drifts. Also, the frequency scan was performed, in this case, by scanning only the microwave frequency driver of the EOM in a range of 3 GHz.

Fig. 4.3a shows the measured birefringence-induced $\Delta\nu$ and the respective Δn profile along the SMF. Since the polarization of the ϕOTDR pulses is not aligned with any particular axis, it is expected that each ϕOTDR measurement contains a superposition of light reflected from both polarization axes. In this case, the cross-correlation spectrum between orthogonal ϕOTDR measurements should present three peaks: one at 0, and two other symmetrically placed at $\pm\Delta\nu$. The local amplitude of these peaks should also be dependent on the ratio of light coupled into the slow/fast axis at each fibre location. The birefringence measurement confirmed the presence of these three peaks, and it was observed that Δn was $\approx 0.3 \cdot 10^{-5}$ at the fibre beginning and then decreased to very close to 0 after 2000 m, although three peaks were still distinguishable. It is interesting to notice that despite the low values of birefringence, the variations of Δn were again measured precisely along the entire fibre length.

A section of the cross-correlation spectrum (at the fibre position 220 m) is shown in Fig. 4.3b. Here, the profile of three peaks, one centred at zero and the other two at ±300 MHz, is clearly depicted. The best measurable birefringence is ultimately limited

by the width of the correlation peaks, which is observed to be ≈50 MHz. This is consistent with the spectral width defined by the 20 ns pulses, and corresponds to a measurable birefringence of $\Delta n \sim 3 \cdot 10^{-7}$.

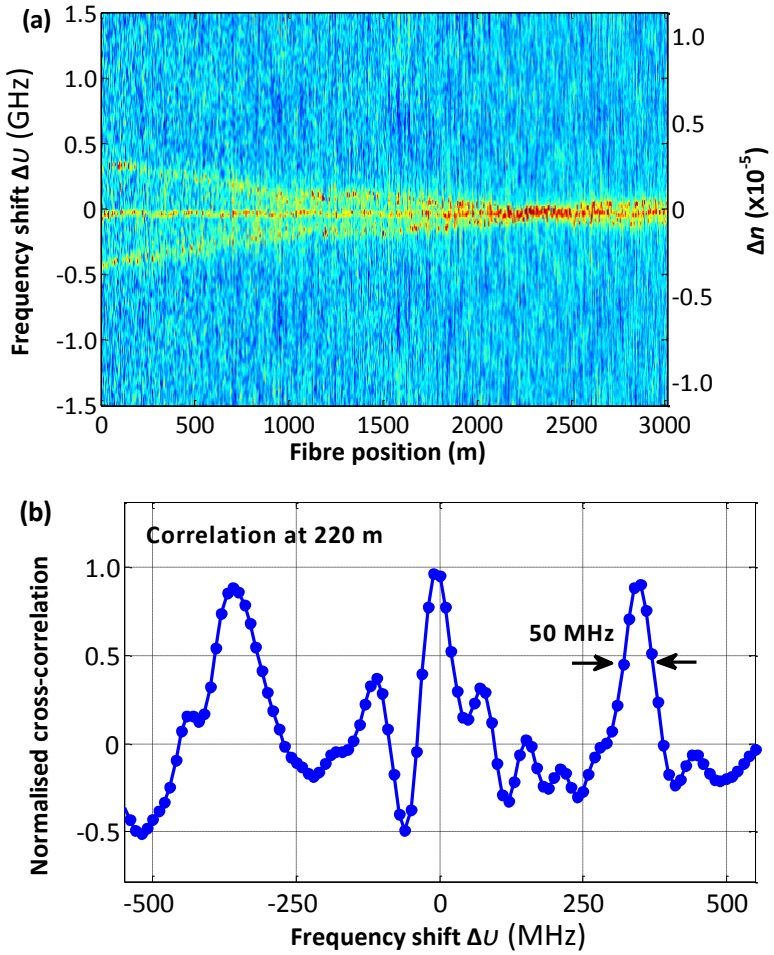

Fig. 4.3 Distributed birefringence measurement in a SMF: a) Measured frequency and birefringence profile versus distance b) cross-correlation spectrum at 220 m distance.

4.5 Conclusions

To the best of our knowledge, distributed measurement of birefringence using ϕOTDR has been presented for the first time. The technique uses the correlation of ϕOTDR measurements at two orthogonal states of polarization. Owing to the high birefringence accuracy achieved ($\Delta n \sim 10^{-7}$), the discrimination of local birefringence changes was clearly demonstrated along not only PMFs, but also along low birefringence SMF. The potential for metre spatial resolutions over several km was also demonstrated.

A potential drawback to the technique is that it requires a comparison between ϕOTDR traces which can be several minutes apart. However, by using unpolarized light and

correlating the measured frequency sweep with itself, it may be possible to perform measurements with a single frequency sweep, thus increasing the stability of the system.

5 URFL for remote vibration sensing

5.1 Introduction

In the present chapter, a new configuration for an intensity vibration sensor based on a Raman fibre laser is proposed. The linear cavity of the Raman fibre laser relies on the combination of a distributed Rayleigh mirror and FBGs, which are used as the sensing element and intensity filter. The main advantages of the proposed configuration are the simple high SNR scheme for remote sensing, and the possibility of easy multiplexing. The main results presented in this chapter were published in Journal of Lightwave Technology [4].

5.2 State-of-the-Art

Raman FBG lasers using a linear cavity have been widely researched and improved over the last two decades [125]. Recently, ultralong Raman fibre lasers (URFL) have been implemented as very attractive solutions for optical communication links [126]. Although fibre lasers based on the Raman effect can present some restrictions when high power is injected in the fibre due to the gain suppression created by the Rayleigh scattering growth, systems where power losses are continuously compensated using second-order Raman pumping, creating virtually lossless fibre spans, have been demonstrated [22]. The principle was used to demonstrate a resolvable mode structure of an URFL with a 270 km cavity in 2009 [55]. Rayleigh scattering can also be used as a distributed random mirror to enhance the generation of Brillouin-Raman comb lasers [127-130], multiwavelength generation [131, 132] and random distributed lasers [133]. In 2010, a 200 km dual-wavelength URFL using two FBGs with different Bragg wavelengths, one on each side of the fibre span, was reported [134]. The laser cavities of the two independent Raman fibre lasers were formed between the FBGs and a distributed random mirror created by Rayleigh scattering, resulting in laser action at the wavelength of the FBG peak.

In optical sensing, several sensors combining the use of FBGs with Rayleigh scattering have been reported. FBGs can be used as sensing heads for measurement of strain, temperature or other physical parameters, since the variation of these parameters induces changes on the central Bragg wavelength [135, 136]. Recently, a temperature-insensitive strain sensor using two different wavelength Raman FBG lasers, which used cooperative Rayleigh scattering, was reported [137]. The use of

Raman fibre lasers also allows for remote optical sensing. Recently, a 300 km URFL (with cooperative Rayleigh scattering) using a distributed mirror was reported for sensing applications [58]. Also, a new method to extend the range of BOTDA systems for up to 100 km with sub-meter resolution was reported [72]. The work exploits the virtual transparency created by second-order Raman pumping in optical fibres.

Conventional vibration sensors, based on capacitive or piezoelectric principles, can present performance limitations due to the problem of electrical isolation, especially in the presence of high-voltages and high magnetic fields [138, 139]. Optical fibre sensors, however, present several characteristics that make them particularly attractive when compared to traditional sensors, such as inherent immunity to electromagnetic interference, small size, possibility of remote operation and multiplexing capability. Furthermore, the fibre can be used as both the sensing element and the communication channel [140, 141].

A distinction can be made between passive FBG-based and active laser-based optical fibre sensor systems. Passive FBG-based sensors rely on the simple reflection of light coming from a spectrally broadband source. In this case, the optical power of the signal to be detected is rather low as the FBGs present narrowband reflection spectra and no amplification occurs, which results in low SNR. In the case of active laser-based sensors, however, the signal is amplified in the optical domain before being detected, rather than in the electronic domain after detection, which leads to significant improvement in the SNR, especially in the presence of high background noise [142]. An improvement of up to 40 dB in the amplitude and 20 dB in the SNR of the detected vibrations between active (laser-based sensor) and passive devices (illuminating FBGs with a broadband source) under similar conditions has been demonstrated [136]. For remote sensing, considering the typical SMF losses, an increase of 40 dB in the amplitude of the signal would allow the sensing range to be increased by ~100 km.

5.3 Experimental Work

Fig. 5.1 presents the configuration of the Raman FBG laser intensity vibration sensor. The gain in this configuration is provided by a 1455 nm Raman pump laser with a maximum power of 5 W, which creates a typical broadband Raman gain in the dispersion compensating fibre (DCF) with a maximum around 1555 nm (13.1 THz

above the pump laser frequency). Two WDMs (1450/1550 nm) and a 1 km DCF with a dispersion coefficient of -132 ps nm^{-1} km^{-1} are used. In this configuration, a laser cavity is formed between two FBGs, which are also used as the sensing head and intensity filter. The process is assisted by a distributed mirror created by Rayleigh scattering in the DCF.

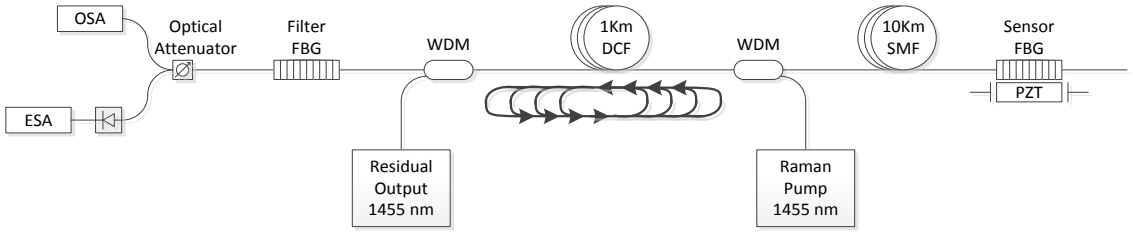

Fig. 5.1 Experimental Setup of the Raman FBG laser intensity vibration sensor.

The sensing head is the sensor FBG, which is connected to the rest of the setup by 10 km of SMF-28, to simulate a remote sensing configuration. In order to characterize the sensor FBG as a vibration sensor, it is attached to a PZT which vibrates at a frequency of up to 1 kHz due to an applied signal voltage generated by an electric modulator. The filter FBG is used as the intensity filter to interrogate the vibration applied to the sensor. In this case, the reflection spectra of the filter FBG and the sensor FBG are tuned to be partially overlapped. By properly tuning the Raman pump power, lasing can be set to occur only when the overlap of the reflection spectra of both FBGs occurs. Due to the wavelength shift of the reflection spectrum of the sensor FBG induced by deformations (simulated by the PZT), the overlap of the reflection spectra of both FBGs will be larger when negative wavelength shifts are applied. The resulting laser spectrum will therefore have higher optical power and lower wavelength peak than when positive wavelength shifts are applied.

Finally, in order to monitor the optical power of the laser output, a photodetector was used to convert the laser output optic signal into an electrical signal which was then observed by an ESA. Also, in parallel, an OSA with a maximum resolution of 0.05 nm was used to observe the laser output optical spectrum.

The optical power output as a function of the Raman power input of the Raman FBG laser was characterized without the filter FBG (Fig. 5.2). The threshold was observed to occur at 350 mW, and a linear regime was observed in the range of 700-1000 mW with a laser slope efficiency of 1.49±0.05 %. The figure inset presents the output spectrum for the input Raman pump powers of 600 mW and 800 mW. For higher pump powers,

the central wavelength of the laser was shifted to higher wavelengths and the efficiency increased due to the Raman gain profile, which has a maximum at 1555 nm.

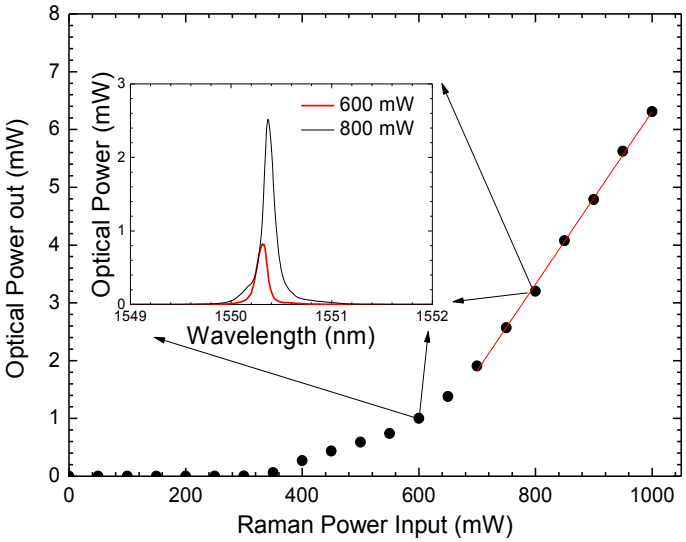

Fig. 5.2 Optical power output as a function of the Raman power input of the Raman FBG laser without the filter FBG (Figure inset: output spectra for the input Raman pump powers of 600 mW and 800 mW).

Using the experimental setup presented in Fig. 5.1, the output optical spectrum was observed when the maximum (15 V) and minimum (-15 V) voltages were applied to the PZT (Fig. 5.3). As expected, for the minimum applied voltage, the output spectrum presented a higher optical power since the overlap of the reflection spectra of the FBGs was higher and the peak was placed at a lower wavelength. The inset of Fig. 5.3 presents the reflection spectra of both FBGs, which were measured with a FBG interrogator. The filter FBG presents a typical 100 % saturated FBG reflection spectrum, with 0.23 nm FWHM and centred at 1549.98 nm, which drops 19 dB between 1550.07 nm and 1550.17 nm. As for the sensor FBG, it presents a 60 % reflectivity and is centred at 1550.13 nm for the minimum applied voltage on the PZT (-15 V), and at 1550.17 nm for the maximum applied voltage (15 V). The sensor FBG has a 0.13 nm FWHM and drops 11 dB between the centre wavelength and 1 nm away from the centre.

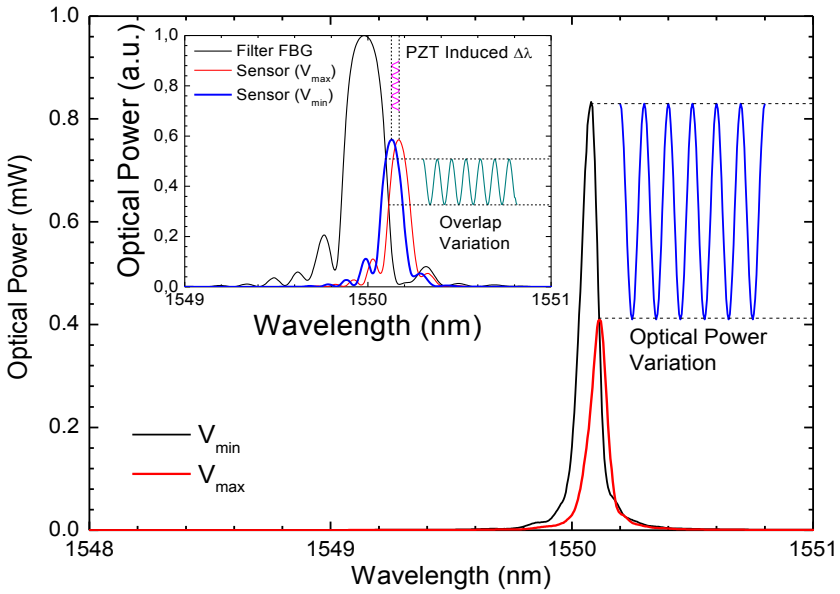

Fig. 5.3 Optical output spectra for maximum and minimum applied strain to the sensing head (FigureiInset: reflection spectra of the filter FBG and sensor FBG for maximum and minimum applied strain to the sensing head).

A sinusoidal electric signal with 30 Vpp (varying between -15 V and 15 V) was applied to the PZT, and the output optical power was observed in the time domain for the frequencies of 50 Hz, 100 Hz and 260 Hz (Fig. 5.4). A sinusoidal variation was observed, as expected, with an amplitude that was observed to decrease with the frequency. Amplitudes of 6.5 dB for 50 Hz, 5.2 dB for 100 Hz and 3.5 dB for 260 Hz were observed, and all spectra had a maximum optical power close to 0 dBm. The optical response was not perfectly sinusoidal due to insufficient pre-tension applied to the sensor FBG during the attachment to the PZT.

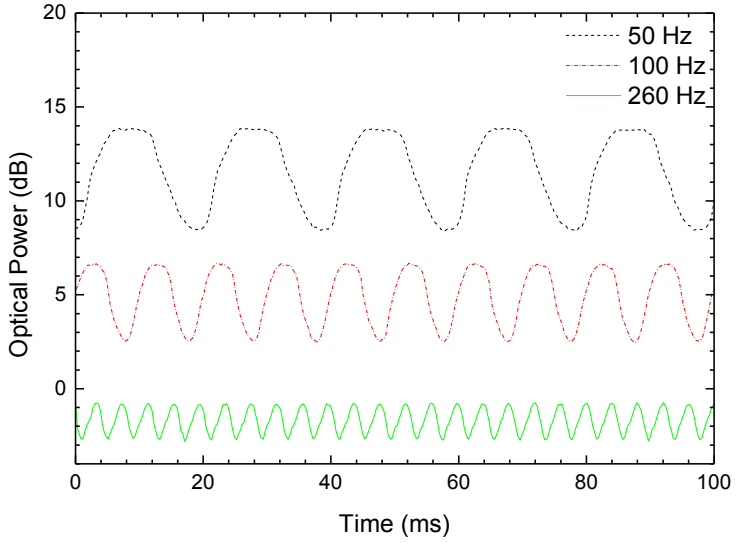

Fig. 5.4 Output optical power variation of the laser in the time domain for applied vibrations of different frequencies (arbitrary optical power reference level).

With the same electrical signal applied to the PZT, the optical power output signal was converted to an electrical signal. This signal was characterized in the spectral domain, and the amplitude of the central frequency was measured as a function of the frequency applied to the PZT (Fig. 5.5). The amplitude of the central frequency was observed to decrease with the applied frequency, decreasing 3 dB (with respect to the lower frequencies) at 200 Hz and showing a steep decrease above 240 Hz. The SNR of the spectra, for applied frequencies below 260 Hz, was higher than 50 dB and a well-defined frequency peak was observed for applied frequencies of up to 340 Hz, with a 22 dB SNR. The inset of Fig. 5.5 presents the output power in the frequency domain for the cases of applied frequencies of 100 Hz and 260 Hz. Higher order harmonics (due to insufficient pre-tension of the FBG, resulting in the clipped sinusoids of Fig. 5.4) are clearly observed for the case of 100 Hz (at 200 Hz and 300 Hz), but with lower amplitudes than that of the applied frequency. A 1/f noise was observed with an average power varying between -65 dBV_{rms} for frequencies near 0 Hz, and -70 dBV_{rms} for frequencies near 400 Hz.

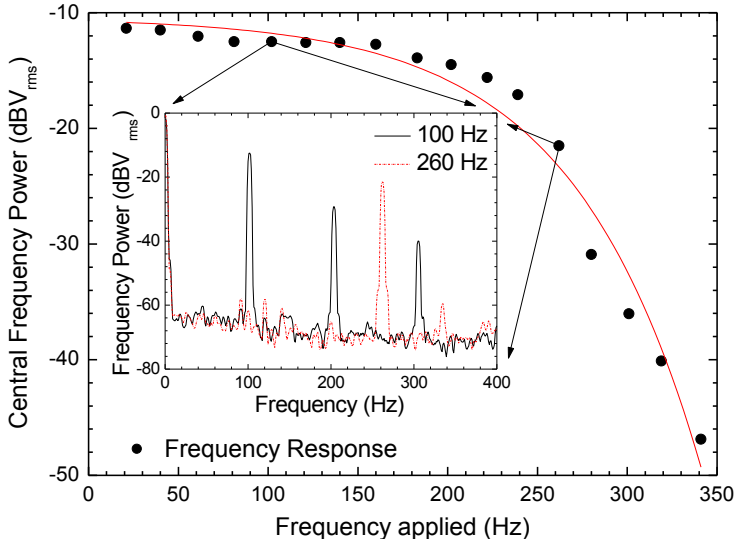

Fig. 5.5 Central frequency output power (converted electric signal) for applied vibrations of different frequencies (Figure inset: output power in the frequency domain for 100 Hz and 260 Hz).

The amplitude of the central frequency of the output spectrum was measured as a function of the maximum strain variation applied to the fibre (proportional to the maximum amplitude of the signal applied to the PZT), at a constant applied frequency (Fig. 5.6). Considering a perfect sinusoidal movement, the maximum acceleration will be given by: $Max_{acceleration} = Max_{strain} \cdot L_{FBG} \cdot (2\pi f)^2$, where f is the frequency of the movement and L_{FBG} is the sensor FBG length (≈1 cm). A response with a sensitivity of

0.57±0.07 dB/με (2.3±0.3·10^{13} dB/(ms^{-2})) for an applied frequency of 100 Hz, and of 0.57±0.05 dB/με (1.5±0.1·10^{14} dB/(ms^{-2})) for an applied frequency of 260 Hz was obtained.

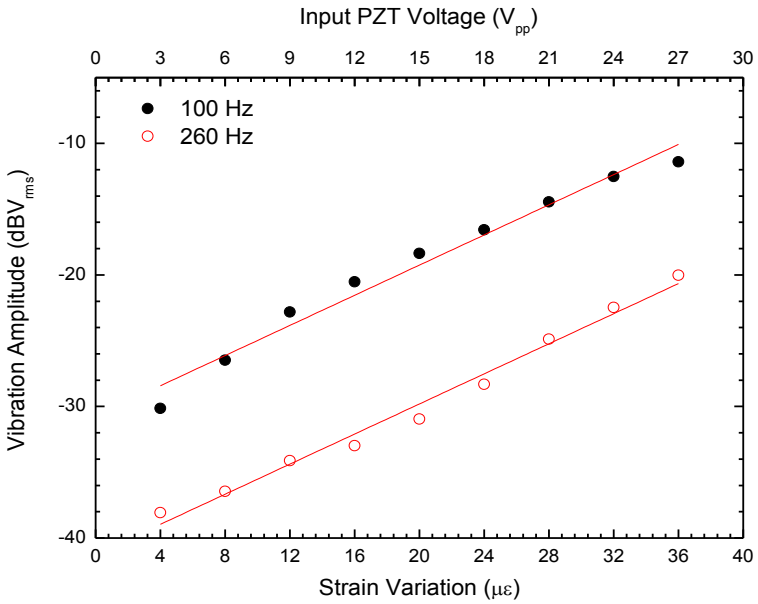

Fig. 5.6 Amplitude of the vibration as a function of the maximum strain variation (induced by applying an electrical signal to the PZT).

5.4 Discussion

In the presented intensity vibration sensor, the output power variation is due to the difference of overlap of the reflection spectra of the FBGs, which creates a laser spectrum with a different power. When the overlap of the reflection spectra of the FBGs is larger (sensor FBG shifted to lower wavelengths), the output power is higher, even though the peak of the laser is placed at a wavelength with lower Raman gain (which increases with wavelength in the region where the FBGs are placed, having a peak at 1555 nm). However, a higher power variation would be expected if the Raman gain was lower for higher wavelengths.

The fact that lasing occurs under the FBGs control provides a high SNR, and also means that the output optical power to be measured will be higher than with other schemes relying on simply measuring the optical power reflected by FBG. The sensor was able to measure frequencies of up to 350 Hz, being limited by the PZT response, which had a resonance near that frequency. However, considering the laser cavity length (~10^{-4}s for a light whole round-trip), measurements above 1 kHz are not to be expected. As for remote sensing, 10 km were demonstrated, but considering the power and SNR

of the output signal, no problems are envisaged for distances of up to 100 km, although a maximum detectable frequency bandwidth decrease would be expected.

Temperature variations in the sensing head will shift the reflection spectra of the sensor FBG and could, in principle, interfere with the vibration measurement. In a typical case, however, the temperature variations will be much slower than the strain variations of the vibration to be detected. Therefore, the temperature variations will not affect the vibration measurements, if the temperature difference between the two FBGs is not too high (~20ºC), in which case the reflection spectra of the FBGs would no longer overlap and vibration measurements would no longer be possible.

5.5 Conclusions

To our knowledge, the use of a Raman FBG laser for an intensity vibration sensor is reported for the first time. When vibrations were applied to the sensing head, a sinusoidal variation of the output power of the Raman fibre laser was observed with maximum optical output power of 0 dBm and maximum amplitude of 6.5 dB. The sensor was able to measure vibrations with frequencies of up to 350 Hz and also the amplitude of the vibrations with a sensitivity of up to 0.57 ± 0.07 dB/με ($2.3\pm0.3\cdot10^{13}$ dB/(ms^{-2}) for 100 Hz), for vibrations with a maximum strain variation of up to 35 με (maximum acceleration of up to $9\cdot10^{-13}$ ms^{-2} for 100 Hz). The frequency spectra were observed to have a SNR higher than 50 dBV$_{rms}$ for frequencies below 250 Hz. Remote sensing at a distance of 10 km was simulated, but no problems are envisaged for distances up to 100 km, although a maximum detectable frequency bandwidth decrease would be expected.

The presented configuration allows for low cost interrogation of vibrations since the measurand is an optical power variation, and high SNRs are achieved. The performance of the sensor could be improved by using higher quality FBGs and a different Raman gain profile.

6 Other Contributions

During the PhD programme, the author was involved in parallel projects which were not directly connected to the main theme of the thesis. As a product of these parallel projects, two additional researches (each one resulting in a publication in an international journal) are presented in this chapter.

6.1 Intensity curvature sensor based on a photonic crystal fibre with three coupled cores

6.1.1 Introduction

In the present chapter, an intensity curvature sensor using a Photonic Crystal fibre (PCF) with three coupled cores is proposed. The three cores are aligned and there is an air hole between each pair of adjacent cores. The fibre has a low air filling fraction, which means that the cores remain coupled in the wavelength region studied. Due to this coupling, interference is obtained in the fibre output even if just a single core is illuminated. A configuration using reflection interrogation, which used a fibre section with 0.13 m as the sensing head, was characterized for curvature sensing. When the fibre is bent along the plane of the cores, one of the lateral cores will be stretched and the other one compressed. This changes the coupling coefficient between the three cores, changing the output optical power intensity. The advantage of this sensing head is the simple interrogation technique based on optical power variation. The main results presented in this chapter were published in Optics Communications [1].

State-of-the-Art

In recent years, PCFs have been widely used both in research and in industry. Recent reports have demonstrated the possibility of using multicore PCFs for several applications, such as light couplers [143-146], narrow band filters [147, 148], frequency comb generators based on FWM [149], supercontinuum generation [150], phase-locking [151] and fibre lasers [152].

Experimental studies comparing the properties of light propagation in a PCF with a number of cores up to eighteen, for high power applications, have been presented [153]. Theoretical models have also been presented to describe the supermode characteristics for linearly and circularly distributed multicores in PCFs [154], and the dependence of

the characteristics of these modes on the geometry of the fibre [155]. PCFs have also been used for sensing applications [156], such as of biomolecules [157], as force metres [158], and as pressure [159], torsion [160], strain [161], temperature [162] and curvature sensors [163].

In the case of curvature sensors, three measurands can be used to interrogate the sensor, namely, the phase shift [163], bending loss [164] or wavelength separation [165]. With the use of FBGs written into separate cores of multicore PCFs, sensors with temperature insensitivity for one-axis [165] and two-axis [166] curvature measurement have been demonstrated. The sensors make use of the different strains applied to different cores when curvature is forced on the fibre to induce different shifts in the wavelengths of the FBGs. The same principle has also been demonstrated in Gemini fibres [167].

An intensity curvature sensor was demonstrated to measure curvature with a sensitivity of 2.16±0.02 dB/m^{-1} in a range of 3.5 m^{-1}, using a long-period fibre grating monitored by an optical time-domain reflectometer [168]. For shorter measuring ranges, higher sensitivities have been achieved. Using a fibre-optic curvature sensor based on the single-mode-multimode-single-mode (SMS) fibre structure, a sensitivity of -18.42 dB/m^{-1} for a range of 0.54 m, and a sensitivity of -130.37 dB/m^{-1} for a range of 0.23 m^{-1}, were demonstrated [169].

6.1.2 Experimental Work

Fig. 6.1 presents the configuration of the curvature sensor. The configuration uses a broadband source, at 1550 nm with 100 nm bandwidth, and an OSA, with a maximum resolution of 0.05 nm, which was used to observe the output optical spectrum. A PCF with 0.13 m length, three aligned cores and a low air filling fraction, is used as the sensing element.

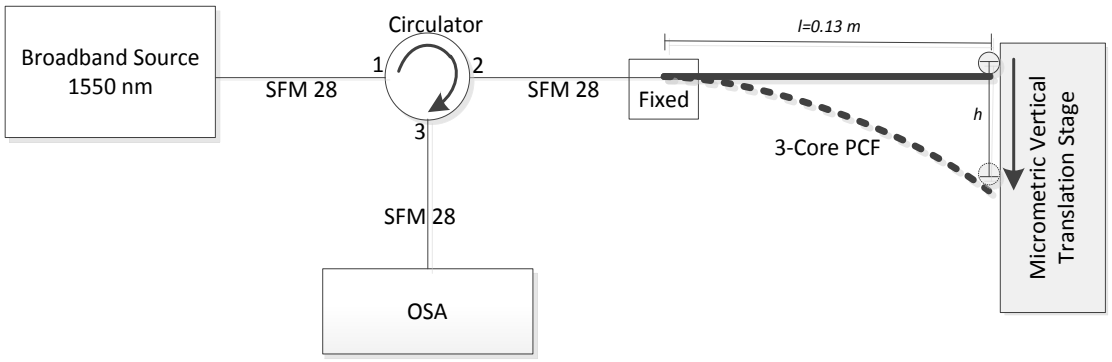

Fig. 6.1 Experimental setup of the bending sensor based on a PCF with three coupled cores.

The average pitch of the air hole (Λ) of the PCF, i.e. the distance between two consecutive holes, is (2.17±0.02) μm, the average diameter of the air holes (d) is (0.9±0.1) μm and the fibre has a total of 88 air holes (N_{AH}). The relative hole diameter $\frac{d}{\Lambda}$ is 0.41±0.05 and the parameter $\frac{\lambda}{\Lambda}$ is 0.71±0.02 (considering a bandwidth of 100 nm). The diameter of the guiding cores is (3.6±0.1) μm, the size of the air hole cladding structure is (22.5±0.1) μm, and the diameter of the cladding is 184 μm. A transversal cross-area section of the PCF geometry is presented in Fig. 6.2.

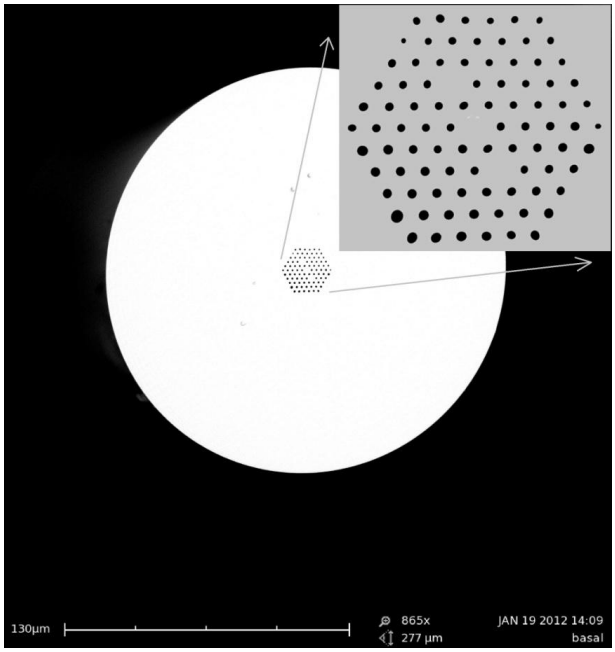

Fig. 6.2 Cross-section of the PCF with three cores with a magnification of 865x (inset figure with a magnification of 9000x).

One end of the PCF is spliced to the SMF-28 and the other end is free. The core of the SMF is aligned with the central core of the PCF so that coupling between the SMF and the side cores of the PCF is low. In order to enable real applications using PCF, it is essential to have low loss splices with standard SMFs. Although the different coefficients of thermal expansion and melting temperatures of the two fibres make splicing difficult, low-loss splices have been demonstrated between SMF-28 and PCFs fibres [170].

The light sent by the light source is reflected from the cleaved free end of the PCF by Fresnel reflection (4 %), and is deflected in the circulator to the OSA. In this case, the output signal is observed in reflection and the effective optical path in the PCF is twice

its physical length. The curvature of the PCF is applied by vertically moving the micrometric translation stage. A good approximation for the curvature *C* is given by

$$C = \frac{1}{R} = \left(\frac{2h}{l^2 + h^2}\right), \tag{6.1}$$

where *R* is the curvature radius, *h* is the height difference between the fixed end and the free end of the PCF, and *l* is the horizontal distance between the fixed end of the PCF and the micrometric translation stage.

Using the setup described in Fig. 6.1, curvature was applied to the PCF. The spectral response of the peak of the output spectrum which presented the highest stability and optical power for different applied curvatures is presented in Fig. 6.3. Although the form of the spectrum remains similar, the average optical power decreases for higher applied curvature.

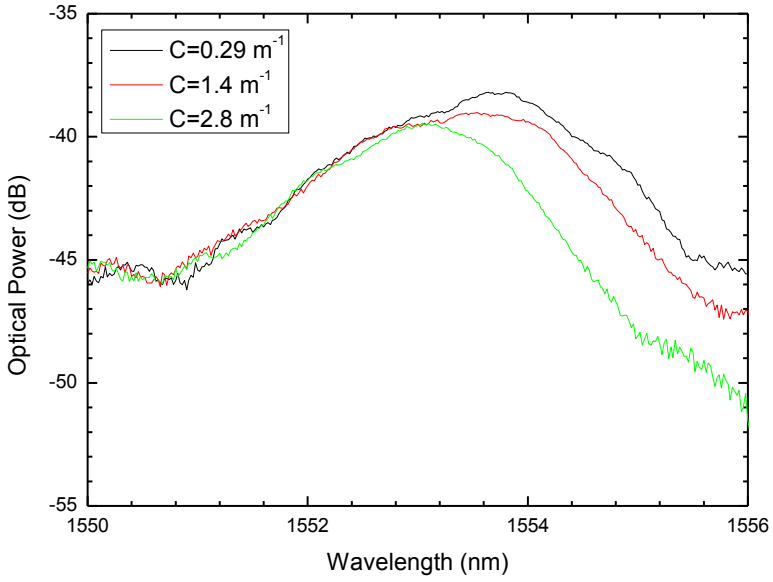

Fig. 6.3 Spectral response for different applied curvatures (reflection setup).

The average optical power (per nm) between 1550 nm and 1556 nm (the range which corresponded to the peaks presented in Fig. 6.3 and which presented the highest sensitivity of the output spectrum) was measured as a function of the curvature (Fig. 6.4) when the bending direction had an angle with the plane of the cores of 0 degrees (along the plane of the cores), 30 degrees and 90 degrees (perpendicular to the plane of the cores).

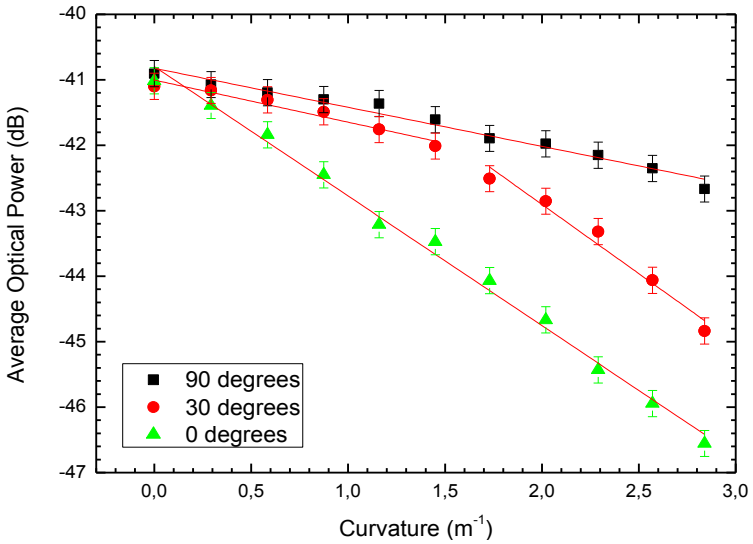

Fig. 6.4 Average optical power vs curvature for rotation angles of 0º, 30º and 90º of the PCF along its axis (Solid lines are a linear fit of the experimental data; for the 30 degrees measurements two regimes are considered: low curvatures (0-1.5 m^{-1}) and high curvatures (1.7-2.8 m^{-1})).

When the fibre is bent, the coupling coefficient between the three cores is changed. If the fibre is bent along the plane of the cores, one of the lateral cores will be stretched and the other one compressed, inducing a high variation of the coupling coefficient. In this case, high sensitivity is expected due to the exchange of optical power between the lateral cores and the central core. However, if the bending direction is perpendicular to the plane of the cores, the lateral cores will experience a similar mechanical stress, resulting in a small variation of the coupling coefficient. In this case, when the curvature is applied, optical power is lost to the cladding. Therefore, the coupling coefficient (and the curvature sensitivity) will strongly depend on the direction of bending, having its maximum when the bending direction is along the plane of the cores, and its minimum when the bending direction is perpendicular to the plane of the cores.

The side cores are weakly coupled to the SMF, and therefore the optical power transferred from the PCF to the SMF will be mostly the optical power in the central core. Since the optical power transferred from the central core to the side cores is dependent on the coupling coefficient between the cores, the output optical power will be dependent on the coupling coefficient, which in turn is dependent on the curvature.

A theoretical model is being developed in which the dependence of the coupling coefficient between the three cores on the curvature and on the other parameters of the fibre will be explicitly given. However, the coupling coefficient should be dependent on the diameter *d* of the air holes (mainly the ones between the cores), and on the diameter

of the cores. Furthermore, although the V-parameter was not calculated, the values of the relative hole diameter $\frac{d}{\Lambda}$, the parameter $\frac{\lambda}{\Lambda}$, and the diameter of the cores place the fibre in the "single-mode" operation region (each core should only have one mode when considered separately) [171].

The main results are summarized in Table 6.1. As expected, the sensitivity of the average optical power on the curvature is higher when the bending direction is along the plane of the cores (0 degrees). With a rotation angle of 0 degrees, a linear response with a curvature sensitivity of 2.0±0.1 dB/m^{-1} was obtained. As for the angle of 90 degrees, a linear response with a curvature sensitivity of 0.60±0.06 dB/m^{-1} was also obtained, i.e. approximately three times lower than the 0 degrees measurement.

Regarding the measurement with an angle of 30 degrees (value in between the two previous angles) a nonlinear behaviour was observed. This behaviour is the combination of the two effects explained previously, i.e., for low curvatures, the behaviour is similar to the 90 degrees case, since the optical power exchange between the cores is not strong. However, for high curvatures, the optical power exchange between central and lateral cores will be higher, and a behaviour similar to the 0 degrees case is observed. Furthermore, optical power will be lost to the cladding, providing an even higher sensitivity than the 0 degrees measurement. The nonlinear response was divided in two linear regimes, for low curvatures and high curvatures. For the low curvature regime (0-1.5 m^{-1}), a sensitivity of 0.6±0.1 dB/m^{-1} was achieved, and for the high curvature regime (1.7-2.8 m^{-1}), a sensitivity of 2.1±0.4 dB/m^{-1} was obtained.

Table 6.1 Curvature sensor parameters

	90 Degrees	**30 Degrees**		**0 Degrees**
Maximum Average Power Variation (dB)	1.8±0.4	3.7±0.4		5.2±0.4
Measurement Range (m^{-1})	0-2.8	0-1.5	1.7-2.8	0-2.8
Curvature Sensitivity (dB/m^{-1})	-0.60±0.06	-0.6±0.1	-2.1±0.4	-2.0±0.1

6.1.3 Conclusions

A new type of intensity curvature sensor using a three core PCF was demonstrated and characterized. The sensor uses the variation of the coupling coefficient between the fibre cores with curvature, and was interrogated in optical power variation when the

sensing head was subjected to curvature. Furthermore, the sensitivity can be tuned by applying the curvature along different planes. A maximum curvature sensitivity of 2.0±0.1 dB/m^{-1} was obtained for a measurement range of 0-2.8 m^{-1}.

Although for shorter measurement ranges sensors with much higher sensitivities have been demonstrated [169], the presented sensor has a similar sensitivity to other fibre based intensity curvature sensors for similar measurement ranges [168]. Using interferometric techniques, curvature sensors with a sensitivity up to an order of magnitude higher than the presented sensor have been reported [165, 172]. This sensor, however, is focused on providing a simpler interrogation scheme, and has also the advantage of using a reflection interrogation scheme which is simpler to implement in practical applications. Furthermore, the sensitivity of the presented sensor can be increased while maintaining the simplicity of the interrogation scheme by increasing the length of the PCF.

6.2 High sensitivity dispersive Mach-Zehnder interferometer based on a dissimilar-doping dual-core fibre for sensing applications

6.2.1 Introduction

In the work reported in the present chapter, a dual-core fibre, in which one of the cores is doped with Germanium and the other one with Phosphorus, is used as an in-line MZ dispersive interferometer. By ensuring equal lengths of the interferometer arms (the two cores), but with different dispersion dependencies, high sensitivity strain and temperature sensing were achieved. Opposite sensitivities for high and low wavelength peaks were also demonstrated when strain and temperature were applied. To our knowledge, this is the first time that such behaviour is demonstrated using this type of in-line interferometer based on a dual-core fibre. The dispersive interferometer was characterized in strain and temperature, and demonstrated to be an alternative solution for high sensitivity measurement of these magnitudes. The main results presented in this chapter were published in Optics Letters [6].

State-of-the-Art

Dual-core, or two-core fibres, were first proposed as strain sensors in 1981 [173]. These types of fibres were also demonstrated as temperature sensors in 1983 [174]. With the advent of microstructured fibres, several dual-core fibres were developed, such as twin-core fibres with special air cladding [175], based on photonic band-gap fibres [176, 177], and polymer fibres [178]. Hybrid dual-core fibres, where light is guided by total internal reflection in one core and by band-gap guidance in the other, were also proposed for wavelength-selective coupling [179]. More recently, another type of microstructured dual-core fibre was developed: the suspended twin-core fibre. In this case, the two cores appear to be suspended in large air holes by thin glass bridges [180]. All these configurations can be used for measurement of different parameters, such as refractive index [177, 181, 182], or for biosensing [178]. Through the selective infiltration of a single hole with fluid along a dual-core PCF, a record sensitivity for a fibre device of 30100 nm per refractive index unit was demonstrated [182].

Usually, when the Mach-Zenhder interferometer is subjected to changes in a physical parameter, the phase changes as the length or/and the refractive index is altered in one of arms. The main advantage of using a single fibre with twin-cores is the stability of

the interferometer, namely with the temperature. Strong immunity to bending has also been demonstrated using a twin-core PCF for an in-line MZI [183]. Moreover, by designing the fibre to have two different cores, it can be made highly sensitive to these parameters. The design of the fibre also introduces relevant trade-offs: the optical coupling between the two cores can be a limitation when the two cores are close [178]. On the contrary, when the two cores are very distant, coupling light simultaneously from a SMF to the two cores may be challenging. In this case, to solve the problem, a tapered fibre splice is a convenient solution.

Dual-Core fibre

The dual-core fibre used as sensing device had a length of 0.5 m and measured losses of ~15 dB/km at 1550 nm. The host material of the fibre was pure silica and the diameter of the cladding was 125 μm. As for the cores, one of them was doped with germanium, had a diameter of 5.1 μm, an expected Δn of 0.013 (estimated from the fibre preform) and a numerical aperture of 0.195. The second core was doped with phosphorous, had a diameter of 6.4 μm, a Δn of 0.00835 and a numerical aperture of 0.155. The core sizes were chosen in order to achieve an estimated cutoff wavelength of ~1.3 μm in both cores. The distance between the two cores was approximately 14.9 μm, thus strongly reducing cross-talk between the two cores [178]. An image of the transversal cross-section of the dual-core fibre geometry is presented in Fig. 6.5.

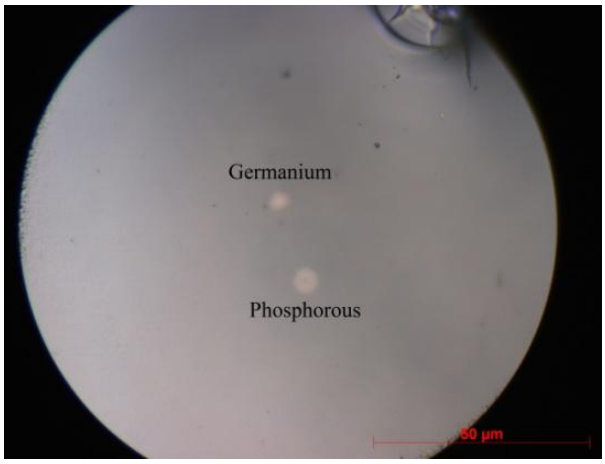

Fig. 6.5 Cross-section of the dual-core fibre, showing the germanium and phosphorous doped cores.

6.2.2 Theoretical Model

Firstly, a theoretical model for the dispersive interferometer is developed. The interferometer is created by splicing both ends of the dual-core fibre with standard

SMF. Since the two cores of the dual-core fibre have different refractive indices, these will present different optical paths, and so an interferometer is created. When strain or temperature variations are applied to the dual-core fibre, the optical path difference between the interferometer arms (the two cores) is changed, and therefore the optical spectrum at the end of the interferometer is changed. Since the two cores are built in the same silica matrix, the arms of the interferometer are assumed to always have the same length. This is a key aspect of the dual-core fibre-based MZ interferometer. In traditional MZ interferometers, a change in the length of an arm will change the phase by a factor proportional to the refractive index of the arms (n_1,n_2). In this case, however, a change in the fibre length will only change the phase by a factor proportional to the difference of the refractive index between the two cores ($\Delta n = n_1 - n_2$), which is much smaller than n_1,n_2. At the end of the dual-core fibre, the light in the core i will be given by

$$\overrightarrow{E_i}(\omega) = \overrightarrow{E_i} \cdot e^{j(L \cdot k_i(\omega) + \phi_0)}, \tag{6.2}$$

where E_i is the amplitude of the field of core i (i=1,2), L is the fibre length, and $k(\omega)_i$ is the wavenumber in core i, which is a function of the angular frequency (ω). Although some degree of birefringence must also exist in this type of fibre, a simple analysis allows concluding that for the number of fringes observed, the birefringence does not play an important role and is, therefore, neglected. Birefringence would essentially result in the superposition of two interferometers (the fast and slow axis of the cores) which would add an envelope function after a large number of fringes. The intensity of the light at the end of the dual-core fibre (from the sum of the fields coming from core 1 and core 2) will be given by

$$I_{out}(\omega) = I_1 + I_2 + 2\sqrt{I_1 I_2}\cos[L \cdot \Delta k(\omega)], \tag{6.3}$$

where $\Delta k(\omega) = k_1(\omega) - k_2(\omega)$. In this case, the evolution of the interference fringes of the dispersive interferometer will be determined by the argument of the cosine, hereinafter referred as the phase of the interferometer (Phase(ω)). When Phase(ω) has a value of $m \cdot 2\pi$ ($m \cdot 2\pi + \pi$), where m is an integer, the interference spectrum has a local maximum (minimum). Using the Taylor expansion of $\Delta k(\omega)$ around an arbitrary ω_0 we obtain:

$$\Delta k(\omega) = \Delta k(\omega_0) + (\omega - \omega_0)\left.\frac{\partial \Delta k}{\partial \omega}\right|_{\omega_0} + (\omega - \omega_0)^2 \frac{1}{2}\left.\frac{\partial^2 \Delta k}{\partial \omega^2}\right|_{\omega_0} + \ldots, \tag{6.4}$$

where $d\Delta k(\omega)/d\omega$ is the difference between the inverses of the group velocities of cores 1 and 2 at ω_0, and $d^2\Delta k(\omega)/d\omega^2$ is the difference between the group delay dispersions

($\Delta GDDs$) of cores 1 and 2 at ω_0. Dispersion terms of order higher than two are neglected as the frequency range used in the measurements is not very large. In conventional MZ interferometers based on twin-core fibres, the dispersion difference between the cores can be considered very low. Here, the fibre is actually composed of two cores with highly dissimilar dopings (Ge and P). This leads to an interesting dispersion behaviour of the interferometer around 1550 nm, which makes it especially sensitive. In the experimental measurements, it was observed that there is a situation for which Phase(ω) remains constant for variations of ω. For simplicity, we define ω_0 as this point, and therefore $d\Delta k(\omega)/d\omega$ equals zero at ω_0. Under these conditions, Phase(ω) will be a quadratic function with centre at ω_0. Fig. 6.6 shows three theoretical plots of Phase$(\omega)/2\pi$ as a function of wavelength (λ) (using $\lambda=2\pi c/\omega$) under different conditions, which are compared with the experimental measurements. The line a) shows the theoretical (and experimental) peak values obtained for the unstrained fibre at room temperature. In this case, the values used were: L=0.5 m, $\Delta k(\omega_0)=2\pi\Delta n_0/\lambda_0$, $\omega_0=2\pi c/\lambda_0$ where c is the velocity of light in the vacuum, λ_0=1540 nm the central wavelength in the vacuum and Δn_0= 0.0046559. For case b) where temperature was applied to the fibre (50ºC shift), the used values were L=0.5000125 m (the modified length was obtained using a coefficient of thermal expansion for silica of $\approx 10^{-6}$/ºC), λ_0=1553 nm and Δn_0=0.0047325; and for case c) where strain was applied to the fibre (1000 με), the used values were L=0.5005 m, λ_0=1533 nm and Δn_0= 0.0046079. In all cases, a value of ΔGDD=22 fs^2/mm (difference of the values of the dispersion parameter between the cores =41.4 ps/(nm.km)) was used, and good agreement was observed between the theoretical (when Phase$(\lambda)/2\pi$=integer) and experimental (dots of the graphic) peaks of the interferometer. With an increase/decrease of Δn_0, the value of Phase(ω) increases/decreases, causing the peaks to move towards/away from the centre of the dispersion interferometer (λ_0). In the simulations, it was possible to observe that changes in Δn_0 of 10^{-6} caused substantial (>1 nm) changes in the peaks positions. Equivalent variations in the peaks positions were only achieved in the simulation with changes of ΔL >1000 με (with Δn_0=constant). In this case, it is expected that when straining the fibre, the impact of the stress-optic coefficient will be higher than the impact of the fibre length increase, as demonstrated by the experimental results.

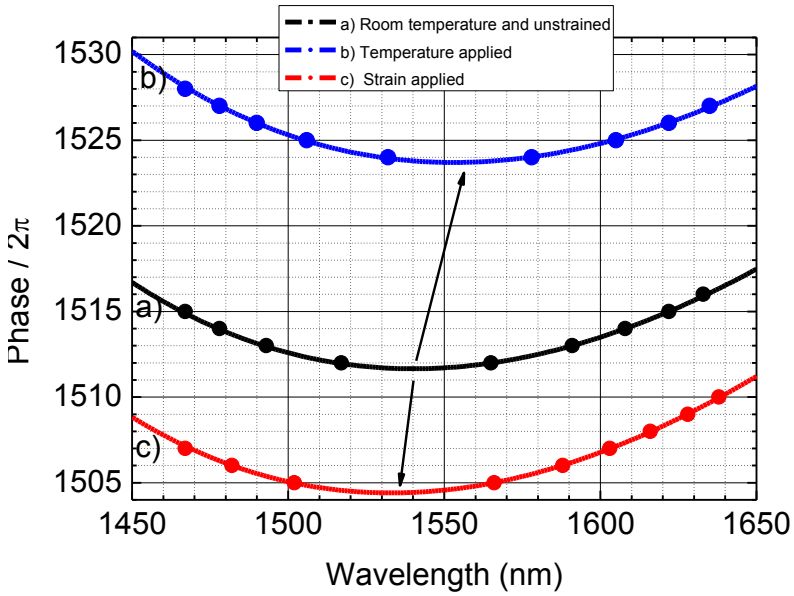

Fig. 6.6 Theoretical phase (the lines) of the interferometer as a function of the wavelength for a fibre at a) Room temperature with no strain, b) temperature applied, c) strain applied. The experimental peaks are also represented (dots). The values used in the simulation are presented in the text.

6.2.3 Experimental Work

Fig. 6.7 presents the experimental configuration used to characterize the dispersion interferometer based on a dual-core fibre as sensing element. The dispersive interferometer is created by splicing both ends of the dual-core fibre with SMF. The core of the SMF was placed between the two cores, thus minimizing the difference between the amount of light coupled into each one of the cores, therefore increasing the visibility. After the fusion splice, the fibre is tapered, reducing the diameter of the fibre in the splice region to ≈60 μm (approximately half the initial size). This increases the numerical aperture and, therefore, the coupling of light into both cores. Strain was applied to the dual core fibre by fixing one end to a stationary stage and the other end to a micrometric translation stage, which applied deformations at 13ºC. As for the temperature measurements, they were performed with no strain applied to the dual-core fibre. An erbium doped fibre amplifier (EDFA) was used to illuminate the dispersive interferometer and an OSA, with a maximum resolution of 0.01 nm, was used to interrogate it in transmission.

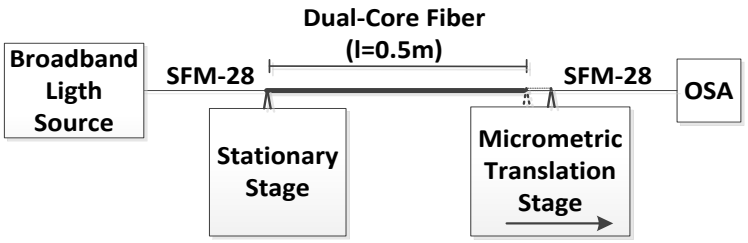

Fig. 6.7 Experimental setup used to characterize the dual-core fibre as a strain and temperature sensor.

Fig. 6.8 presents the transmission spectrum of the dispersive interferometer and the respective wavelength shift for increasing applied strain (Fig. 6.8a) and temperature (Fig. 6.8b). The characteristic dips of an interferometer out appear in the spectral response, as expected. The spacing between the dips presents symmetry around a central wavelength (at ≈1540 nm), and decreases when moving away from it. In terms of sensitivity (both to strain and temperature), the interferometer peaks present opposite response for wavelengths higher and lower than the central wavelength. These peaks move symmetrically away/towards the centre for applied strain/temperature, as predicted by the theoretical model. To our knowledge, this is the first time that this effect is observed in this type of in-line interferometer based on a dual-core fibre. As explained in the theoretical model, this is owed to a change in the sign of the derivative of $\Delta k(\omega)$. The visibility of the peaks seems to decrease when moving away from the centre. This effect, however, is owed to the emission spectrum of the EDFA, which transmits more light in the 1500-1600 nm range than in the rest of the observed range. When observed with a broader light source, the peaks presented similar visibilities in a higher range (at least 1400-1700 nm).

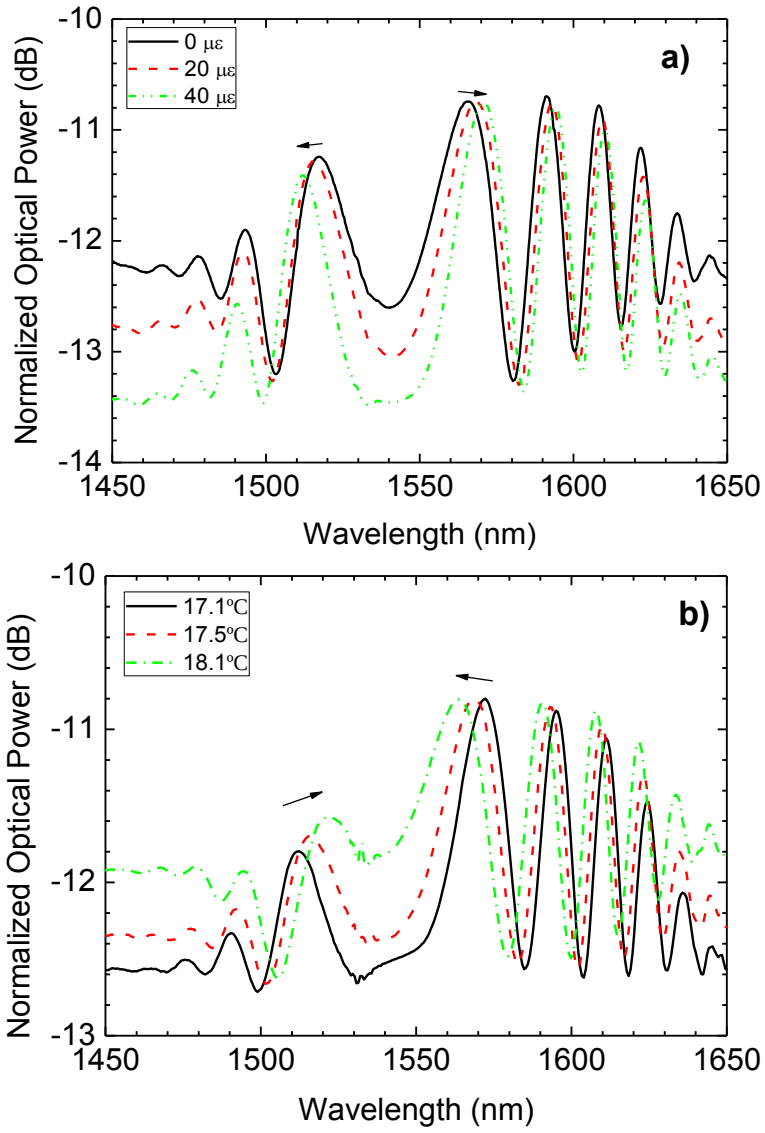

Fig. 6.8 Shift of the normalized transmission spectrum of the dispersive interferometer with increasing applied a) strain and b) temperature.

Fig. 6.9 shows the wavelength shift of the peaks of the dispersive interferometer spectrum when a) strain (at 13ºC) and b) temperature (with no strain) is applied.

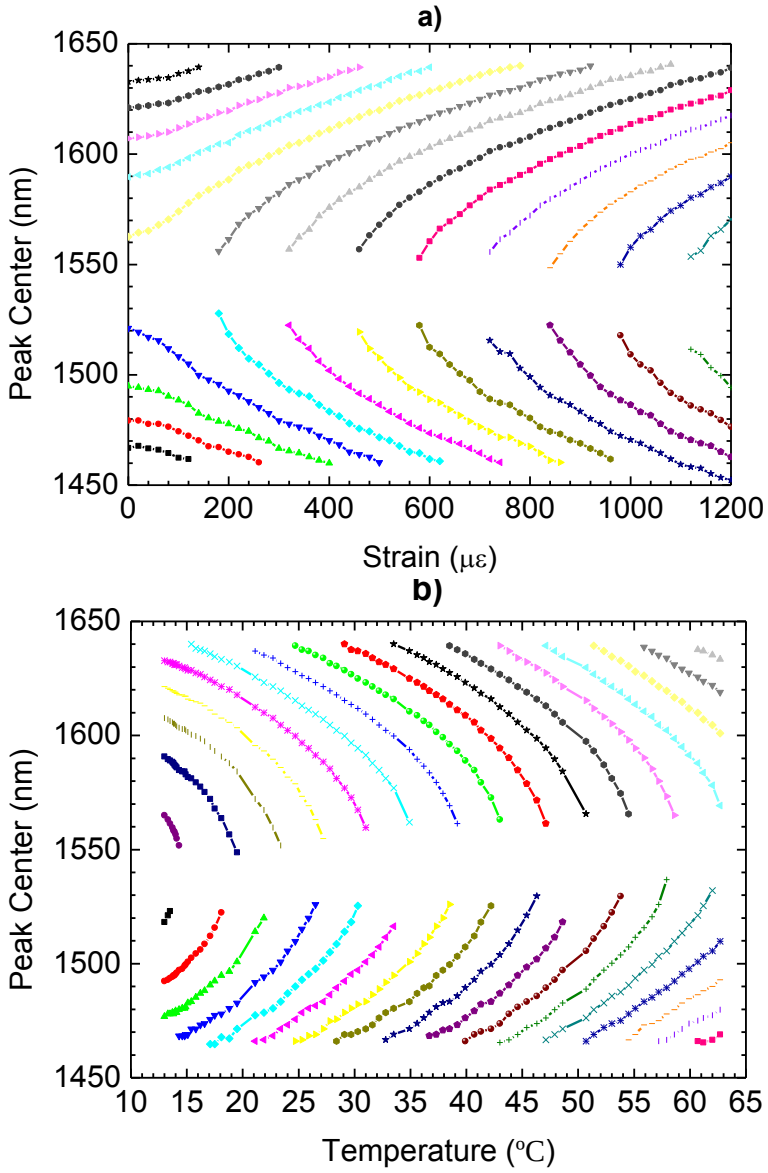

Fig. 6.9 Peaks wavelength shift of the dispersive interferometer spectrum as a function of the applied a) strain and b) temperature.

With increasing applied strain (Fig. 6.9a), the interference fringes are observed to move towards the centre. Given the parabolic nature of the evolution of Phase(λ), the sensitivity of the peaks decreases when moving away from the centre. Monitoring a single peak, average sensitivities of (-0.125±0.003) nm/με (1520-1460 nm) and of (0.102±0.002) nm/με (1540-1640 nm) were observed when a strain of up to 800 με was applied. This value is much higher than the typical values presented by fibre Bragg grating based sensors (≈1 pm/με [137]), or traditional dual-core in-line MZ interferometers (≈1 pm/$\mu\varepsilon$ [183, 184]), in which the difference between dispersion dependencies of the two cores is much weaker than the ones presented in this work.

As for the temperature measurements, with increasing applied temperature (Fig. 6.9b) the interference fringes are observed to move away from the centre. Monitoring a single peak, average sensitivities of (-4.0±0.1) nm/ºC (1640-1570 nm) and of (4.2±0.1) nm/ºC (1460-1540 nm) were observed when the temperature was raised from 47ºC to 62ºC. In this case, taking the resolution of the OSA (0.01 nm), resolutions of the experimental setup of 0.002 με and of 0.08ºC can be estimated.

It is also important to point out that the centre of the spectrum ($\Delta k(\omega)=0$) was observed to shift ≈-7 nm from 1540 nm to 1533 nm, while maintaining the form of the transmission spectrum, for an applied strain between 0-1000 $\mu\varepsilon$ (Fig. 6.9a), and ≈13 nm (from 1540 nm to 1553 nm) when the temperature was raised from 13ºC to 62ºC (Fig. 6.9b). This means that the dispersion curve was changed when applying temperature/strain. This effect can be used to measure the value of the absolute temperature/strain rather than only measuring variations of temperature/strain.

6.2.4 Conclusions

In conclusion, a new device concept for a highly sensitive MZ interferometer, based on a dual-core fibre with dissimilar-doping, is described theoretically and experimentally. By ensuring the same length in both arms of the interferometer (built in the same silica matrix), the interferometer is only sensitive to the variations in differential dispersion between the two cores, thus allowing high sensitivity strain and temperature sensing with also a good robustness and even potential for absolute measurements.

A theoretical model was presented, showing good agreement with the experimental results. Opposite sensitivities for wavelength peaks higher and lower than the central wavelength of the interferometer were demonstrated when strain and temperature were applied. To our knowledge, this is the first time that such behaviour is demonstrated using this type of in-line interferometer based on a dual-core fibre. The effect is demonstrated to be owed to a sign reversal in differential dispersion between the wavenumbers of the core fields.

A sensitivity of (0.102±0.002) nm/$\mu\varepsilon$, between 0-800 $\mu\varepsilon$, and of (-4.0±0.2) nm/ºC between 47-62ºC is demonstrated. The centre of the spectrum was observed to shift to higher/lower wavelengths with applied temperature/strain, which allows the measurement of absolute temperature/strain.

7 Final Conclusions and Future Work

7.1 Final Conclusions

The results reported in this PhD thesis fulfill all the proposed objectives of the work plan.

The use of phase-sensitive optical time domain reflectometry (ϕOTDR), and the effects involved in its operation, were studied for both dynamic and static measurements. MI was identified as the limiting nonlinear effect of the performance of a ϕOTDR under normal operation conditions, and its impact on ϕOTDR operation was thoroughly described, both theoretically and experimentally. For dynamic sensing, mainly distributed vibration along optical fibres, three configurations were tested which presented different trade-offs in their performances: ϕOTDR without amplification (39.5 kHz over 1.25 km, 5 m resolution), assisted by first-order Raman amplification (250/300 Hz over 125/110 km, 10 m resolution), and assisted by second-order Raman amplification (380 Hz over 125 km, 10 m resolution). Apart from achieving frequency measurements in the limits set by the time of flight of light using ϕOTDR without amplification and assisted by second-order Raman amplification, to the best of our knowledge, the presented results include records in ϕOTDR distributed vibration sensing for the highest vibration frequency detected (39.5 kHz) and the largest sensing range (125 km) at the time of publication of ref. [3] and [5], respectively. The noise was carefully characterized and minimized in all configurations, and balanced detection was demonstrated to greatly reduce the RIN, which is one of the main undesired effects which arise with the use of Raman amplification.

As for static measurements, a technique based on the correlation of ϕOTDR measurements at two orthogonal states of polarization was used to achieve high sensitivity distributed measurement of birefringence over very long optical fibres (PMFs and SMFs), with an ultimate accuracy of 10^{-7} for a spatial resolution of 2 m.

A new configuration for an intensity vibration sensor based on a Raman fibre laser was demonstrated for remote point sensing. The sensor was able to measure vibrations with frequencies of up to 350 Hz, and also the amplitude of the vibrations with a sensitivity of up to 0.57±0.07 dB/με ($2.3\pm0.3\cdot10^{13}$ dB/(ms^{-2}) for 100 Hz) for vibrations with a maximum strain variation of up to 35 με.

As a result of parallel projects which were not directly connected to the main theme of the thesis, it was possible to test microstructured fibres for different applications. An intensity curvature sensor, with a sensitivity of 2.0±0.1 dB/m^{-1}, based on a three core PCF, and a high-sensitivity strain and temperature sensor with a sensitivity of (0.102±0.002) nm/$\mu\varepsilon$, between 0-800 $\mu\varepsilon$, and of (-4.0±0.2) nm/ºC, based on a dissimilar-doping dual-core fibre, were demonstrated.

7.2 Future Work

The following topics are proposed for further improvement of the work developed in the PhD programme:

- For distributed vibration sensing using ϕOTDR, given that the RIN was one of the main limitations imposed by Raman amplification, the use of semiconductor lasers (which present lower RIN figures than Raman fibre lasers) as pumps to provide the amplification should be tested. The combination of first- and second-order Raman amplification, which has been demonstrated to improve the performance of Brillouin based systems, also presents an interesting possibility to further improve the range of sensing. The use of post-processing denoising was not addressed in this PhD programme, but could improve the performance of the system. Lastly, once the detection of vibrations is clearly established, it is then very important to interpret what these vibrations mean: the analyses of signature patterns resultant from different perturbations (e.g. distinguish the pattern of people walking from cars moving around the fibre) is of critical importance when working towards practical applications.
- Consolidate the work using ϕOTDR for distributed birefringence measurements and test the limits of its performance, such as the maximum fibre length which can be measured and the spatial resolution. The noise should be properly characterized and the main limiting factors (which can be strongly dependent on the type of fibre used) should be identified. More efficient ways to perform the measurement can also be proposed: by using unpolarized light and correlating the measured frequency sweep with itself, it may be possible to perform measurements with a single frequency sweep, thus decreasing the measurement time and increasing the stability of the system. After that, the possibility of using

amplification to improve the range of the measurements can also be addressed. A number of interesting applications based on this work can be proposed, such as measurement of pressure or curvature.

- Test the possibility of multiplexing using the setup of URFL for remote point sensing.
- Test the possibility of integrating microstructured fibres in distributed sensing.

References

References

1. Martins, H., et al., *Intensity curvature sensor based on photonic crystal fiber with three coupled cores.* Optics Communications, 2012. **285**(24): p. 5128-5131.
2. Martins, H.F., et al., *Modulation instability-induced fading in phase-sensitive optical time-domain reflectometry.* Optics Letters, 2013. **38**(6): p. 872-874.
3. Martins, H.F., et al., *Coherent Noise Reduction in High Visibility Phase-Sensitive Optical Time Domain Reflectometer for Distributed Sensing of Ultrasonic Waves.* Journal of Lightwave Technology, 2013. **31**(23): p. 3631-3637.
4. Martins, H.F., M.B. Marques, and O. Frazão, *Intensity vibration sensor based on Raman fiber laser using a distributed mirror combined with Bragg grating structures.* Applied Physics B, 2014. **114**(4): p. 455-459.
5. Martins, H.F., et al., *Phase-sensitive optical time domain reflectometer assisted by first-order Raman amplification for distributed vibration sensing over >100km.* Journal of Lightwave Technology, 2014. **32**(8): p. 1510-1518.
6. Martins, H.F., et al., *High-sensitivity dispersive Mach -Zehnder interferometer based on a dissimilar-doping dual-core fiber for sensing applications.* Optics Letters, 2014. **39**(9): p. 2763-2766.
7. Boyd, R.W., *Nonlinear Optics*. Third ed2008: Academic Press.
8. Keck, D.B., R.D. Maurer, and P.C. Schultz, *Ultimate Lower Limit of Attenuation in Glass Optical Waveguides.* Applied Physics Letters, 1973. **22**(7): p. 307-309.
9. Agrawal, G.P., *Nonlinear Fiber Optics*. Third ed2001: Academic Press.
10. Paulo Sérgio, B.A., *Componentes optoelectrónicos para redes fotónicas de alto débito*, in *Physics Department*2002, University of Aveiro.
11. Cohen, L.G., C. Lin, and W.G. French, *Tailoring Zero Chromatic Dispersion into the 1.5-1.6 Mu-M Low-Loss Spectral Region of Single-Mode Fibers.* Electronics Letters, 1979. **15**(12): p. 334-335.
12. Kaminow, I.P., *Polarization in Optical Fibers.* Ieee Journal of Quantum Electronics, 1981. **17**(1): p. 15-22.
13. Wikipedia. *http://en.wikipedia.org/wiki/Polarization-maintaining_optical_fiber*. accessed in 01/03/2014].
14. Maier, R.R.J., et al., *Distributed sensing using Rayleigh scatter in polarization-maintaining fibres for transverse load sensing.* Measurement Science & Technology, 2010. **21**(9).
15. Tai, K., A. Hasegawa, and A. Tomita, *Observation of Modulational Instability in Optical Fibers.* Physical Review Letters, 1986. **56**(2): p. 135-138.
16. Alasia, D., et al., *Detrimental effect of modulation instability on distributed optical fibre sensors using stimulated Brillouin scattering.* 17th International Conference on Optical Fibre Sensors, Pts 1 and 2, 2005. **5855**: p. 587-590.
17. Agrawal, G.P., *Nonlinear Fiber Optics*, 2001, Academic Press. p. 136-140.
18. Orlando José dos Reis, F., *Sensores em Fibra Óptica Baseados em Interferometria e Efeitos Não-Lineares*, in *Physics Department*2009, University of Porto.
19. Islam, M.N., *Raman Amplifiers for Telecommunications I - Physical Principles*. Springer Series in Optical Sciences, 2004: Springer-Velag.
20. Dakin, J.P., et al., *Distributed Optical Fiber Raman Temperature Sensor Using a Semiconductor Light-Source and Detector.* Electronics Letters, 1985. **21**(13): p. 569-570.

21. Eckhardt, G., et al., *Stimulated Raman Scattering from Organic Liquids.* Physical Review Letters, 1962. **9**(11): p. 455-&.
22. Ania-Castanon, J.D., et al., *Ultralong raman fiber lasers as virtually lossless optical media.* Physical Review Letters, 2006. **96**(2): p. -.
23. Rodriguez-Barrios, F., et al., *Distributed Brillouin Fiber Sensor Assisted by First-Order Raman Amplification.* Lightwave Technology, Journal of, 2010. **28**(15): p. 2162-2172.
24. Shimizu, K., T. Horiguchi, and Y. Koyamada, *Characteristics and Reduction of Coherent Fading Noise in Rayleigh Backscattering Measurement for Optical Fibers and Components.* Journal of Lightwave Technology, 1992. **10**(7): p. 982-988.
25. Lu, Y.L., et al., *Distributed Vibration Sensor Based on Coherent Detection of Phase-OTDR.* Journal of Lightwave Technology, 2010. **28**(22): p. 3243-3249.
26. Qin, Z.G., et al., *High Sensitivity Distributed Vibration Sensor Based on Polarization-Maintaining Configurations of Phase-OTDR.* Ieee Photonics Technology Letters, 2011. **23**(15): p. 1091-1093.
27. Koyamada, Y., et al., *Fiber-Optic Distributed Strain and Temperature Sensing With Very High Measurand Resolution Over Long Range Using Coherent OTDR.* Journal of Lightwave Technology, 2009. **27**(9): p. 1142-1146.
28. Taylor, H.F. and C.E. Lee, *Apparatus and method for fiber optic intrusion sensing*, U.S. Patent 5194847, Texas A & M University System, March 16, 1993.
29. Park, J. and H.F. Taylor, *Fiber optic intrusion sensor.* Fiber Optic Sensors V, 1996. **2895**: p. 214-221.
30. Park, J.H., W.K. Lee, and H.F. Taylor, *A fiber optic intrusion sensor with the configuration of an optical time domain reflectometer using coherent interference of Rayleigh backscattering.* Optical and Fiber Optic Sensor Systems, 1998. **3555**: p. 49-56.
31. Choi, K.N. and H.F. Taylor, *Spectrally stable Er-fiber laser for application in phase-sensitive optical time-domain reflectometry.* Ieee Photonics Technology Letters, 2003. **15**(3): p. 386-388.
32. Juarez, J.C., et al., *Distributed fiber-optic intrusion sensor system.* Journal of Lightwave Technology, 2005. **23**(6): p. 2081-2087.
33. Juarez, J.C. and H.F. Taylor, *Field test of a distributed fiber-optic intrusion sensor system for long perimeters.* Applied Optics, 2007. **46**(11): p. 1968-1971.
34. Shatalin, S.V., V.N. Treschikov, and A.J. Rogers, *Interferometric optical time-domain reflectometry for distributed optical-fiber sensing.* Applied Optics, 1998. **37**(24): p. 5600-5604.
35. Zhou, J., et al., *Characteristics and Explanations of Interference Fading of a phi-OTDR With a Multi-Frequency Source.* Journal of Lightwave Technology, 2013. **31**(17): p. 2947-2954.
36. Zhu, T., et al., *Enhancement of SNR and Spatial Resolution in phi-OTDR System by Using Two-Dimensional Edge Detection Method.* Journal of Lightwave Technology, 2013. **31**(17): p. 2851-2856.
37. Pan, Z.Q., et al., *Phase-sensitive OTDR system based on digital coherent detection.* Optical Sensors and Biophotonics Iii, 2011. **8311**.
38. Peng, F., et al., *Ultra-long high-sensitivity phi-OTDR for high spatial resolution intrusion detection of pipelines.* Optics Express, 2014. **22**(11): p. 13804-13810.

39. Juarez, J.C. and H.F. Taylor, *Polarization discrimination in a phase-sensitive optical time-domain reflectometer intrusion-sensor system.* Optics Letters, 2005. **30**(24): p. 3284-3286.
40. Qin, Z.G., L. Chen, and X.Y. Bao, *Continuous wavelet transform for non-stationary vibration detection with phase-OTDR.* Optics Express, 2012. **20**(18): p. 20459-20465.
41. Qin, Z.G., L. Chen, and X.Y. Bao, *Wavelet Denoising Method for Improving Detection Performance of Distributed Vibration Sensor.* Ieee Photonics Technology Letters, 2012. **24**(7): p. 542-544.
42. Izumita, H., et al., *Stochastic amplitude fluctuation in coherent OTDR and a new technique for its reduction by stimulating synchronous optical frequency hopping.* Journal of Lightwave Technology, 1997. **15**(2): p. 267-278.
43. Li, J., et al., *124km phase-sensitive OTDR with Brillouin amplification.* 23rd International Conference on Optical Fibre Sensors, 2014. **9157**.
44. Wang, Z., et al., *175km Phase-sensitive OTDR with Hybrid Distributed Amplification.* 23rd International Conference on Optical Fibre Sensors, 2014. **9157**.
45. Madsen, C.K., T. Bae, and T. Snider, *Intruder signature analysis from a phase-sensitive distributed fiber-optic perimeter sensor - art. no. 6770OK.* Fiber Optic Sensors and Applications V, 2007. **6770**: p. Ok770-Ok770.
46. Wang, J., et al., *Phase-sensitive optical time-domain reflectometer based on bi-directional Raman amplification.* Acta Physica Sinica, 2013. **62**(4).
47. Bristiel, B., et al., *New model of noise figure and RIN transfer in fiber Raman amplifiers.* Ieee Photonics Technology Letters, 2006. **18**(5-8): p. 980-982.
48. Izumita, H., et al., *The Performance Limit of Coherent Otdr Enhanced with Optical-Fiber Amplifiers Due to Optical Nonlinear Phenomena.* Journal of Lightwave Technology, 1994. **12**(7): p. 1230-1238.
49. Van Simaeys, G., P. Emplit, and M. Haelterman, *Experimental study of the reversible behavior of modulational instability in optical fibers.* Journal of the Optical Society of America B-Optical Physics, 2002. **19**(3): p. 477-486.
50. Anderson, D., et al., *Features of modulational instability of partially coherent light: Importance of the incoherence spectrum (vol E 69, art no 025601, 2004).* Physical Review E, 2004. **69**(3).
51. Van Simaeys, G., P. Emplit, and M. Haelterman, *Experimental demonstration of the Fermi-Pasta-Ulam recurrence in a modulationally unstable optical wave.* Physical Review Letters, 2001. **87**(3).
52. Hegarty, J., N.A. Olsson, and L. Goldner, *Cw Pumped Raman Preamplifier in a 45 Km-Long Fiber Transmission-System Operating at 1.5 Mu-M and 1 Gbit/S.* Electronics Letters, 1985. **21**(7): p. 290-292.
53. Aoki, Y., *Properties of Fiber Raman Amplifiers and Their Applicability to Digital Optical Communication-Systems.* Journal of Lightwave Technology, 1988. **6**(7): p. 1225-1239.
54. Hansen, P.B., et al., *Capacity upgrades of transmission systems by Raman amplification.* Ieee Photonics Technology Letters, 1997. **9**(2): p. 262-264.
55. Turitsyn, S.K., et al., *270-km Ultralong Raman Fiber Laser.* Physical Review Letters, 2009. **103**(13): p. -.
56. Alahbabi, M.N., Y.T. Cho, and T.P. Newson, *150-km-range distributed temperature sensor based on coherent detection of spontaneous Brillouin backscatter and in-line Raman amplification.* Journal of the Optical Society of America B-Optical Physics, 2005. **22**(6): p. 1321-1324.

57. Martin-Lopez, S., et al., *Brillouin optical time-domain analysis assisted by second-order Raman amplification.* Optics Express, 2010. **18**(18): p. 18769-18778.
58. Martins, H., M.B. Marques, and O. Frazao, *300 km-ultralong Raman fiber lasers using a distributed mirror for sensing applications.* Optics Express, 2011. **19**(19): p. 18149-18154.
59. Jia, X.H., et al., *Detailed theoretical investigation on improved quasi-lossless transmission using third-order Raman amplification based on ultralong fiber lasers.* Journal of the Optical Society of America B-Optical Physics, 2012. **29**(4): p. 847-854.
60. Nuno, J., M. Alcon-Camas, and J.D. Ania-Castanon, *RIN transfer in random distributed feedback fiber lasers.* Optics Express, 2012. **20**(24): p. 27376-27381.
61. Martins, H.F., et al., *Comparison of the use of first and second-order Raman amplification to assist a phase-sensitive optical time domain reflectometer in distributed vibration sensing over 125 km.* 23rd International Conference on Optical Fibre Sensors, 2014. **9157**.
62. Alcon-Camas, M. and J.D. Ania-Castanon, *RIN transfer in 2nd-order distributed amplification with ultralong fiber lasers.* Optics Express, 2010. **18**(23): p. 23569-23575.
63. Rao, Y.-J., et al., *Long-distance fiber-optic phi-OTDR intrusion sensing system.* 20th International Conference on Optical Fibre Sensors, 2009. **7503**.
64. He, Q., et al., *Real distributed vibration sensing with high frequency response based on pulse pair.* 23rd International Conference on Optical Fibre Sensors, 2014. **9157**.
65. Pan, Z., et al., *High sampling rate multi-pulse phase-sensitive OTDR employing frequency division multiplexing.* 23rd International Conference on Optical Fibre Sensors, 2014. **9157**.
66. He, Q., et al., *All Fiber Distributed Vibration Sensing Using Modulated Time-Difference Pulses.* Ieee Photonics Technology Letters, 2013. **25**(20): p. 1955-1957.
67. Zhu, T., et al., *Modulated pulses based distributed vibration sensing with high frequency response and spatial resolution.* Optics Express, 2013. **21**(3): p. 2953-2963.
68. Rao, Y.J., et al., *Distributed intrusion detection based on combination of phi-OTDR and POTDR.* 19th International Conference on Optical Fibre Sensors, Pts 1 and 2, 2008. **7004**.
69. Masoudi, A., M. Belal, and T.P. Newson, *A distributed optical fibre dynamic strain sensor based on phase-OTDR.* Measurement Science & Technology, 2013. **24**(8).
70. Denisov, A., M.A. Soto, and L. Thévenaz, *1'000'000 resolved points along a Brillouin distributed fibre sensor.* 23rd International Conference on Optical Fibre Sensors, 2014. **9157**.
71. Soller, B.J., et al., *High resolution optical frequency domain reflectometry for characterization of components and assemblies.* Optics Express, 2005. **13**(2): p. 666-674.
72. Angulo-Vinuesa, X., et al., *Raman-assisted Brillouin optical time-domain analysis with sub-meter resolution over 100 km.* Optics Express, 2012. **20**(11): p. 12147-12154.

73. Viveiros, D., et al., *Fiber optic sensing system for monitoring of coal waste piles in combustion.* 23rd International Conference on Optical Fibre Sensors, 2014. **9157**.
74. Lopez-Higuera, J.M., et al., *Fiber Optic Sensors in Structural Health Monitoring.* Journal of Lightwave Technology, 2011. **29**(4): p. 587-608.
75. Horiguchi, T. and M. Tateda, *Optical-Fiber-Attenuation Investigation Using Stimulated Brillouin-Scattering between a Pulse and a Continuous Wave.* Optics Letters, 1989. **14**(8): p. 408-410.
76. Barnoski, M.K., et al., *Optical Time Domain Reflectometer.* Applied Optics, 1977. **16**(9): p. 2375-2379.
77. Thévenaz, L. *Review and progress in distributed fiber sensing*. in *Optical Fiber Sensors, OFS 2006*. 2006. Cancun; Mexico.
78. Bao, X.Y. and L. Chen, *Recent Progress in Distributed Fiber Optic Sensors.* Sensors, 2012. **12**(7): p. 8601-8639.
79. Barnoski, M.K. and S.M. Jensen, *Fiber Waveguides - Novel Technique for Investigating Attenuation Characteristics.* Applied Optics, 1976. **15**(9): p. 2112-2115.
80. Koyamada, Y. and H. Nakamoto, *High-Performance Single-Mode Otdr Using Coherent Detection and Fiber Amplifiers.* Electronics Letters, 1990. **26**(9): p. 573-575.
81. Healey, P., *Fading in Heterodyne Otdr.* Electronics Letters, 1984. **20**(1): p. 30-32.
82. Rogers, A.J., *Polarization Optical-Time Domain Reflectometry.* Electronics Letters, 1980. **16**(13): p. 489-490.
83. Wuilpart, M., et al., *Measurement of the spatial distribution of birefringence in optical fibers.* Ieee Photonics Technology Letters, 2001. **13**(8): p. 836-838.
84. Corsi, F., A. Galtarossa, and L. Palmieri, *Polarization mode dispersion characterization of single-mode optical fiber using backscattering technique.* Journal of Lightwave Technology, 1998. **16**(10): p. 1832-1843.
85. Ellison, J.G. and A.S. Siddiqui, *A fully polarimetric optical time-domain reflectometer.* Ieee Photonics Technology Letters, 1998. **10**(2): p. 246-248.
86. Huttner, B., B. Gisin, and N. Gisin, *Distributed PMD measurement with a polarization-OTDR in optical fibers.* Journal of Lightwave Technology, 1999. **17**(10): p. 1843-1848.
87. Galtarossa, A. and L. Palmieri, *Spatially resolved PMD measurements.* Journal of Lightwave Technology, 2004. **22**(4): p. 1103-1115.
88. Peng, F., et al., *106km fully-distributed fiber-optic fence based on P-OTDR with 2nd-order Raman amplification.* 2013 Optical Fiber Communication Conference and Exposition and the National Fiber Optic Engineers Conference (Ofc/Nfoec), 2013.
89. Linze, N., P. Megret, and M. Wuilpart, *Development of an Intrusion Sensor Based on a Polarization-OTDR System.* Ieee Sensors Journal, 2012. **12**(10): p. 3005-3009.
90. Zhang, Z.Y. and X.Y. Bao, *Distributed optical fiber vibration sensor based on spectrum analysis of Polarization-OTDR system.* Optics Express, 2008. **16**(14): p. 10240-10247.
91. Oberson, P., et al., *Optical frequency domain reflectometry with a narrow linewidth fiber laser.* Ieee Photonics Technology Letters, 2000. **12**(7): p. 867-869.

92. Eickhoff, W. and R. Ulrich, *Optical Frequency-Domain Reflectometry in Single-Mode Fiber.* Applied Physics Letters, 1981. **39**(9): p. 693-695.
93. Wait, P.C., K. DeSouza, and T.P. Newson, *A theoretical comparison of spontaneous Raman and Brillouin based fibre optic distributed temperature sensors.* Optics Communications, 1997. **144**(1-3): p. 17-23.
94. Farahani, M.A. and T. Gogolla, *Spontaneous raman scattering in optical fibers with modulated probe light for distributed temperature Raman remote sensing.* Journal of Lightwave Technology, 1999. **17**(8): p. 1379-1391.
95. Dyer, S.D., et al., *Analysis of a distributed fiber-optic temperature sensor using single-photon detectors.* Optics Express, 2012. **20**(4): p. 3456-3466.
96. Bolognini, G., et al., *Analysis of distributed temperature sensing based on Raman scattering using OTDR coding and discrete Raman amplification.* Measurement Science & Technology, 2007. **18**(10): p. 3211-3218.
97. Belal, M., et al., *A temperature-compensated high spatial resolution distributed strain sensor.* Measurement Science & Technology, 2010. **21**(1).
98. Shimizu, K., et al., *Coherent Self-Heterodyne Detection of Spontaneously Brillouin-Scattered Light Waves in a Single-Mode Fiber.* Optics Letters, 1993. **18**(3): p. 185-187.
99. Kurashima, T., T. Horiguchi, and M. Tateda, *Distributed-Temperature Sensing Using Stimulated Brillouin-Scattering in Optical Silica Fibers.* Optics Letters, 1990. **15**(18): p. 1038-1040.
100. Soto, M.A., et al., *Extending the Real Remoteness of Long-Range Brillouin Optical Time-Domain Fiber Analyzers.* Journal of Lightwave Technology, 2014. **32**(1): p. 152-162.
101. Nikles, M., L. Thevenaz, and P.A. Robert, *Brillouin gain spectrum characterization in single-mode optical fibers.* Journal of Lightwave Technology, 1997. **15**(10): p. 1842-1851.
102. Bao, X., D.J. Webb, and D.A. Jackson, *32-Km Distributed Temperature Sensor-Based on Brillouin Loss in an Optical-Fiber.* Optics Letters, 1993. **18**(18): p. 1561-1563.
103. Brown, A.W., B.G. Colpitts, and K. Brown, *Dark-pulse Brillouin optical time-domain sensor with 20-mm spatial resolution.* Journal of Lightwave Technology, 2007. **25**(1): p. 381-386.
104. Song, K.Y., et al., *Time-Domain Distributed Fiber Sensor With 1 cm Spatial Resolution Based on Brillouin Dynamic Grating.* Journal of Lightwave Technology, 2010. **28**(14): p. 2062-2067.
105. Jamioy, C.A.G. and J.M. Lopez-Higuera, *Decimeter Spatial Resolution by Using Differential Preexcitation BOTDA Pulse Technique.* Ieee Sensors Journal, 2011. **11**(10).
106. Foaleng, S.M., et al., *High Spatial and Spectral Resolution Long-Range Sensing Using Brillouin Echoes.* Journal of Lightwave Technology, 2010. **28**(20): p. 2993-3003.
107. Dong, Y.K., et al., *2 cm spatial-resolution and 2 km range Brillouin optical fiber sensor using a transient differential pulse pair.* Applied Optics, 2012. **51**(9): p. 1229-1235.
108. Wojcik, A.K., *Signal statistics of phase dependent optical time domain reflectometry*, 2006, Texas A&M University: Available at: http://hdl.handle.net/1969.1/4873.

109. Kotz, S., T.J. Kozubowski, and K. Podgórski, *The Laplace distribution and generalizations: a revisit with applications to Communications, Economics, Engineering and Finance*, 2001, Boston: Birkhäuser. p. 23.
110. Agrawal, G.P., *Fiber Optic Communication Systems*, 2002: ., New York: Wiley. p. 156-158.
111. Baney, D.M., P. Gallion, and R.S. Tucker, *Theory and measurement techniques for the noise figure of optical amplifiers.* Optical Fiber Technology, 2000. **6**(2): p. 122-154.
112. Kim, J., et al., *Static gain saturation model of quantum-dot semiconductor optical amplifiers.* Ieee Journal of Quantum Electronics, 2008. **44**(7-8): p. 658-666.
113. Cho, H.J. and C.J. Lissenden, *Structural health monitoring of fatigue crack growth in plate structures with ultrasonic guided waves.* Structural Health Monitoring-an International Journal, 2012. **11**(4): p. 393-404.
114. Botsev, Y., et al., *Structural Health Monitoring using an Embedded PZT-FBG Ultrasonic Sensor Array.* Proceedings of the Fourth European Workshop on Structural Health Monitoring 2008, 2008: p. 649-656.
115. Olsson, B.E., M. Karlsson, and P.A. Andrekson, *Polarization mode dispersion measurement using a sagnac interferometer and a comparison with the fixed analyzer method.* Ieee Photonics Technology Letters, 1998. **10**(7): p. 997-999.
116. Flavin, D.A., R. McBride, and J.D.C. Jones, *Dispersion of birefringence and differential group delay in polarization-maintaining fiber.* Optics Letters, 2002. **27**(12): p. 1010-1012.
117. Kim, C.S., et al., *Optical fiber modal birefringence measurement based on Lyot-Sagnac interferometer.* Ieee Photonics Technology Letters, 2003. **15**(2): p. 269-271.
118. Hlubina, P. and D. Ciprian, *Spectral-domain measurement of phase modal birefringence in polarization-maintaining fiber.* Optics Express, 2007. **15**(25): p. 17019-17024.
119. Huttner, B., et al., *Local birefringence measurements in single-mode fibers with coherent optical frequency-domain reflectometry.* Ieee Photonics Technology Letters, 1998. **10**(10): p. 1458-1460.
120. Froggatt, M.E., et al., *Characterization of polarization-maintaining fiber using high-sensitivity optical-frequency-domain reflectometry.* Journal of Lightwave Technology, 2006. **24**(11): p. 4149-4154.
121. Dong, Y.K., L. Chen, and X.Y. Bao, *Truly distributed birefringence measurement of polarization-maintaining fibers based on transient Brillouin grating.* Optics Letters, 2010. **35**(2): p. 193-195.
122. Koyamada, Y., et al., *Novel fiber-optic distributed strain and temperature sensor with very high resolution.* Ieice Transactions on Communications, 2006. **E89b**(5): p. 1722-1725.
123. Imahama, M., Y. Koyamada, and K. Hogari, *Restorability of Rayleigh backscatter traces measured by coherent OTDR with precisely frequency-controlled light source.* Ieice Transactions on Communications, 2008. **E91b**(4): p. 1243-1246.
124. Lu, X., M.A. Soto, and L. Thévenaz, *MilliKelvin resolution in cryogenic temperature distributed fibre sensing based on coherent Rayleigh scattering.* 23rd International Conference on Optical Fibre Sensors, 2014. **9157**.
125. Grubb, S.G., et al., *High-Power 1.48 μm Cascaded Raman Laser in Germanosilicate Fibers.* Optical Amplifiers and Their Applications, 1995. **18**.

126. Ania-Castanon, J.D., et al., *Simultaneous spatial and spectral transparency in ultralong fiber lasers.* Physical Review Letters, 2008. **101**(12): p. -.
127. Park, K.D., et al., *Dynamics of cascaded Brillouin-Rayleigh scattering in a distributed fiber Raman amplifier.* Optics Letters, 2002. **27**(3): p. 155-157.
128. Min, B., P. Kim, and N. Park, *Flat amplitude equal spacing 798-channel Rayleigh-assisted Brillouin/Raman multiwavelength comb generation in dispersion compensating fiber.* Ieee Photonics Technology Letters, 2001. **13**(12): p. 1352-1354.
129. Zamzuri, A.K., et al., *Brillouin-Raman comb fiber laser with cooperative Rayleigh scattering in a linear cavity.* Optics Letters, 2006. **31**(7): p. 918-920.
130. Shahi, S., S.W. Harun, and H. Ahmad, *Multi-wavelength Brillouin fiber laser using Brillouin-Rayleigh scatterings in distributed Raman amplifier.* Laser Physics Letters, 2009. **6**(10): p. 737-739.
131. Pinto, A.M.R., et al., *Multiwavelength fiber laser based on a photonic crystal fiber loop mirror with cooperative Rayleigh scattering.* Applied Physics B-Lasers and Optics, 2010. **99**(3): p. 391-395.
132. Pinto, A.M.R., et al., *Multiwavelength Raman Fiber Lasers Using Hi-Bi Photonic Crystal Fiber Loop Mirrors Combined With Random Cavities.* Journal of Lightwave Technology, 2011. **29**(10): p. 1482-1488.
133. Turitsyn, S.K., et al., *Random distributed feedback fibre laser.* Nature Photonics, 2010. **4**(4): p. 231-235.
134. El-Taher, A.E., et al., *Dual-wavelength, ultralong Raman laser with Rayleigh-scattering feedback.* Optics Letters, 2010. **35**(7): p. 1100-1102.
135. Frazao, O., et al., *Applications of fiber optic grating technology to multi-parameter measurement.* Fiber and Integrated Optics, 2005. **24**(3-4): p. 227-244.
136. Ferreira, M.S., et al., *A vibration sensor based on a distributed Bragg reflector fibre laser.* Laser Physics Letters, 2013. **10**(9).
137. Martins, H.F., M.B. Marques, and O. Frazao, *Temperature-insensitive strain sensor based on four-wave mixing using Raman fiber Bragg grating laser sensor with cooperative Rayleigh scattering.* Applied Physics B-Lasers and Optics, 2011. **104**(4): p. 957-960.
138. Demjanenko, V., et al., *A Noninvasive Diagnostic Instrument for Power Circuit-Breakers.* Ieee Transactions on Power Delivery, 1992. **7**(2): p. 656-663.
139. Runde, M., et al., *Acoustic Diagnosis of High-Voltage Circuit-Breakers.* Ieee Transactions on Power Delivery, 1992. **7**(3): p. 1306-1315.
140. Gangopadhyay, T.K., *Prospects for Fibre Bragg Gratings and fabry-perot interferometers in fibre-optic vibration sensing.* Sensors and Actuators a-Physical, 2004. **113**(1): p. 20-38.
141. Giallorenzi, T.G., et al., *Optical Fiber Sensor Technology.* Ieee Journal of Quantum Electronics, 1982. **18**(4): p. 626-665.
142. Mandal, J., et al., *Bragg grating tuned fiber laser system for measurement of wider range temperature and strain.* Optics Communications, 2005. **244**(1-6): p. 111-121.
143. Varshney, S.K., et al., *Coupling Characteristics of Multicore Photonic Crystal Fiber-Based 1 x 4 Power Splitters.* Journal of Lightwave Technology, 2009. **27**(12): p. 2062-2068.
144. Yue, Y., et al., *Broadband single-polarization single-mode photonic crystal fiber coupler.* Ieee Photonics Technology Letters, 2006. **18**(17-20): p. 2032-2034.

145. Laegsgaard, J., O. Bang, and A. Bjarklev, *Photonic crystal fiber design for broadband directional coupling.* Optics Letters, 2004. **29**(21): p. 2473-2475.
146. Chen, M.Y., X.X. Fu, and Y.K. Zhang, *Design and analysis of a low-loss terahertz directional coupler based on three-core photonic crystal fibre configuration.* Journal of Physics D-Applied Physics, 2011. **44**(40).
147. Saitoh, K., et al., *Tunable photonic crystal fiber couplers with a thermo-responsive liquid crystal resonator.* Journal of Lightwave Technology, 2008. **26**(5-8): p. 663-669.
148. Saitoh, K., et al., *Design of narrow band-pass filters based on the resonant-tunneling phenomenon in multicore photonic crystal fibers.* Optics Express, 2005. **13**(25): p. 10327-10335.
149. Husakou, A.V. and J. Herrmann, *Frequency comb generation by four-wave mixing in a multicore photonic crystal fiber.* Applied Physics Letters, 2003. **83**(19): p. 3867-3869.
150. Dudley, J.M., G. Genty, and S. Coen, *Supercontinuum generation in photonic crystal fiber.* Reviews of Modern Physics, 2006. **78**(4): p. 1135-1184.
151. Mafi, A. and J.V. Moloney, *Phase locking in a passive multicore photonic crystal fiber.* Journal of the Optical Society of America B-Optical Physics, 2004. **21**(5): p. 897-902.
152. Michaille, L., et al., *Characteristics of a Q-switched multicore photonic crystal fiber laser with a very large mode field area.* Optics Letters, 2008. **33**(1): p. 71-73.
153. Michaille, L., et al., *Multicore Photonic Crystal Fiber Lasers for High Power/Energy Applications.* Ieee Journal of Selected Topics in Quantum Electronics, 2009. **15**(2): p. 328-336.
154. Guan, C.Y., L.B. Yuan, and J.H. Shi, *Supermode analysis of multicore photonic crystal fibers.* Optics Communications, 2010. **283**(13): p. 2686-2689.
155. Wang, C.C., et al., *Photonic crystal fiber for fundamental mode operation of multicore fiber lasers and amplifiers.* Optics Communications, 2008. **281**(21): p. 5364-5371.
156. Cardenas-Sevilla, G.A., et al., *Photonic crystal fiber sensor array based on modes overlapping.* Optics Express, 2011. **19**(8): p. 7596-7602.
157. Jensen, J.B., et al., *Photonic crystal fiber based evanescent-wave sensor for detection of biomolecules in aqueous solutions.* Optics Letters, 2004. **29**(17): p. 1974-1976.
158. Reimlinger, M., et al., *Multicore Photonic Crystal Fiber Force Meters.* Sensors and Smart Structures Technologies for Civil, Mechanical, and Aerospace Systems 2011, 2011. **7981**.
159. Chen, D., G. Hu, and L. Chen, *Dual-Core Photonic Crystal Fiber for Hydrostatic Pressure Sensing.* Ieee Photonics Technology Letters, 2011. **23**(24).
160. Chen, W.G., et al., *Highly Sensitive Torsion Sensor Based on Sagnac Interferometer Using Side-Leakage Photonic Crystal Fiber.* Ieee Photonics Technology Letters, 2011. **23**(21): p. 1639-1641.
161. Deng, M., et al., *PCF-Based Fabry-Perot Interferometric Sensor for Strain Measurement at High Temperatures.* Ieee Photonics Technology Letters, 2011. **23**(11): p. 700-702.
162. Nalawade, S.M. and H.V. Thakur, *Photonic Crystal Fiber Strain-Independent Temperature Sensing Based on Modal Interferometer*. Ieee Photonics Technology Letters, 2011. **23**(21): p. 1600-1602.

163. MacPherson, W.N., et al., *Remotely addressed optical fibre curvature sensor using multicore photonic crystal fibre.* Optics Communications, 2001. **193**(1-6): p. 97-104.
164. Michaille, L., et al., *Damage threshold and bending properties of photonic crystal and photonic band-gap optical fibres.* Integrated Optical Devices, Nanostructures, and Displays, 2004. **5618**: p. 30-38.
165. Burnett, J.G., P.M. Blanchard, and A.H. Greenaway, *Optical Fibre-based Vectoral Shape Sensor.* Strain, 2000. **36**(3): p. 127-133.
166. Flockhart, G.M.H., et al., *Two-axis bend measurement with Bragg gratings in multicore optical fiber.* Optics Letters, 2003. **28**(6): p. 387-389.
167. Zetterlund, E., et al., *Gemini Fiber for Interferometry and Sensing Applications.* Journal of Sensors, 2009. **2009**.
168. Frazao, O., et al., *Optical bend sensor based on a long-period fiber grating monitored by an optical time-domain reflectometer.* Optical Engineering, 2005. **44**(11).
169. Gong, Y., et al., *All-Fiber Curvature Sensor Based on Multimode Interference.* Ieee Photonics Technology Letters, 2011. **23**(11): p. 679-681.
170. Frazao, O., J.P. Carvalho, and H.M. Salgado, *Low-loss splice in a microstructured fibre using a conventional fusion splicer.* Microwave and Optical Technology Letters, 2005. **46**(2): p. 172-174.
171. Kuhlmey, B.T., et al., *Microstructured optical fibers: where's the edge?* Optics Express, 2002. **10**(22): p. 1285-1290.
172. Gander, M.J., et al., *Two-axis bend measurement using multicore optical fibre.* Optics Communications, 2000. **182**(1-3): p. 115-121.
173. Meltz, G. and E. Snitzer, *Fiber optic strain sensor*, WIPO Patent WO1981000618 A1, March 5, 1981, Google Patents.
174. Meltz, G., et al., *Cross-Talk Fiber-Optic Temperature Sensor.* Applied Optics, 1983. **22**(3): p. 464-477.
175. Zhang, L. and C.X. Yang, *Polarization-dependent coupling in twin-core photonic crystal fibers.* Journal of Lightwave Technology, 2004. **22**(5): p. 1367-1373.
176. Wang, Z., et al., *Coupling in dual-core photonic bandgap fibers: theory and experiment.* Optics Express, 2007. **15**(8): p. 4795-4803.
177. Yuan, W., G.E. Town, and O. Bang, *Refractive Index Sensing in an All-Solid Twin-Core Photonic Bandgap Fiber.* Ieee Sensors Journal, 2010. **10**(7): p. 1192-1199.
178. Markos, C., et al., *Label-free biosensing with high sensitivity in dual-core microstructured polymer optical fibers.* Optics Express, 2011. **19**(8): p. 7790-7798.
179. Sun, X.W., *Wavelength-selective coupling of dual-core photonic crystal fiber with a hybrid light-guiding mechanism.* Optics Letters, 2007. **32**(17): p. 2484-2486.
180. Frazao, O., et al., *Temperature- and strain-independent torsion sensor using a fiber loop mirror based on suspended twin-core fiber.* Optics Letters, 2010. **35**(16): p. 2777-2779.
181. Town, G.E., et al., *Microstructured optical fiber refractive index sensor.* Optics Letters, 2010. **35**(6): p. 856-858.
182. Wu, D.K.C., B.T. Kuhlmey, and B.J. Eggleton, *Ultrasensitive photonic crystal fiber refractive index sensor.* Optics Letters, 2009. **34**(3): p. 322-324.

183. Kim, B., et al., *Twin core photonic crystal fiber for in-line Mach-Zehnder interferometric sensing applications.* Optics Express, 2009. **17**(18): p. 15502-15507.
184. Liu, S.H., et al., *Simple In-Line M-Z Interferometer Based on Dual-Core Photonic Crystal Fiber.* Ieee Photonics Technology Letters, 2012. **24**(19): p. 1768-1770.